Meshless methods for Maxwell's equations with applications to magnetotelluric modelling and inversion

Inaugural-Dissertation

zur

Erlangung des Doktorgrades

der Mathematisch-Naturwissenschaftlichen Fakultät

der Universität zu Köln vorgelegt von

Jan Wittke

aus Wilhelmshaven

Köln, 2017

Berichterstatter: Prof. Dr. B. Tezkan
Prof. Dr. K. Spitzer
Prof. Dr. M. Becken

Tag der mündlichen Prüfung: 16.11.2017

| Dedicated to my parents and my sister.

Abstract

The first part of thesis presents new meshless methods for solving time harmonic electromagnetic fields in closed two- or three-dimensional volumes containing heterogeneous materials. This new methods will be used to simulate magnetotelluric experiments, when an Earth conductivity model is given in advanced. Normally, classical approximation methods like finite elements or finite differences are used to solve this task. The algorithms here in this thesis, only need an unstructured point sampling in the modelling domain for the discretization and is able to gain a solution for the partial differential equation without a fixed mesh or grid. This is advantageous when complex model geometries have to be described, because no adapted mesh or grid need to be generated. The meshless methods, described here in this thesis, use a direct discretization technique in combination with a generalized approximation method. This allows to formulate the partial differential equations in terms of linear functionals, which can be approximated and directly form the discretization. For the two-dimensional magnetotelluric problem, a second-order accurate algorithm to solve the partial differential equations was developed and tested with several example calculations. The accuracy of the new meshless methods was compared to analytical solutions, and it was found, that a better accuracy can be achieved with less degrees of freedoms compared to previously published results. For the three-dimensional case, a meshless formulation was given and numerical calculations show the ability of the scheme to handle models with heterogeneous conductivity structures. In the second part of this thesis, the newly developed two-dimensional simulation method will be used in an inversion scheme. Here, the task is to recover the unknown Earth conductivity model with the help of data gained from a magnetotelluric experiment. Due to the previously developed meshless approximation algorithm, some numerical tasks during the inversion can be simplified by reusing the discretization defined on the point sampling from the forward simulation. The newly developed meshless inversion algorithm will be tested with synthetic data to reconstruct known conductivity anomalies. It can be shown, that the inverse algorithm produces correct results, even in the presence of topography.

Zusammenfassung

Im Rahmen dieser Arbeit wurde ein neuartiges Verfahren zur zwei- und dreidimensionalen Modellierung von magnetotellurischen Daten vorgestellt. Weiterhin wurde, basierend auf den Entwicklungen zur mangetotellurischen Modellierung, ein Verfahren implementiert, welches die zweidimensionale Inversion von magnetotellurischen Daten ermöglicht.
Im Gegensatz zu etablierten Simmulationsverfahren, verwendet diese neu entwickelte Methode kein numerisches Gitter zur Diskretisierung der partiellen Differentialgleichungen. Es genügen lediglich im Modellraum gleichmäßig verteilte Punkte zur Berechnung der Diskretisierung. Durch die Vermeidung eines starren Gitters zur Berechnung der Diskretisierung ergeben sich numerische Vorteile, welche schwer durch eine starre Gitterdiskretisierung realisierbar sind.
Komplexe Modellgeometrien können besser diskretisiert werden und der rechnerische Aufwand, ein qualitativ hochwertiges Gitter zu erzeugen, entfällt. Weiterhin können die Berechnungen, welche nötig sind um ein Gleichungssystem zu erstellen, das zur Näherungslösung der Differentialgleichung führt, für jeden Freiheitsgrad unabhängig voneinander durchgeführt werden. Das verwendete Verfahren, welches zur Diskretisierung genutzt wird, hat seinen Ursprung in der Approximationstheorie und ermöglicht es beliebige, lineare Funktionale zu approximieren. Die Diskretisierung der Differentialgleichungen ist dann möglich, da sie als System linearer Funktionale formuliert werden können. Durch diese Art der Approximation ergeben sich in der weiteren Verwendung zusätzliche Vorteile. Wurde eine Differentialgleichung einmal mit dem Verfahren diskretisiert, erhält man durch die vorhandene Diskretisierung die Möglichkeit jegliche Approximation oder Integration auf den Punkten im Modellraum ohne erheblichen Mehraufwand zu berechnen. Dieses ist von Vorteil bei der Inversion von magnetotellurischen Daten. Das im letzten Teil der Arbeit vorgestellte Inversionsverfahren verwendet genau diesen Ansatz, um die Diskretisierung für eine Regularisierung des Inversionsalgorithmus zu verwenden. Das inverse Verfahren wird hierbei für die Erstellung von Leitfähigkeitsmodellen aus gemessenen magnetotellurischen Daten verwendet. Tests mit Hilfe von synthetische Datensätzen, wobei blockförmige Leitfähigkeitsanomalien innerhalb eines homogenen Halbraumes rekonstruiert werden, zeigen die Anwendbarkeit des Algorithmus.

Contents

List of Figures

List of Tables

Acronyms

This list specifies the common acronyms used in this thesis.

1D	one-dimensional
2D	two-dimensional
3D	three-dimensional
DMLPG	direct meshless local Petrov-Galerkin
FD	finite difference method
FEM	finite element method
GMLS	generalized moving least squares
MLPG	meshless local Petrov-Galerkin
MLS	moving least squares
MT	magnetotellurics
PDE	partial differential equation
rms	root mean square
TE	transverse electric mode / E-polarisation
TM	transverse magnetic mode / B-polarisation

List of Symbols

This list only specifies the symbols with a physical meaning used in this thesis. Mathematical symbols are not be listed here and will be defined as used. Mathematical function spaces will be listed in Appendix A.1. Bolt symbols are vectors and have components according to the spatial dimension, for example in two dimension this will be $\mathbf{E} = (E_x, E_y)^T$. Tensors will be denoted with a underlying bar.

Symbol	SI-Unit	Description
I	A	current
$\mathbf{A}$	$\mathrm{V\,s\,m^{-1}}$	magnetic vector potential
$\mathbf{B}$	T	magnetic induction
$\mathbf{D}$	$\mathrm{A\,s\,m^{-2}}$	electric displacement
$\mathbf{E}$	$\mathrm{V\,m^{-1}}$	electric field
$\mathbf{H}$	$\mathrm{A\,m^{-1}}$	magnetic intensity
$\mathbf{j}$	$\mathrm{A\,m^{-2}}$	electrical current density
μ_0	$4\pi \times 10^{-7}$ Vs/Am	magnetic permeability of the vacuum
μ	$\mathrm{V\,s\,A^{-1}\,m^{-1}}$	magnetic permeability
ω	Hz=1/s	angular frequency
ϕ	V	scalar potential
ρ_a	$\Omega\,\mathrm{m}$	apparent resistivity
ρ_e	$\mathrm{C/m^d}$	electric charge density ($d = 2, 3$)
ρ	$\Omega\,\mathrm{m}$	electrical resistivity
σ	$\mathrm{S\,m^{-1}}$	electrical conductivity
$\underline{\mathbf{Z}}$	$\mathrm{V\,A^{-1}}$	magnetotelluric impedance
ε_0	8.854×10^{-12} As/Vm	electrical permittivity of the vacuum
ε	$\mathrm{A\,s\,V^{-1}\,m^{-1}}$	electrical permittivity
φ	$^\circ$	magnetotelluric phase
c	$299\,792\,458\,\mathrm{m\,s^{-1}}$	speed of light in vacuum
f	Hz=1/s	frequency

Introduction

To understand the interior composition of Earth material several applied geophysical methods have been developed during the last decades. An important tool in the interpretation is the numerical simulation of the real geophysical experiment through boundary value problems and their corresponding partial differential equations. Simplifications of the physical description should be made to reasonably simulate the physical process with the available numerical tools at hand. Classical numerical methods like finite differences or finite elements have been successfully applied to simulate the geophysical experiment with a given idealistic material parameter distribution. All of these numerical methods rely on computational grids or meshes to calculate the discretization of the underlying partial differential equation. A lot of effort has been devoted to the process of mesh generation. To generate qualitative meshes to handle complex geometries is a significant task and even if a lot of mesh generators are freely available, the main valuable part of a mesh based application, which solves partial differential equations, is the mesh generator. In the development of numerical simulation tools for the computation of electromagnetic fields used in applied geophysical methods the progress has been mostly devoted to improve existent classical approaches. Even if different numerical methods were available, less progress has been made to adapt these novel schemes to the field of electromagnetic geophysics. This thesis will present first attempts utilizing novel discretization strategies, to solve the boundary value problems for the simulation of electromagnetic fields, which occur in an applied geophysical method called Magnetoellurics. This newly developed approach can be categorized into the class of meshless or meshfree methods. These discretization schemes do not rely on a fixed mesh or grid and can handle unorganized point samplings to solve a boundary value problem. In the second part of this thesis, the simulation method will be applied in an inverse scheme to reconstruct conductivity models from given magnetotelluric data.

Methods to solve the magnetotelluric forward problem have a long history of use and development in theoretical geophysics. The focus here is on finite differences and finite elements, because of their popularity, even if there are other methods like the integral equation method or boundary element method. One of the first practically usable finite difference implementations has been provided by Jones and Pascoe (1971). Followed by a publication by Brewitt-Taylor and Weaver (1976) about the finite difference solution of two-dimensional induction problems and an implementation of Červ et al. (1978). An

implementation that incorporates two-dimensional anisotropic conductivity structures was given by Pek and Verner (1997). Even though the finite differences implementations gave reasonable results, the development of two-dimensional finite element formulations began at the same time. One of the earliest publication is due to Coggon (1971) followed by Kisak and Silvester (1975). This was the time, when the theoretical work of finite element methods dealt with discontinuous approximations Babuška (1970). Finally, the work of Rodi (1976) improves the modelling using finite element methods and one decade later the formulation of Wannamaker et al. (1985) was published. Their work is used up to now, and is one of the building blocks in the well known Occam's inversion developed by Degroot and Constable (1990). Reasonable improvements have been made in Li and Key (2007) and Franke et al. (2007) as well as in Key and Ovall (2011), by using unstructured meshes which can be adapted to the error of the calculations. The work of Key and Ovall (2011) results in the most up-to-date implementation of Key (2016).
Parallel to the development of two-dimensional finite element and finite difference approximations, three-dimensional modelling schemes have been developed. Here the developments of the finite element algorithms are tied strongly to the use of elements proposed by Nedelec (1980). While the first three-dimensional schemes given by Weidelt (1975) and Ting and Hohmann (1981) used the integral equation approach, early finite element formulations were given by Mogi (1996), Everett and Schultz (1996) or Zyserman and Santos (2000). In contrast to finite element methods, finite differences often use a staggered Yee scheme (Yee, 1966) for the discretization and have been investigated by Wannamaker et al. (1984), Mackie et al. (1993), Mackie et al. (1994) or Weiss and Newman (2002). Recent developments use finite element schemes with unstructured grids as described by Schwarzbach (2009); Schwarzbach and Haber (2013), Ansari and Farquharson (2014) or Grayver and Kolev (2015).
Nevertheless, meshless methods for geophysical electromagnetic modelling have not been considered until the work of Wittke and Tezkan (2014). Up to now, only Li et al. (2015) and Ji et al. (2017) published results on this topic. Here in this thesis, new research on this topic will be presented, including two- and three dimensional meshless magnetotelluric modelling and inversion.

1.1 Outline of research

An introduction on electromagnetic theory to describe the basic electromagnetic phenomena and the fundamental principles of the magnetotelluric method is presented in the

Sub-chapter 1.1. Starting with an overview on the magnetotelluric method, Maxwell's equations and various physical assumptions, as well as electromagnetic potential formulation are given to describe electromagnetic fields. Here, gauge conditions are essential for these formulations and as a result gauged vector potential formulations are stated.
This special choice, describing the electromagnetic fields using potentials, results in the smoothness of the vector potential fields. In this formulation the potential fields are smooth across conductivity interfaces, what is beneficial for the meshless approximation scheme. This is described in the Sub-chapter 3.6 of electromagnetic interface conditions. When interface conditions are defined, it is possible to apply them at the outer boundaries of a computational domain. Here, boundary conditions have to be considered. The description of various conditions, that can be imposed on outer boundaries which closes the computational domain are given in Sub-chapter 2.4.2. After presenting all components for arranging boundary values problems, formulations for the induction in two-dimensional conductivity structures are given in the Sub-chapter 2.5. Here the formulation splits into two separate equation systems, corresponding to the electrical and magnetic fields. The Sub-chapter 2.6 about second order formulations gives the complete sets of equations for the boundary value problems in two and three dimensions. At the end of this Chapter, special modifications for the earlier stated differential equations are given, to adapt the general formulations to the magnetotelluric case.
In the Chapter 2.8 about meshless methods for Maxwell's equations, a general description of the generalized moving least squares method is given first. After presenting an extension to this method, error bounds are given. The Sub-chapter 3.4 about the meshless formulations presents the formulations for the two- and three-dimensional problems according to a description using linear functionals. The actual implementation is given in Sub-chapter 3.5, while Sub-chapter 3.6 discusses the descriptions of interfaces and their discretization. Sub-chapter 3.7 informs about how to generate point samplings and how to solve the sparse linear system of equations. Convergence results for the meshless algorithms are given in Sub-chapter 3.8. In this Sub-chapter magnetotelluric example calculations are also conducted, to test the newly developed forward algorithm.
The Section 3.9 is devoted to the development of a meshless inverse algorithm. Sub-chapter 4.1 introduces the basic inversion theory and, later on, the Sub-chapter 4.2 deals with the calculation of meshless fréchet derivatives. After presenting regularization schemes in Sub-chapter 4.3 example inversions are given in Sub-chapter 4.4.

The magnetotelluric method

The magnetotelluric (MT) method is one of the oldest and best established geophysical exploration techniques to probe the Earth's conductivity structure down to depth of several thousands meters. It is a passive, natural-source electromagnetic method, easy to apply in the field, and widely used for scientific and industrial exploration. The fundamental principle of the method is to establish a better understanding of the conductivity structure inside the Earth by comparing measured electrical and magnetic fields at its surface. Precise information about the source current distribution which generates the measured electromagnetic fields can be neglected. These natural time-varying electromagnetic fields have their origin in the Earth's ionosphere and magnetosphere. Here, interactions of solar and near-Earth plasma with the geomagnetic field generate electrical currents of mostly unknown shape and size. Basic types of magnetotelluric field variations are generated by pulsations, polar sub-storms, solar daily variations and worldwide magnetic storms (Berdichevsky and Dmitriev, 2002). These sources are substantial for generating long-period (>1 s) signals, while short periods are commonly due to meteorological processes. A significant drop in the signal strength can be observed in the frequency around 1 Hz, which is commonly referred as the MT dead-band (Simpson and Bahr, 2005).

The most basic assumption which can be made, is a plane electromagnetic wave vertically incident on an Earth consisting of homogeneous, horizontal, isotropic conductivity layering. This plane-wave assumption is mathematical justifiable, but lacks a precise physical model (Chave and Jones, 2012). Nevertheless, it is the basic foundation of the classical magnetotelluric theory given by Rikitake (1948), Tikhonov (1950), Cagniard (1953) and establishes a tensor relationship between the horizontal electric field $\mathbf{E}$ and magnetic field $\mathbf{H}$

$$\mathbf{E} = \underline{\mathbf{Z}} \cdot \mathbf{H}, \tag{2.1}$$

with the MT impedance $\underline{\mathbf{Z}}$ as a function of period. The impedance contains information about the electrical conductivity structure and can be transformed into an apparent resistivity and phase. For the simple case of a one-dimensional, isotropic layered Earth, this transformation is given by

$$\bar{\rho}_a = \frac{i}{\mu_0 \omega} Z^2 = \rho_a e^{i\phi_a}, \tag{2.2}$$

in which the absolute value

$$\rho_a = |\bar{\rho}_a| = \frac{|Z^2|}{\mu_0 \omega}, \tag{2.3}$$

defines the apparent resistivity ρ_a. The complex argument

$$\varphi_a = \arg \bar{\rho}_a = 2 \arg Z + \pi/2, \tag{2.4}$$

is the magnetotelluric phase (Berdichevsky and Dmitriev, 2002). Both are a function of the frequency ω and this formulation allows interpreting qualitatively the variation of Earth's resistivity with depth, because the penetration depth of electromagnetic fields varies with their frequency. The apparent resistivity can be interpreted as the weighted average of Earth's resistivity within a specific volume, in which electromagnetic energy is dissipated (Berdichevsky, 1968).

During a magnetotelluric experiment, time series of the electric and magnetic fields are recorded. A sketch of a magnetotelluric measurement set-up is displayed in Figure 2.1. The electric field can be measured by grounded, separated electrodes, sensing voltage variations versus time. Dividing these voltage variations by the electrode spacing gives an approximation of the electric field. The magnetic field can be sensed by induction coils measuring either horizontal or vertical field variations. After processing the recorded data, the final product is in the most simple case a set of apparent resistivity values and phases plotted against a different frequency range. They can be used to identify conductivity changes in the subsurface beneath the measuring site.

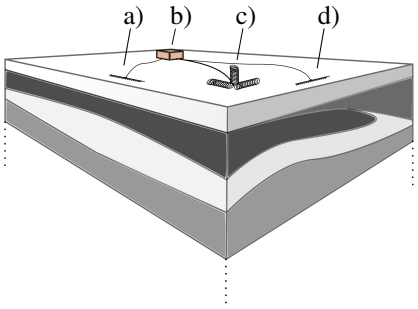

Figure 2.1: Schematic of a magnetotelluric measurement experiment set-up including: a) & d) electrical sensors, b) recording unit, c) magnetic sensors.

The magnetotelluric assumptions

Simulating an experiment utilizing the magnetotelluric method, some basic assumptions can be made to simplify the underlying physical model. A general list is given by Simpson and Bahr (2005) and have been discussed in many publications (Vozoff, 1991;

Berdichevsky and Dmitriev, 2002). Here, two important simplifications will be restated:

- The electromagnetic source fields, which are used by the magnetotelluric method, are generated far away from the Earth surface by large uniform current sheets. These source fields can be simply described as uniform plane-polarized electromagnetic waves, normally incident on the Earth surface.

- Propagation of electromagnetic fields are described by a diffusion process rather than an electromagnetic wave propagation. This assumption, often referred to as the *MT-approximation*, neglects occurring displacement currents due to the applied time scales, as well as size of the induction process.

Assuming a source field which can be characterized as a plane-wave leads to the time invariance of the magnetotelluric impedance tensor $\underline{\mathbf{Z}}$. Repeated measurements should be similar or even equal if the conductivity structure inside Earth does not change over time.

Electromagnetic properties of Earth materials

One of the main objective of a magnetotelluric experiment is to increase an understanding of the Earth's interior composition. The link between magnetotelluric field variations and induction processes in Earth are the electromagnetic properties of naturally occurring materials. However, interpretations of magnetotelluric measurements will only be successful if valuable laboratory measurements of material parameter are available to compare with.
The electromagnetic properties of Earth materials in this thesis will be described with three basic parameters, the electrical conductivity σ (or reciprocal the electrical resistivity ρ), the electrical permittivity ϵ and the magnetic permeability μ. All of them can be functions of other physical parameters for example temperature, pressure or water content. For simplicity, in this thesis only a spatial dependence is assumed and their mathematical description will be stated more precisely in the subsequent chapter. For a general overview of different physical processes and descriptions about these properties, the reader is referred to the work of Chave and Jones (2012) or Palacky (1988). To get an idea about the ranges in electrical conductivities, a table (see Figure 2.2) is compiled to give an overview on common Earth materials.

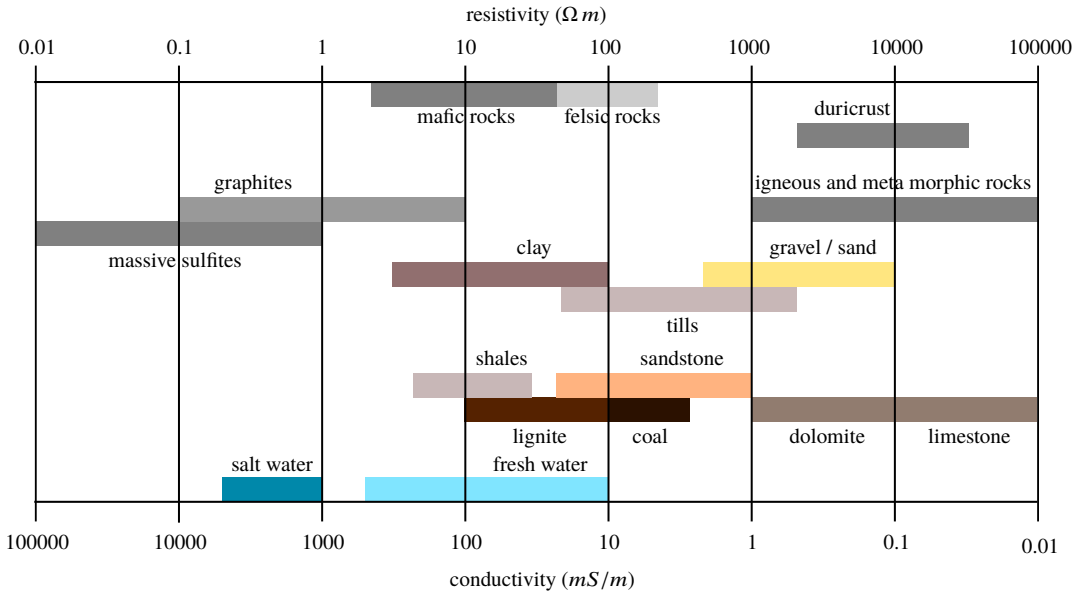

Figure 2.2: Overview of conductivity and resistivity values of some common Earth materials, modified after (Miensopust, 2010; Palacky, 1988).

2.1 Basic notations

Assuming spatial varying material parameters, mathematical descriptions are needed to specify the behaviour of the electromagnetic fields. Generally, all considerations take place in a proper subset of the whole space in $\mathbb{R}^3$. This finite domain is named by $\Omega \subsetneq \mathbb{R}^3$, while its Lipschitz-continuous boundary is denoted by $\Gamma = \partial\Omega$. If a boundary is composed of several individual parts, a superscript index $\Gamma^{i=1,\dots,k}$ is used to differentiate them into k different components. In some cases, a boundary can be named after its special type. For example, Dirichlet type boundaries will be named with Γ^D, Neumann type boundaries are denoted by Γ^N, electric boundaries by Γ^e, and so on. In the three dimensional case, $\partial\Omega \subsetneq \mathbb{R}^2$ and for a two dimensional domain its boundary is in $\mathbb{R}$. All of these domains can be decomposed in non-overlapping parts. For example, the computational domain Ω can be divided into $\Omega = \cup_i \Omega_i$ and for some $i \neq j$ the intersection $\Omega_i \bigcap \Omega_j = \emptyset$. The same is also valid for the boundaries. Thus, the computational domain is a convex polygon (see Figure 2.3). An interface between two regions Ω_i and Ω_j is denoted by $\Gamma_{i,j}^{int} = \bar{\Omega}_i \cap \bar{\Omega}_j$. If a function $f(\mathbf{x})$ has a discontinuity on an interface, this will be expressed with

$$[f(\mathbf{x})]_{i,j} = f^+(\mathbf{x}) - f^-(\mathbf{x}), \quad \mathbf{x} \in \Gamma_{i,j}^{int}, \tag{2.5}$$

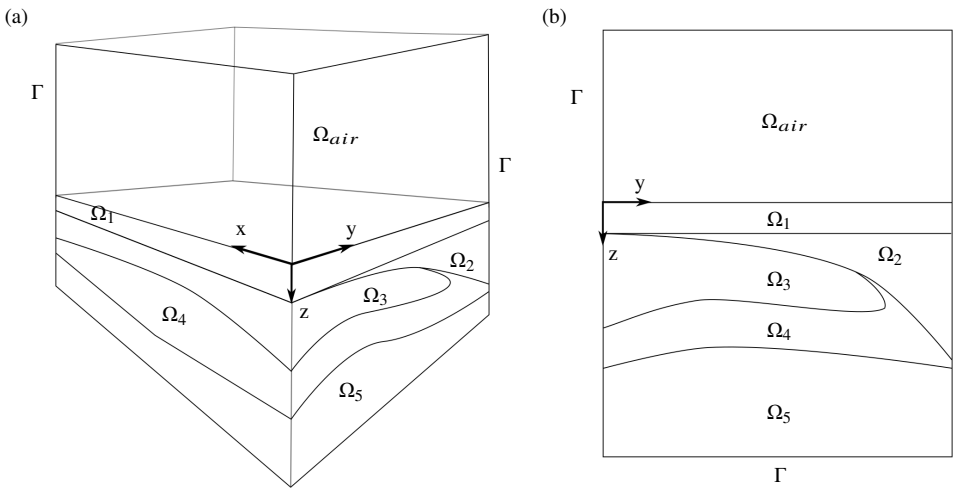

Figure 2.3: Example of computational domains. (a) A three-dimensional model domain composed from various sub-domains, called Ω*. Enclosed by a boundary denoted by* Γ *(b) A two-dimensional model abstraction, where the labeling is the same as in the three-dimensional model.*

whereas functions at the interface are defined with $f^+(\mathbf{x}) = \lim_{\delta\to 0} f(\mathbf{x} + \delta\mathbf{n})$ and $f^-(\mathbf{x}) = lim_{\delta\to 0} f(\mathbf{x} - \delta\mathbf{n})$.

2.2 Material parameters and Ohm's law

As stated in the previous chapter, the main intention of this work is the calculation of electromagnetic fields from a given, spatial material parameter distribution as well as the prediction of material parameters according to measured electromagnetic fields. As material properties be defined at a microscopic level, macroscopic scale properties of materials play a prominent role. Here, all electromagnetic fields are related through constitutive relations which define a linear dependence between the fields:

$$\mathbf{D} = \underline{\boldsymbol{\varepsilon}}\mathbf{E}, \tag{2.6}$$

$$\mathbf{B} = \underline{\boldsymbol{\mu}}\mathbf{H}. \tag{2.7}$$

The proportionally factors $\underline{\boldsymbol{\varepsilon}} : \mathbb{R}^3 \to \mathbb{R}^{3\times 3}$ and $\underline{\boldsymbol{\mu}} : \mathbb{R}^3 \to \mathbb{R}^{3\times 3}$ are the electrical permittivity and the magnetic permeability tensors, respectively. When the electromagnetic process is driven by an applied current density $\mathbf{J}^e$ the generalized Ohm's law reads

$$\mathbf{J} = \underline{\boldsymbol{\sigma}}\mathbf{E} + \mathbf{J}^e, \tag{2.8}$$

with the electrical conductivity tensor as a matrix valued function $\underline{\boldsymbol{\sigma}} : \mathbb{R}^3 \to \mathbb{R}^{3\times3}$. In this experimentally justified relation, the conductivity takes the prominent role, as all following electromagnetic calculations are based on this parameter. All these material parameters are generally not constant, but symmetric and uniformly positive definite matrices with bounded functions of the spatial position. For the conductivity, this reads (in coordinates) for example:

$$\begin{pmatrix} J_x \\ J_y \\ J_z \end{pmatrix} = \begin{pmatrix} \sigma_{11} & \sigma_{12} & \sigma_{13} \\ \sigma_{21} & \sigma_{22} & \sigma_{23} \\ \sigma_{33} & \sigma_{23} & \sigma_{33} \end{pmatrix} \begin{pmatrix} E_x \\ E_y \\ E_z \end{pmatrix}. \tag{2.9}$$

The conductivity should also uniformly bounded from below and above by two strictly positive constants (Santos and Sheen, 2000). This is physically intuitive, because Earth materials should always have a positive conductivity. If the extremal values are denoted by σ_{max} and σ_{min}, it can be mathematically assumed for all $\xi \in \mathbb{R}^3$ and $x \in \Omega$ that

$$\sigma_{min}|\xi|^2 \leq \sum_{i,j=1}^{3} \sigma_{ij}(x)\xi_j\xi_k \leq \sigma_{max}|\xi|^2 . \tag{2.10}$$

Then it follows that the eigenvalues of σ are uniformly bounded from below and above by two strictly positive constants, denoted by σ_{min} and σ_{max}. Different distinctions can be made with respect to the distribution of the material parameters:

- material parameters independent of the position are called *homogeneous*
- a parameter dependent on the spatial position is termed *inhomogeneous*
- material parameters having different values in different spatial directions are called *anisotropic*
- material parameters depending on the amplitude of the applied fields are termed *nonlinear*
- parameters depending on the frequency or time of the applied fields are termed *dispersive*.

The relations (2.6) through (2.8) are usable when the medium is almost dispersion free in a broad frequency range. For a causal medium and when the constitutive relations depend on the time, Equations (2.6) and (2.7) must be written as convolution-type integrals (Mackay and Lakhtakia, 2010). Throughout this work linear, isotropic and inhomogeneous material parameters, which do not depend on time or frequency are

considered. This assumption reduces the tensor in (2.9) to a constant, scalar value and Ohm's law reads

$$\mathbf{J} = \sigma\mathbf{E} + \mathbf{J}^e. \tag{2.11}$$

This is also valid for the magnetic permeability and electrical permittivity. Throughout this thesis, constant values are used for both. These values are the magnetic permeability and electrical permittivity for the free space

$$\mu = \mu_0 = 4\pi \times 10^{-7}, \tag{2.12a}$$

$$\varepsilon = \varepsilon_0 = \left(\mu_0 c^2\right)^{-1}. \tag{2.12b}$$

Therein, c is the speed of light in vacuum.

2.3 Maxwell's equations

Maxwell equations are known as the fundamental, complete description of the behavior between electric and magnetic fields (Jackson, 1999). They consist of two vectorial equations and two scalar equations

$$\nabla \times \mathbf{E} + \frac{\partial \mathbf{B}}{\partial t} = \mathbf{0}, \tag{2.13a}$$

$$\nabla \times \mathbf{H} - \frac{\partial \mathbf{D}}{\partial t} = \mathbf{J}, \tag{2.13b}$$

$$\nabla \cdot \mathbf{D} = \rho_e, \tag{2.13c}$$

$$\nabla \cdot \mathbf{B} = 0. \tag{2.13d}$$

Faraday's law (2.13a) describes that circulating electric fields are generated by time-varying magnetic fields. Maxwell-Ampere's law (2.13b) states that the sum of electrical currents and time-varying electric fields produce circulating magnetic fields. The Gauss law for magnetism (2.13d) and Gauss law for electricity (2.13c) state that there are no magnetic monopoles and the electric field diverges from electrical charges.In this form, Maxwell's equations are valid in a resting or moving inertial reference frame, in which materials are at rest. Fourier transform in time of Equations (2.13a) through (2.13d) and

using constitutive relations and Ohm's law leads to:

$$\nabla \times \mathbf{E} - i\omega\mu_0\mathbf{H} = \mathbf{0}, \tag{2.14a}$$

$$\nabla \times \mathbf{H} + i\omega\varepsilon_0\mathbf{E} = \sigma\mathbf{E} + \mathbf{J}^e, \tag{2.14b}$$

$$\nabla \cdot (\varepsilon_0\mathbf{E}) = \rho_e, \tag{2.14c}$$

$$\nabla \cdot (\mu_0\mathbf{H}) = 0. \tag{2.14d}$$

Equations (2.14a - 2.14d) are Maxwell's equations in the frequency domain. Both sets of equations are suitable for magnetotelluric modelling, whereas the frequency domain equations are used more often as the time domain version (de la Kethulle de Ryhove and Mittet, 2014). Furthermore, Amperes law can be rewritten using a notation as $\hat{\sigma} = \sigma - i\omega\varepsilon_0$, introducing the complex conductivity $\hat{\sigma}$.

2.3.1 Electromagnetic vector potential formulations

As a result of the Helmholtz theorem, every vector field can be decomposed in a part that is divergence free and in a part that is curl free (Girault and Raviart, 2012, Theorem 3.5). To derive a formulation of differential equation using vector potentials, the electrical field intensity and the magnetic flux density will be decomposed as described in Huray (2011):

$$\mathbf{E} = \nabla \times \mathbf{F} - \nabla\psi, \tag{2.15}$$

$$\mathbf{B} = \nabla \times \mathbf{A} - \nabla\chi. \tag{2.16}$$

Here $\mathbf{F}$ and $\mathbf{A}$ are the vector potentials corresponding to the fields $\mathbf{E}$ and $\mathbf{B}$. While the associated scalar fields are ψ and χ. This transformation allows a different way of describing electromagnetic fields. It is not only a different mathematical formulation, the converse argument is also true: electromagnetic phenomena can be either described by the fields $\mathbf{E}$ and $\mathbf{B}$ *or* by using potentials from which $\mathbf{E}$ and $\mathbf{B}$ can be derived. Both can exist independently of each other and the Aharonov-Bohm effect (Aharonov and Bohm, 1959) shows the existence of electromagnetic potentials even if $\mathbf{E}$ and $\mathbf{B}$ are zero.
Following Tyler et al. (2004), inserting Equations (2.15 - 2.16) into (2.13a) gives

$$\begin{aligned}
\nabla \times \mathbf{E} + \partial_t(\nabla \times \mathbf{A} - \nabla\chi) &= \nabla \times (\nabla \times \mathbf{F} - \nabla\psi) + \partial_t(\nabla \times \mathbf{A} - \nabla\chi) \\
&= \nabla \times \nabla \times \mathbf{F} + \partial_t(\nabla \times \mathbf{A}) - \partial_t\nabla\chi \\
&= \nabla^2\mathbf{F} - \nabla(\nabla \cdot \mathbf{F}) + \partial_t(\nabla \times \mathbf{A}) - \partial_t\nabla\chi \\
&= \mathbf{0}.
\end{aligned} \tag{2.17}$$

Also, by inserting Equations (2.15) and (2.16) into (2.13b) and using (2.6) gives

$$\begin{aligned}\nabla \times \mathbf{B} - \mu_0\mathbf{J} - \mu_0\varepsilon_0\partial_t(\nabla \times \mathbf{F} - \nabla\psi) &= \nabla^2\mathbf{A} - \nabla(\nabla \cdot \mathbf{A}) - \mu_0\mathbf{J} - \mu_0\varepsilon_0\partial_t(\nabla \times \mathbf{F} - \nabla\psi) \\ &= \nabla^2\mathbf{A} - \nabla(\nabla \cdot \mathbf{A}) - \mu_0\sigma(\nabla \times \mathbf{F} - \nabla\psi) \\ &\quad - \mu_0\varepsilon_0\partial_t(\nabla \times \mathbf{F} - \nabla\psi) \\ &= \mu_0\mathbf{J}^e.\end{aligned} \tag{2.18}$$

To proceed, the divergence is applied to Equation (2.13b) together with Ohm's law and Equation (2.15) is inserted :

$$\begin{aligned}\nabla \cdot (\mu_0\sigma\mathbf{E} + \mu_0\mathbf{J}^e - \mu_0\varepsilon_0\partial_t\mathbf{E}) &= \nabla \cdot (\mu_0\sigma(\nabla \times \mathbf{F} - \nabla\psi) - \mu_0\varepsilon_0\partial_t(\nabla \times \mathbf{F} - \nabla\psi) + \mu_0\mathbf{J}^e) \\ &= \nabla \cdot \mu_0 \left(\sigma\nabla \times \mathbf{F} - \sigma\nabla\psi - \varepsilon_0\partial_t(\nabla \times \mathbf{F}) - \varepsilon_0\partial_t\nabla\psi + \mathbf{J}^e\right) \\ &= \mathbf{0}.\end{aligned} \tag{2.19}$$

Now, arriving at three Equations (2.17-2.19) for the decomposition of Maxwell's Equation, they need to be decoupled and written only in terms of one vector potential. By inserting the decomposition (2.16) into Gauss' law (2.13d) a homogeneous Poisson equation for χ could be derived. A natural choice is to specify $\chi = 0$ at boundaries of the computational domain and as consequence χ will also be zero all over the domain. Using this assumption allows rewriting Equation (2.17) as

$$\nabla \times \mathbf{F} + \partial_t\mathbf{A} + \nabla\xi = \mathbf{0}, \tag{2.20}$$

because χ vanishes in Equation (2.17). The last term $\nabla\xi$ results from the fact, that every vector field whose curl is zero, can be written as a gradient of some scalar function which was introduced here as ξ. Using Equation (2.20) and the identity $\nabla \times \nabla \times \mathbf{A} = \nabla^2\mathbf{A} - \nabla(\nabla \cdot \mathbf{A})$, it is now possible to eliminate $\mathbf{F}$ from Equations (2.18) and (2.19)

$$\begin{aligned}\nabla^2\mathbf{A} - \nabla(\nabla \cdot \mathbf{A}) - \mu_0\sigma(\nabla \times \mathbf{F} - \nabla\psi) - \mu_0\varepsilon_0\partial_t(\nabla \times \mathbf{F} - \nabla\psi) & \\ = \nabla^2\mathbf{A} - \nabla(\nabla \cdot \mathbf{A}) - \mu_0\sigma(\partial_t\mathbf{A} - (\nabla\psi + \nabla\xi)) & \\ - \varepsilon_0\mu_0\partial_t(\partial_t\mathbf{A} - (\nabla\psi + \nabla\xi)) & \\ = \mu_0\mathbf{J}^e. &\end{aligned} \tag{2.21}$$

By using $\phi = \psi + \xi$ Equation (2.21) can finally be written as

$$\nabla^2\mathbf{A} - \nabla(\nabla \cdot \mathbf{A}) - \mu_0\sigma\partial_t\mathbf{A} - \mu_0\sigma\nabla\phi - \varepsilon_0\mu_0\partial_t\partial_t\mathbf{A} - \varepsilon_0\mu_0\partial_t\nabla\phi = \mu_0\mathbf{J}^e, \tag{2.22}$$

and also Equation (2.19) becomes

$$\nabla \cdot (\sigma \nabla \phi - \sigma \partial_t \mathbf{A} - \mu_0 \varepsilon_0 \partial_t \partial_t \mathbf{A} - \varepsilon_0 \partial_t \nabla \phi + \mu_0 \mathbf{J}^e) = 0. \tag{2.23}$$

Both equations are now decoupled from $\mathbf{F}$ and are also independent of ξ. This is a partial differential equation system with four equations and four scalar unknowns, which is rather diagonal dominant as well as weakly coupled, as noted by Aruliah (2001).

Comparing Equations (2.22) and (2.23) with (2.13a) and (2.13b), the relation between $(\mathbf{E}, \mathbf{B})$ and $(\mathbf{A}, \phi)$ is now given by

$$\mathbf{B} = \nabla \times \mathbf{A} \tag{2.24}$$

and

$$\mathbf{E} = -\partial_t \mathbf{A} - \nabla \phi. \tag{2.25}$$

Equation (2.24) can also be seen as a direct consequence of Equation (2.13d), because $\mathbf{B}$ is a solenoidal vector field (Girault and Raviart, 2012, Corollary 3.4). By using Faraday's law (2.13a), Equation (2.25) can be written as:

$$\nabla \times (\mathbf{E} + \partial_t \mathbf{A}) = \mathbf{0}. \tag{2.26}$$

Every vector field, whose curl is zero, can be written as a gradient of some scalar function (Zhdanov, 2009):

$$(\mathbf{E} + \partial_t \mathbf{A}) = -\nabla \phi. \tag{2.27}$$

This gives an expression for the electric field in terms of magnetic vector potential $\mathbf{A}$ and a gradient of some scalar potential, which is Equation (2.25).

2.3.2 Gauging conditions

The vector field $\mathbf{A}$ is not uniquely determined, since Equation (2.24) only specifies the curl of $\mathbf{A}$. Hence, a gauge procedure is needed to ensure uniqueness of the potentials. This is important from the computational point of view, not from the physical aspect. If the system is not unique, every potential could also give exactly the same[1] electromagnetic fields, as noted also by Biro and Preis (1989). But if non uniqueness occurred, discretisations will raise to singular or ill-conditioned algebraic systems. As pointed out by Fernandes (1995),

[1] Adding an arbitrary function f to the potential $\mathbf{A}$ which satisfy $\nabla \times \nabla f \equiv \mathbf{0}$ gives exactly the same magnetic field as defined in Equation (2.24).

'gauging ensures setting conditions on potentials that makes a one-to-one correspondence between field solutions and potential solutions'. Gauging conditions are needed for the uniqueness of the potentials, but they are also used to prove existence and uniqueness of solutions calculated from different vector potential formulations (Fernandes, 1995; Kordy, 2014). Rather than choosing a gauging function which sets the potential unique, a constraint on $\mathbf{A}$ can be imposed to ensure uniqueness.
Mostly, two different gauging procedures are commonly described in the literature. The first one, the *Coulomb gauge* is established by:

$$\nabla \cdot \mathbf{A} = \mathbf{0}. \tag{2.28}$$

Now, the curl of $\mathbf{A}$ is set with Equation (2.24) and also the divergence is determined by Equation (2.28). Another popular choice is:

$$\nabla \cdot \mathbf{A} = -\mu_0 \hat{\sigma} \phi. \tag{2.29}$$

Equation (2.29) is called *Lorenz gauge*[2] (Bossavit, 1999; Kordy et al., 2015) and relates the divergence of the vector potential $\mathbf{A}$ to the scalar ϕ. Both conditions can be transformed into one other by specifying a gauge function (Jackson, 2002) and both are useful to derive different partial differential systems for calculating electromagnetic phenomena e.g. (Biro and Preis, 1989; Bryant et al., 1990, 1998; Biro et al., 1996).

2.3.3 Gauged vector potential formulations

Having the different gauge constrains at hand, vector potential formulations for general three-dimensional computations can be derived. They are the basic formulations to simulate magnetotelluric fields for a given three-dimensional conductivity structure. Starting with Equation (2.22) by applying the Fourier transformation gives

$$\nabla^2 \mathbf{A} - \nabla(\nabla \cdot \mathbf{A}) + i\omega\mu_0\sigma\mathbf{A} - \mu_0\sigma\nabla\phi + \omega^2\varepsilon_0\mu_0\mathbf{A} + i\omega\varepsilon_0\mu_0\nabla\phi = -\mu_0\mathbf{J}^e. \tag{2.30}$$

Rearranging and ordering terms gives

$$\nabla^2 \mathbf{A} - \nabla(\nabla \cdot \mathbf{A}) + i\omega\mu_0\hat{\sigma}\mathbf{A} + \hat{\sigma}\mu_0\nabla\phi = -\mu_0\mathbf{J}^e. \tag{2.31}$$

[2]The condition is correctly called *Lorenz* gauge and not Lorentz, as often erroneously written (Sihvola, 1991).

Using the gradient on Equation (2.29), inserting it in Equation (2.31) and rearranging terms leads to

$$\nabla(\nabla \cdot \mathbf{A}) = -\nabla(\mu_0 \hat{\sigma} \phi) = -(\mu_0 \nabla \hat{\sigma} \phi + \mu_0 \hat{\sigma} \nabla \phi). \tag{2.32}$$

Finally, by inserting Equation (2.32) into (2.30), leads to

$$\nabla^2 \mathbf{A} + i\omega\mu_0 \hat{\sigma} \mathbf{A} + \mu_0 \phi \nabla \hat{\sigma} = -\mu_0 \mathbf{J}^e. \tag{2.33}$$

Inspecting Equation (2.33), four unknowns (A_x, A_y, A_z, ϕ) are embedded into this system with three equations. To complete it, one additional condition is needed which weakly couples the partial differential equations. Here, in accordance to several other authors e.g. (Aruliah et al., 2001; Aruliah, 2001; Tyler et al., 2004; Weiss, 2013) Equation (2.23) can be used to close the system. Transforming this equation to the frequency domain gives

$$\nabla \cdot \left(\sigma \nabla \phi + i\omega \hat{\sigma} \mathbf{A} - \mu_0 \omega^2 \varepsilon_0 \mathbf{A} + i\omega\mu_0 \varepsilon_0 \nabla \phi \right) = -\mu_0 \mathbf{J}^e. \tag{2.34}$$

Using the divergence, as well as the Lorenz gauge (2.29) and rearranging terms leads to

$$\nabla \cdot (\sigma \nabla \phi) - i\omega\varepsilon_0 \nabla \cdot (\nabla \phi) - i\omega\varepsilon_0\mu_0 \nabla \cdot (\nabla \phi) + i\omega\sigma\mu_0 \hat{\sigma} \phi - \mu_0 \omega^2 \varepsilon_0 \mu_0 \hat{\sigma} \phi = -\mu_0 \mathbf{J}^e, \tag{2.35}$$

and finally to

$$\nabla \cdot (\hat{\sigma} \nabla \phi) + i\omega \hat{\sigma} \mu_0 \hat{\sigma} \phi - i\omega \mathbf{A} \cdot \nabla \hat{\sigma} = \nabla \cdot \mathbf{J}^e. \tag{2.36}$$

At this point, Equations (2.33) and (2.36) can be used together to determine the vector potential $\mathbf{A}$ as well as the scalar ϕ for a given conductivity distribution and frequency. Afterwards, the electric and magnetic field can be derived through relations (2.24) and (2.25). As Tyler et al. (2004) point out, Equations (2.33) and (2.36) are almost equal for different gauging constrains and can be written in a general form, in which different gauging lead to different coefficients.

By using the gauging constrain (2.28), a similar set of differential equations can be derived. Following the same mathematical steps as before, Equation (2.33) changes to:

$$\nabla^2 \mathbf{A} + i\omega\mu_0 \hat{\sigma} \mathbf{A} - \mu_0 \hat{\sigma} \nabla \phi = -\mu_0 \mathbf{J}^e. \tag{2.37}$$

Again, Equation (2.37) comprises three differential equations involving four different unknowns. Thus, an additional statement has to close the system. In the case of Coulomb gauging,

$$\nabla \cdot (\hat{\sigma} \nabla \phi) - i\omega \nabla \cdot (\hat{\sigma} \mathbf{A}) = \nabla \cdot \mathbf{J}^e \tag{2.38}$$

can be used for this purpose. By using Equations (2.37) and (2.38) together, an operator form notation of the system is

$$\begin{pmatrix} C_x & 0 & 0 & P_x \\ 0 & C_y & 0 & P_y \\ 0 & 0 & C_z & P_z \\ P_x & P_y & P_z & D \end{pmatrix} \begin{pmatrix} A_x \\ A_y \\ A_z \\ \phi \end{pmatrix} = \begin{pmatrix} -\mu_0 J_x^e \\ -\mu_0 J_y^e \\ -\mu_0 J_z^e \\ \nabla \cdot \mathbf{J}^e \end{pmatrix}. \tag{2.39}$$

The coefficient matrix can be composed according to the used gauge formulation. Using Coulomb gauging, the diagonal coefficients are $C_{x,y,z} = \nabla^2 + i\omega\mu_0\hat{\sigma}$ and $D = \nabla \cdot (\hat{\sigma}\nabla)$. The off diagonal coupling terms are, in this case, component wise representations of $P_i = \mu_0\hat{\sigma}\partial_i\phi,\ i \in \{x, y, z\}$. Using Lorenz gauging, the coefficients have to be changed accordingly.
Finally, a table is compiled to give an overview for the different coefficients and terms occurring in the system (2.39). Table 2.3 summarizes the used terms and coefficients.

Gauge	$C_{x,y,z}$	D	$P_{x,y,z}$
Lorenz	$\nabla^2 + i\omega\mu_0\hat{\sigma}$	$\nabla \cdot (\hat{\sigma}\nabla) + i\omega\hat{\sigma}\mu_0\hat{\sigma}$	$\mu_0\phi\partial_{x,y,z}\hat{\sigma}$ $-i\omega\mathbf{A} \cdot \nabla\hat{\sigma}$
Coulomb	$\nabla^2 + i\omega\mu_0\hat{\sigma}$	$\nabla \cdot (\hat{\sigma}\nabla)$	$\mu_0\hat{\sigma}\partial_{x,y,z}\phi$ $-i\omega\nabla \cdot (\hat{\sigma}\mathbf{A})$

Table 2.3: Overview of the coefficients for the two gauging conditions in Equation (2.39)

Here, $C_{x,y,z}$ act on A_x, A_y, A_z according to the correct dimension, while the off-diagonal elements $P_{x,y,z}$ act in one case on the scalar potential ϕ and in another case $P_{x,y,z}$ on the vector potential $\mathbf{A}$. This can be seen also in the coefficient matrix of system (2.39). The first three entries of the last column act on the scalar potential, while the first three entries of the last row act on the vector potential. This fact is also included in Table 2.3, where two entries for $P_{x,y,z}$ for each gauging exists.

2.4 Interface and boundary conditions

Interface and boundary conditions define the behavior of electromagnetic fields at transitions of different materials or at the outer boundaries of the computational domain. With prior defined interface condition it is possible to derive a set of rules how the fields must behave at boundaries of the modelling domain. With defined boundary and interface

conditions, it is possible to formulate a boundary value problem, describing the correct physical behavior of the electromagnetic fields.

2.4.1 Electromagnetic interface conditions

Interface conditions are generally derived, for example, by using integral formulations of Maxwell's equations. Here, a different determination will be used based on Namias (1988) and Idemen (2011). Maxwell's equations (2.13b-2.13d) are presented in the differential formulation and the interface condition should be determined from these expressions. It is possible to derive interface conditions directly from the differential formulation with less effort. If the domain is separated by an interface $\Gamma_{1,2}$ into two different regions Ω_1 and Ω_2, as sketched in Figure 2.3 for example, it is always possible to express the surface of separation with an equation like $\varphi(\mathbf{x}) = 0, \forall \mathbf{x} \in \Gamma_{1,2}$. Also, the function will be positive $\varphi(\mathbf{x}_1) > 0$ for points in region Ω_1 and negative $\varphi(\mathbf{x}_2) < 0$ in region Ω_2. This is essentially the definition of a signed distance function (Osher and Fedkiw, 2006). To proceed, the electromagnetic fields in the complete domain can be written as

$$\mathbf{E} = \mathbf{E}_1\Theta(-\varphi) + \mathbf{E}_2\Theta(\varphi), \tag{2.40a}$$

$$\mathbf{D} = \mathbf{D}_1\Theta(-\varphi) + \mathbf{D}_2\Theta(\varphi), \tag{2.40b}$$

$$\mathbf{B} = \mathbf{B}_1\Theta(-\varphi) + \mathbf{B}_2\Theta(\varphi), \tag{2.40c}$$

$$\mathbf{H} = \mathbf{H}_1\Theta(-\varphi) + \mathbf{H}_2\Theta(\varphi). \tag{2.40d}$$

In which the Heavyside step function is defined, to separate both sides, by

$$\Theta(x) = \begin{cases} 1, & \text{if } x \geq 0 \\ 0, & \text{if } x < 0. \end{cases} \tag{2.41}$$

Inserting Equation (2.40b) into Gauss' law (2.13c), gives

$$\nabla \cdot \mathbf{D}_1\Theta(-\varphi) + \nabla \cdot \mathbf{D}_2\Theta(\varphi) + \mathbf{n} \cdot \left[(\mathbf{D}_2 - \mathbf{D}_1)\right]|\nabla\varphi|\,\delta(\varphi) = \rho_e. \tag{2.42}$$

Here, $\delta(\cdot)$ is the Dirac's delta-function. The last term results from the fact that $\nabla\Theta(\pm\varphi) = \pm\mathbf{n}|\nabla\varphi|\,\delta(\varphi)$, which is described by Idemen (2011). The same can be done for the charge density by splitting it for two regions:

$$\rho_e = \rho_{e1}\Theta(-\varphi) + \rho_{e2}\Theta(\varphi) + \rho_s|\nabla\varphi|\,\delta(\varphi). \tag{2.43}$$

The last summand in (2.43) includes a surface charge density ρ_s. Setting Equation (2.42) equal to (2.43), and comparing the resulting terms gives:

$$\mathbf{n} \cdot [\mathbf{D}]_{1,2} = \rho_s. \tag{2.44}$$

Equation (2.44) holds point-wise on $\Gamma_{1,2}$ and states a discontinuity of the electrical displacement field if a surface charge is present. As previously, $[\mathbf{D}]$ in Equation (2.44) is expressed by a limiting value as defined in Equation (2.5). For the tangential components of the magnetic field intensity, a similar procedure can be applied. Using Equation (2.40d) and (2.40b) together with Ampere's law (2.13b) gives

$$(\nabla\times\mathbf{H}_1)\Theta(-\varphi)+(\nabla\times\mathbf{H}_2)\Theta(\varphi)-\partial_t\mathbf{D}_1\Theta(-\varphi)-\partial_t\mathbf{D}_2\Theta(\varphi)-\mathbf{H}_1\times\nabla\Theta(-\varphi)-\mathbf{H}_2\times\nabla\Theta(\varphi) = \mathbf{J}. \tag{2.45}$$

Again, a relation for the right hand side of Equation (2.45), the electrical current density, can be given in analogy to Equation (2.43):

$$\mathbf{J} = \mathbf{J}_1\Theta(-\varphi) + \mathbf{J}_2\Theta(\varphi) + \mathbf{J}_s|\nabla\varphi|\,\delta(\varphi). \tag{2.46}$$

Grouping the terms of Equation (2.45) for the two regions and comparing them to (2.46), a condition of

$$\mathbf{n} \times [\mathbf{H}]_{1,2} = \mathbf{J}_s, \tag{2.47}$$

is derived. Here, a surface current $\mathbf{J}_s$ is involved. Also, similar interface conditions for the tangential components of $\mathbf{E}$ and the normal parts of $\mathbf{B}$ can be found

$$\mathbf{n} \cdot [\mathbf{B}]_{1,2} = 0, \tag{2.48}$$

$$\mathbf{n} \times [\mathbf{E}]_{1,2} = \mathbf{0}. \tag{2.49}$$

To summarize, possible discontinuities can occur at junctions of different media. For geophysical applications, the surface current in Equation (2.47) vanishes (Ward and Hohmann, 1988) and the tangential components of $\mathbf{H}$ will be continuous.
For the electromagnetic vector potential, interface conditions can be derived in a similar way,see Namias (1988):

$$\mathbf{A} = \mathbf{A}_1\Theta(-\varphi) + \mathbf{A}_2\Theta(\varphi), \tag{2.50a}$$

$$\phi = \phi_1\Theta(-\varphi) + \phi_2\Theta(\varphi). \tag{2.50b}$$

Using Equations (2.24) and (2.25) with (2.40a), (2.40c) gives

$$\mathbf{n} \times (\mathbf{A_1} - \mathbf{A_2}) |\nabla \varphi| \, \delta(\varphi) = \mathbf{0} \tag{2.51}$$

and

$$(\phi_1 - \phi_2) |\nabla \varphi| \, \delta(\varphi) = 0. \tag{2.52}$$

This induce the interface condition for the tangential part of the vector potential, which is continuous by

$$\mathbf{n} \times [\mathbf{A}]_{1,2} = \mathbf{0}, \tag{2.53}$$

as well as the continuity of the scalar potential

$$[\phi]_{1,2} = 0. \tag{2.54}$$

By using the Lorenz constrain Equation (2.29) together with Equation (2.50a), what is

$$\nabla \cdot \mathbf{A}_1 \Theta(-\varphi) + \nabla \cdot \mathbf{A}_2 \Theta(\varphi) + \nabla \mu_0 \hat{\sigma} \phi_1 \Theta(-\varphi) + \nabla \mu_0 \hat{\sigma} \phi_2 \Theta(\varphi) + \mathbf{n} \cdot \left[(\mathbf{A}_2 - \mathbf{A}_1) \right] |\nabla \varphi| \, \delta(\varphi) = 0, \tag{2.55}$$

gives the continuity of the normal part of the vector potential

$$\mathbf{n} \cdot [\mathbf{A}]_{1,2} = 0. \tag{2.56}$$

Inspecting Equation (2.53) as well as Equation (2.56), the complete set of interface conditions between two materials are given as

$$[\mathbf{A}]_{1,2} = 0, \tag{2.57a}$$

$$[\phi]_{1,2} = 0. \tag{2.57b}$$

The vector potential as well as the scalar potential are continuous between an interface. The tangential continuity (2.53) is caused by vanishing magnetic charges (2.13d) and using a Lorenz gauge constrain, the continuity of the vector potential in the normal direction is enforced.

2.4.2 Electromagnetic boundary conditions

To state a system of partial differential equations which solution is uniquely defined, boundary conditions have to be considered. At least two general kinds of boundary conditions can be used. If the computational domain is spatially bounded, interface conditions can be used to determine values of the fields along boundaries. Thereby,

in the outer domain fields are treated as given and in the inner computational domain fields at this interface can be calculated according to the defined interface conditions. Suppose that the outer boundaries of the computational domain Γ are divided into two separate parts, Γ^e and Γ^h whereat $\Gamma^e = \Gamma \setminus \Gamma^h$. With some predefined values $\mathbf{E}_0$ and $\mathbf{H}_0$ the following boundary conditions can be used:

$$\begin{aligned} \mathbf{n} \times \mathbf{E} &= \mathbf{n} \times \mathbf{E}_0 \quad \text{on } \Gamma^e, \\ \mathbf{n} \times \mathbf{H} &= \mathbf{n} \times \mathbf{H}_0 \quad \text{on } \Gamma^m. \end{aligned} \tag{2.58}$$

If the predefined fields are zero at the outer boundary, e.g. $\mathbf{E}_0 = \mathbf{0}$ and $\mathbf{H}_0 = \mathbf{0}$ they describe either a *perfect electric conductor* (PEC) or for the latter a *perfect magnetic conductor* (PMC). Due to their simplicity, they are often used in a lot of applications where simple conditions are sought after (Jin, 2015). In an oppositional case, when the outer boundary is absent or respectively extended to infinity, electromagnetic fields have to satisfy the Silver-Müller radiation conditions (Kirsch and Hettlich, 2015). Especially, if $\mathbf{x} \in \mathbb{R}^3$ and goes to infinity uniformly in all directions $\mathbf{x} \to \infty$, then

$$\begin{gathered} |\mathbf{x}|\mathbf{E}(\mathbf{x}, \omega) \text{ and } |\mathbf{x}|\mathbf{H}(\mathbf{x}, \omega) \text{ are bounded and} \\ \mathbf{E}(\mathbf{x}, \omega) + \frac{\mathbf{x}}{|\mathbf{x}|} \times \mathbf{H}(\mathbf{x}, \omega) = O\left(\frac{1}{|\mathbf{x}|}\right). \end{gathered} \tag{2.59}$$

A partial differential system using this conditions proves to have a unique solution, which was shown by Santos and Sheen (2000). To reduce the simulation costs and downsize the computational domain, in which the solution has to be calculated, the Silver-Müller radiation conditions can be approximated by an *absorbing boundary condition* (ABC) (Zyserman et al., 1999) in which is

$$\alpha \mathbf{P}_\tau \mathbf{E} + \mathbf{n} \times \mathbf{H} = 0 \quad \text{on } \Gamma. \tag{2.60}$$

These extended boundary conditions will absorb a plane wave travelling into the direction $\mathbf{n}$ to the boundary. Although, in context of magnetotellurics α is defined as

$$\alpha = \frac{1 - i}{\sqrt{2\omega}} \sqrt{\frac{\sigma}{\mu}}, \tag{2.61}$$

where σ and μ are positive, bounded functions. The projection of the trace operator on Γ is defined as $\mathbf{P}_\tau \mathbf{E} = -\mathbf{n} \times (\mathbf{n} \times \mathbf{E})$.

For geophysical applications using low and moderate frequency sources like magnetotellurics, the boundary influence is not as important as in high frequency wave scattering

applications, for example ground penetrating radar (GPR). Here, special care has to be taken into account when formulating boundary conditions, because errors, which arise at the boundaries, can populate into the entry solution (Gonzalez Huici, 2013). Electromagnetic vector potential formulations require different boundary conditions. Nevertheless, compared to Equations (2.58) similar conditions are given by Haber et al. (2000)

$$\begin{aligned} -\mathbf{n} \times (\nabla \times \mathbf{A}) &= \mathbf{0} \quad \text{on } \Gamma, \\ \mathbf{n} \cdot \mathbf{A} &= 0 \quad \text{on } \Gamma, \\ \mathbf{n} \cdot \nabla \phi &= 0 \quad \text{on } \Gamma, \\ \int_{\Omega} \phi \, d\Omega &= 0 \quad \text{in } \Omega. \end{aligned} \tag{2.62}$$

In case of a magnetotelluric simulation, simplified boundary conditions can be applied in contrast to Equations (2.62). This will be explored in the subsequent chapter about the magnetotelluric model.

2.5 Induction into two-dimensional conductivity structures

Besides a general three-dimensional formulation, simplifications can be made if the underlying conductivity structure has variations only in two spatial directions. In the direction, in which the conductivity structure does not change, the source fields are constant and the directional derivatives of the conductivity vanish. This direction is often called *strike direction*. This simplification decouples Maxwell's equations into two independent sets of equations. The first set derived from Equations (2.14a - 2.14b) is

$$\frac{\partial H_z}{\partial y} - \frac{\partial H_y}{\partial z} = \hat{\sigma} E_x + J_x^e, \tag{2.63a}$$

$$\frac{\partial E_x}{\partial z} = -i\omega\mu_0 H_y, \tag{2.63b}$$

$$-\frac{\partial E_x}{\partial y} = -i\omega\mu_0 H_z. \tag{2.63c}$$

In this set of equations, the electrical field E_x is the only component in the direction of strike and hence it is called *TE-mode* (or *E-polarization*). The opposed set is subsequently

called the *TM-mode* (or *B-polarization*)

$$\frac{\partial E_z}{\partial y} - \frac{\partial E_y}{\partial z} = -i\omega\mu_0 H_x, \tag{2.64a}$$

$$\frac{\partial H_x}{\partial z} = \hat{\sigma} E_y + J_y^e, \tag{2.64b}$$

$$-\frac{\partial H_x}{\partial y} = \hat{\sigma} E_z + J_z^e. \tag{2.64c}$$

Within the TE-Mode, electrical currents are parallel to the strike direction and in the TM-mode perpendicular to the strike direction. Both modes are driven by a generating

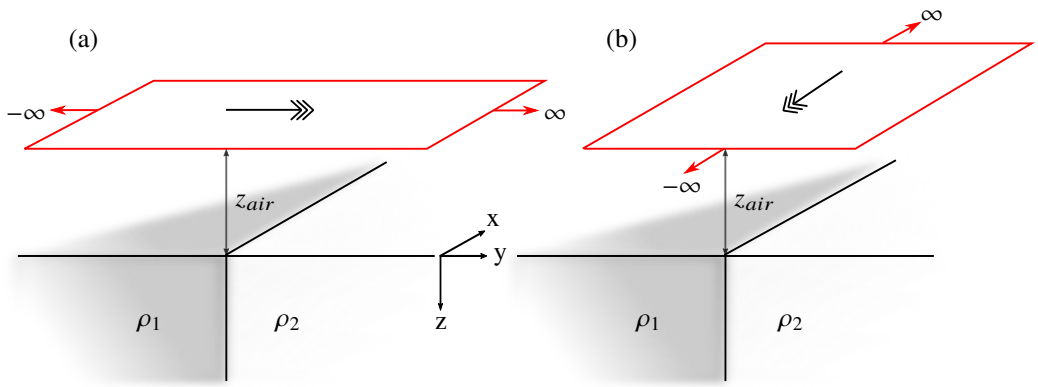

Figure 2.4: Schematic representation of the two-dimensional magnetotelluric modes. (a) TM-mode, where a uniform sheet current at a height z_{air} in the y-direction is extended to infinity. (b) TE-mode, where a uniform sheet current at a height z_{air} in the x-direction is extended to infinity. In both sketches two unequal conductivities are present ($\sigma_1 \neq \sigma_2$) (modified, after (Chave and Jones, 2012).)

current systems at a height $z_{air} < 0$. Assuming that the z-direction is positive downwards (see Figure 2.4), by inspecting Equations (2.64b) and (2.64c), the magnetic field H_x is constant in the non-conducting air half-space. For the TE-mode a horizontal sheet current of the form

$$\mathbf{J}^e = -H_x^0 \delta(z - z_{air}) \hat{\mathbf{e}}_x, \tag{2.65}$$

at height z_{air} can be assumed, which produces a two-dimensional inducing magnetic field in the air half-space. For the TM-mode a source term

$$\mathbf{J}^e = H_x^0 \delta(z - z_{air}) \hat{\mathbf{e}}_y, \tag{2.66}$$

can be assumed (Chave and Jones, 2012). The sources are coupled to the conductive half-space only by induction and not by galvanic contact. But since H_x is constant in the air half-space, it can be set to $H_x(y, z = 0) = H_0$ at the air-Earth interface for the

TM-mode. The air half-space doesn't have to be modelled, whereas in the TE-mode the air half-space has to be considered.
A second order differential equation can be derived for both modes. First, for the TE-mode, inserting Equations (2.63b) and (2.63c) into (2.63a) gives

$$\nabla \cdot (\mu_0^{-1} \nabla E_x) - i\omega\hat{\sigma} E_x = -i\omega H_x^0 \delta(z - z_{air}). \tag{2.67}$$

Also, for the TM-mode, rearranging Equations (2.64b) as well as (2.64c) into (2.64a) gives

$$\nabla \cdot (\hat{\sigma}^{-1} \nabla H_x) - i\omega\mu_0 H_x = 0. \tag{2.68}$$

In order to model the electrical field, the partial equation for the TE-mode has to be used. If the magnetic field is required, the second order partial differential equation for the magnetic field has to be utilised.
If Equation (2.67) is multiplied by μ_0, or Equation (2.68) by $\hat{\sigma}$ (if a homogeneous conducting half-space is present) a simplification in the notation can be introduced by writing:

$$k^2 = i\omega\mu_0\hat{\sigma}. \tag{2.69}$$

Here, k defines a wave number that implies the equality of the real and imaginary part of this absorption coefficient

$$k = e^{(\pi/4)i}(\omega\mu_0\hat{\sigma})^{1/2} = (1+i)(\omega\mu_0\hat{\sigma}/2)^{1/2}. \tag{2.70}$$

Examining the differential equation for the electrical field (2.67) at interfaces Γ_{int}, it must hold

$$[E_x]_{\Gamma_{int}} = 0, \tag{2.71a}$$

$$\mathbf{n} \cdot [\nabla E_x]_{\Gamma_{int}} = 0. \tag{2.71b}$$

At an interface between different conductivities the electrical field is continuous as well as its normal derivative. For the TM-mode examining Equation (2.68) reveals, that

$$[H_x]_{\Gamma_{int}} = 0, \tag{2.72a}$$

$$\mathbf{n} \cdot \left[\sigma^{-1} \nabla H_x\right]_{\Gamma_{int}} = 0. \tag{2.72b}$$

Assuming conductivity inhomogeneities far away from the outer boundaries, simple one-dimensional analytical solutions as described, for example by Wait (1953) for a

layered half-space, can be used as Dirichlet boundary conditions.

2.6 Second order formulations

Having introduced all necessary preconditions to formulate the boundary value problems, the main formulations for the two- and three-dimensional case will be given. First, the general case for the Lorenz and Coulomb gauged vector potential formulation will be considered and later on the two-dimensional case will follow. Using formulations for the vector potential, the task is to find $\mathbf{A}$ and ϕ such that

$$\begin{aligned}
\nabla^2\mathbf{A} + i\omega\mu_0\hat{\sigma}\mathbf{A} + \mu_0\phi\nabla\hat{\sigma} &= -\mu_0\mathbf{J}^e && \text{in } \Omega,\\
\nabla\cdot(\hat{\sigma}\nabla\phi) + i\omega\hat{\sigma}\mu_0\hat{\sigma}\phi - i\omega\mathbf{A}\cdot\nabla\sigma &= \nabla\cdot\mathbf{J}^e && \text{in } \Omega,\\
-\mathbf{n}\times(\nabla\times\mathbf{A}) &= \mathbf{0} && \text{on } \Gamma,\\
\mathbf{n}\cdot\mathbf{A} &= 0 && \text{on } \Gamma,\\
\mathbf{n}\cdot\nabla\phi &= 0 && \text{on } \Gamma,\\
\int_\Omega \phi\, d\Omega &= 0 && \text{in } \Omega,\\
[\mathbf{A}]_{1,2} &= 0 && \text{on } \Gamma^{int},\\
[\phi]_{1,2} &= 0 && \text{on } \Gamma^{int}.
\end{aligned} \tag{2.73}$$

The boundary value problem (2.73) can be used to find an approximation for the desired electromagnetic fields. The constraint equation can be replaced by setting $\phi = 0$ at some point on the boundary. This is commonly done in fluid simulations, where the pressure must be constrained in the same way (Girault and Raviart, 2012). In the same manner, a boundary value problem using the Coulomb gauging can be stated by interchanging Equations from (2.73) with Equations (2.37) and (2.38). For the two-dimensional problem, a set of two boundary value problems should be considered. The entire boundary value problem for the TE-mode is to find an E_x such that

$$\begin{aligned}
\nabla\cdot(\mu_0^{-1}\nabla E_x) - i\hat{\sigma}E_x &= -i\omega H_x^0\delta(z - z_{air}) && \text{in } \Omega,\\
E_x &= E_x^{1D} && \text{on } \Gamma^D,\\
[E_x]_{\Gamma_{int}} &= 0 && \text{on } \Gamma^{int},\\
\mathbf{n}\cdot[\nabla E_x]_{\Gamma_{int}} &= 0 && \text{on } \Gamma^{int}.
\end{aligned} \tag{2.74}$$

Combining equations (2.68) and (2.72a - 2.72b) gives the boundary value problem for the TM-mode, which is to find an H_x such that

$$\begin{aligned} \nabla \cdot (\hat{\sigma}^{-1} \nabla H_x) - i\omega\mu_0 H_x &= 0 && \text{in } \Omega \setminus \Omega_{air}, \\ H_x &= H_x^{1D} && \text{on } \Gamma^D, \\ [H_x]_{\Gamma_{int}} &= 0 && \text{on } \Gamma^{int}, \\ \mathbf{n} \cdot \left[\hat{\sigma}^{-1} \nabla H_x\right]_{\Gamma^{int}} &= 0 && \text{on } \Gamma^{int}. \end{aligned} \tag{2.75}$$

Assuming a quasi-uniform source term by setting it to zero in Equations (2.74) and (2.75) allows for imposing pre-calculated field values as boundary conditions.

2.7 The magnetotelluric model

Now, after describing Maxwell's equations, their generalizations and restrictions, an application to the magnetotelluric method will be represented in the next subsections. The outcome of these are boundary value problems which can be used to describe the induction within the Earth. They will be later discretized with meshless methods and applied to example calculations.

2.7.1 MT-Approximation - neglecting displacement currents

To use the Maxwell equations (2.14a - 2.14d) for magnetotelluric modelling, one assumption is to neglect displacement currents. However, the time-variation of magnetic induction is still important, but in magnetotellurics applications wave lengths are much larger than the physical domain. Inspecting Maxwell-Ampere's law (2.13b), this statement implies that $\partial_t \mathbf{D}$ is much smaller than the curl of the magnetic field or the total electric current density. Following Bossavit (1998) as well as de Castro et al. (2014), if L is the typical length of the induction process and ω a typical frecuency, dropping the displacement currents is valid if

$$|\omega||\mathbf{D}| \ll |\mathbf{H}|L^{-1} \text{ and } |\omega||\mathbf{D}| \ll |\sigma\mathbf{E}|. \tag{2.76}$$

Using Faraday's equation (2.13a) and the constitutive relation connecting the electrical field intensity with the magnetic flux gives

$$|\omega||\mathbf{E}| \approx |\omega||\mu_0\mathbf{H}|. \tag{2.77}$$

Inserting Equation (2.77) into (2.76) and rearranging the terms results in

$$L \ll \frac{1}{\sqrt{\epsilon_0 \mu_0}|\omega|}. \tag{2.78}$$

Thus, dropping the displacement currents is only valid if the wavelength of the electromagnetic field is much lager than the length scale L. Note that $(\epsilon_0\mu_0)^{-1/2}$ is the speed of light in vacuum. The second assumption from (2.76) is that a product of the electrical permittivity and the time is much smaller than the conductivity or otherwise formulated, the charge relaxation time is many orders of magnitude smaller than a typical period used in a magnetotellurics experiment:

$$\sigma^{-1}\epsilon_0|\omega| \ll 1. \tag{2.79}$$

The latter relation is more often recited when arguing that it is possible to drop the displacement current term in magnetotelluric applications. Assuming a typical magnetotelluric frequency of $\omega = 2\pi \times 10^{-1}\,\mathrm{rad\,s^{-1}}$ and conductivity $\sigma_{Earth} = 0.01\ \mathrm{S\,m^{-1}}$, the estimations

$$L \ll \frac{1}{\sqrt{\epsilon_0 \mu_0}|\omega|} = 10^{10}\,\mathrm{m} \ \text{ and } \ \sigma^{-1}\epsilon_0|\omega| = 5.6 \times 10^{-8} \tag{2.80}$$

give an appropriate reason to drop the displacement currents from Maxwell's equations in common magnetotelluric experiments.
Rewriting Equations (2.14a - 2.14d) without displacement currents will describe the *eddy-current approximation*[3] or *quasi-static approximation* of Maxwell's equations

$$\nabla \times \mathbf{E} - i\omega\mu_0\mathbf{H} = \mathbf{0}, \tag{2.81a}$$

$$\nabla \times \mathbf{H} - \sigma\mathbf{E} = \mathbf{J}^e, \tag{2.81b}$$

$$\nabla \cdot (\epsilon_0\mathbf{E}) = \rho_e, \tag{2.81c}$$

$$\nabla \cdot (\mu_0\mathbf{H}) = 0. \tag{2.81d}$$

Mathematically, the equations changes from a hyperbolic partial differential system to a parabolic system. Using this formulation, all terms related to displacement currents can be neglected in boundary value problems like the proposed ones in sub-chapter 2.6. This amounts to change $\hat{\sigma}$ to σ in most cases.

[3] A name often used in the engineering literature (Kriezis et al., 1992)

2.7.2 Plane-wave approximation

Another physical assumption can be made if it is supposed that the current systems, which generates electromagnetic fields utilized by the magnetotelluric technique, are large-scale, homogeneous horizontal current sheets in the ionosphere. Due to the distance to Earth, they generate electromagnetic plane-waves normally incident on the Earth's surface. This key property lead to constant electromagnetic fields as exciting source and as consequence, a time-invariance of the magnetotelluric impedance tensor. The fields can now be written as

$$\mathbf{E} = \mathbf{E}_0 e^{(i\omega t - \mathbf{k}z)}, \tag{2.82a}$$

$$\mathbf{H} = \mathbf{H}_0 e^{(i\omega t - \mathbf{k}z)}, \tag{2.82b}$$

with constant amplitudes $\mathbf{E}_0$ and $\mathbf{H}_0$ and a wave number $\mathbf{k}$. If periods considered within less than a time scale of a day, Earth's curvature is negligible and all calculations are valid in a flat model description using Cartesian coordinates, as shown by Srivastava (1965). For magnetotelluric simulations, different versions of the modelling domain, corresponding to the used dimensionality, displayed in Figure 2.3 are adoptable.

2.7.3 Secondary field approach

A common approach, not only applied in magnetotellurics, is to split the electromagnetic fields into a part given by a known primary field and a secondary field that has to be calculated. In this approach, the primary field should be easily calculated and in magnetotelluric modelling a simple layered half-space model is used, for which the solution is analytically given. The secondary field is generated by anomalous conductivity structures. Splitting the fields, yields into a primary part and a secondary part in

$$\mathbf{E} = \mathbf{E}^p + \mathbf{E}^s, \tag{2.83a}$$

$$\mathbf{H} = \mathbf{H}^p + \mathbf{H}^s. \tag{2.83b}$$

The primary fields in (2.83a) and (2.83b) satisfies Maxwell's equations, assuming no source currents are applied in a simple half-space or layered model. Subsequently, Maxwell's equations for the secondary fields including the primary parts as sources read

$$\nabla \times \mathbf{E}^s - i\omega\mu_0 \mathbf{H}^s = i\omega\mu_0 \mathbf{H}^p, \tag{2.84a}$$

$$\nabla \times \mathbf{H}^s - \sigma \mathbf{E}^s = \Delta\sigma \mathbf{E}^p. \tag{2.84b}$$

In (2.84b) the difference is $\Delta\sigma = \sigma - \sigma^p$, in which σ^p is the conductivity of the one-dimensional layered background. Solving for the secondary field is numerically beneficial, because the primary field is calculated by a simple analytical expression and also the secondary field is often significantly smaller than the primary fields (Coggon, 1971; Livelybrooks, 1993; Wannamaker et al., 1985; Rätz, 2000).

2.7.4 Secondary field formulation for three dimensional conductivity structures

For a three-dimensional case the electromagnetic potentials can be separated into a primary and secondary part as well:

$$\mathbf{A} = \mathbf{A}^p + \mathbf{A}^s, \tag{2.85a}$$

$$\phi = \phi^p + \phi^s. \tag{2.85b}$$

This changes the boundary value problem (2.73) and the task is to find a $\mathbf{A^s}$ and ϕ such that

$$\nabla^2\mathbf{A}^s + i\omega\mu_0\hat{\sigma}\mathbf{A}^s + \mu_0\phi^s\nabla\hat{\sigma} = -\mu_0\Delta\sigma\mathbf{E}^p \quad \text{in } \Omega, \tag{2.86a}$$

$$\nabla\cdot(\hat{\sigma}\nabla\phi^s) + i\omega\hat{\sigma}\mu_0\hat{\sigma}\phi^s - i\omega\mathbf{A}^s\cdot\nabla\sigma = \nabla\cdot\Delta\sigma\mathbf{E}^p \quad \text{in } \Omega, \tag{2.86b}$$

$$\mathbf{n}\cdot\mathbf{A} = 0 \quad \text{on } \Gamma, \tag{2.86c}$$

$$\mathbf{n}\cdot\nabla\phi = 0 \quad \text{on } \Gamma, \tag{2.86d}$$

$$[\mathbf{A}]_{1,2} = 0 \quad \text{on } \Gamma^{int}, \tag{2.86e}$$

$$[\phi]_{1,2} = 0 \quad \text{on } \Gamma^{int}. \tag{2.86f}$$

The primary part of the field enters the system as an electrical field generated by a simple conductivity structure.

2.7.5 Secondary field formulation for two dimensional conductivity structures

The two sets of Maxwell equations for a two-dimensional conductivity structure can also be applied to a splitted field. The resulting differential equations for the secondary fields differ only in adding a non-zero source term, which results from a conductivity difference multiplied by some pre-calculated field values. Solving the TE-mode secondary field

gives the following boundary value problem to find an E_x such that

$$\begin{aligned} \nabla \cdot (\mu_0^{-1} \nabla E_x^s) - i\omega\sigma E_x^s &= i\omega\Delta\sigma E_x^p \quad \text{in } \Omega, \\ E_x^s &= 0 \qquad\qquad \text{on } \Gamma^D, \\ \left[E_x^s\right]_{\Gamma_{int}} &= 0 \qquad\qquad \text{on } \Gamma^{int}, \\ \mathbf{n} \cdot \left[\nabla E_x^s\right]_{\Gamma_{int}} &= 0 \qquad\qquad \text{on } \Gamma^{int}. \end{aligned} \tag{2.87}$$

As previous, $\Delta\sigma = \sigma - \sigma^p$ is the difference between a composed conductivity distribution and the layered host. Using the same splitting for the magnetic field, a boundary value problem for the TM-mode is finding an H_x such that

$$\begin{aligned} \nabla \cdot (\sigma^{-1} \nabla H_x^s) - i\omega\mu_0 H_x^s &= \frac{\partial}{\partial z}\left(\frac{\sigma_p}{\sigma}\right) E_y^p + i\omega\mu_0 \left(1 - \frac{\sigma_p}{\sigma}\right) H_x^p \quad \text{on } \Omega \setminus \Omega_{air}, \\ H_x &= 0 \qquad\qquad \text{on } \Gamma^D, \\ \left[H_x^s\right]_{\Gamma_{int}} &= 0 \qquad\qquad \text{on } \Gamma^{int}, \\ \mathbf{n} \cdot \left[\sigma^{-1} \nabla H_x^s\right]_{\Gamma^{int}} &= 0 \qquad\qquad \text{on } \Gamma^{int}. \end{aligned} \tag{2.88}$$

Note, the right-hand side involves derivatives of the conductivity, which has to be carefully implemented into a numerical algorithm.

2.7.6 Magnetotelluric transfer functions

The primary method to present magnetotelluric results, is based on the concept of apparent resistivities and phases. They are both based on the conjunction of the magnetic and electrical field through the magnetotelluric impedance tensor. Assuming the horizontal magnetic field **H** measured at a point on or beneath the surface of Earth and an electrical horizontal field **E**, the magnetotelluric impedance is defined as

$$\mathbf{E} = \underline{\mathbf{Z}} \cdot \mathbf{H}. \tag{2.89}$$

This relation is fundamental to the magnetotelluric method and for Chave and Jones (2012) it "*is the point where experiment and theory is connected*". The impedance is a complex second-rank tensor $\underline{\mathbf{Z}} : \mathbb{R}^3 \to \mathbb{R}^{3\times 3}$ and its entries are populated according to the dimensionality of the conductivity structure. If the underlying conductivity structure is purely one-dimensional, the diagonal elements of the impedance tensor vanish and the off-diagonal entries are equal in amplitude, but have opposite signs. A two-dimensional conductivity structure generates diagonal entries, which are equal in amplitude and different in sign as well as off-diagonal elements, which are different to each other. For a

purely three-dimensional conductivity structure all entries are populated with different values. The tensor is frequency dependent according to the measured fields. If the conductivity structure is purely one-dimensional, the impedance reduces to

$$Z_{1D} = \frac{E_x}{H_y}. \tag{2.90}$$

Using Equation (2.90), the apparent resistivity can be calculated by

$$\rho_a(\omega) = \frac{1}{\omega\mu_0}|Z_{1D}(\omega)|^2, \tag{2.91}$$

$$\varphi(\omega) = \arg\left(Z_{1D}(\omega)\right) = \tan^{-1}\left(\frac{re(Z_{1D}(\omega))}{im(Z_{1D}(\omega))}\right). \tag{2.92}$$

These equations generalize up to three dimensions, in which the magnetotelluric impedance is fully a populated second-rank tensor. The apparent resistivity and phase is defined as

$$\rho_a^{ij}(\omega) = \frac{1}{\omega\mu_0}|Z^{ij}(\omega)|^2, \tag{2.93}$$

$$\varphi^{ij}(\omega) = \arg\left(Z^{ij}(\omega)\right) = \tan^{-1}\left(\frac{re(Z^{ij}(\omega))}{im(Z^{ij}(\omega))}\right). \tag{2.94}$$

Here, the impedance is Z^{ij} with $i, j \in \{x, y\}$ which are entries of the full impedance tensor. Calculating the apparent resistivities and phases for a three-dimensional simulation need to solve Equation (2.89) for the impedance. A more general treatment and description is given in Chave and Jones (2012). When using the two-dimensional formulation, the solution of the boundary value problem gives one field component: E_x or H_x. To calculate the apparent resistivity as well as the phase the corresponding complementary field (E_y or H_y) must be calculated by using Maxwell's equations.

2.8 Summary and Conclusions

In this chapter, the basic mathematical description for simulating a magnetotelluric experiment was derived. As introduced, this applied geophysical method is based on the comparison of electromagnetic fields measured on Earths surface. If a set of time series have been recorded, transfer functions can be derived through post-processing. In a simple case, apparent resistivities and phases for different time periods or frequencies are derived, which can be used to establish an understanding of the regional conductivity structure

beneath the measuring area. To simulate such experiment, a physical description has to be formulated in which electromagnetic fields can be represented by partial differential equation system depending on the conductivity of Earths surface.

To derive such mathematical abstraction, simplifications have to be made in order to capture the right physical behavior of this experiment. The first simplification is to lighten the geometrical description of the problem, where simulations take place. The modelling domain will be constructed from a simple convex polygon with a Lipschitz-continuous boundary. This simplification is mathematically important later on, because this implies that the computational domain automatically satisfy a so called cone condition (Mirzaei, 2015a).

As described, material parameters should be bounded from below and above. For the simplest case piece-wise constant material parameters will be used to describe a conductivity model defined by a simplified Earth geometry.

Starting from a general, time-dependent form of Maxwell's equations a simpler parabolic system, which describes the eddy current approximation in the frequency domain, was derived. To further simplify the mathematical description a vector potential ansatz is used. Here, the fields are continuous at material interfaces whereas in a formulation with electric and magnetic fields discontinuities occur. This simplifies the numerical implementation in a general three-dimensional modelling algorithm. In order to avoid the discretization of a coupled partial differential system, a weakly coupled second order system of partial differential equations based on the vector potential ansatz was derived. This procedure is commonly used in finite-element discretizations when standard node-based finite elements are used to discretize electromagnetic vector-valued problems (Boyse et al., 1992). In the sense Bossavit (1999) states: "... *the discrete analogue of the* $\nabla \times (\mu^{-1}\nabla \times \cdot)$ *operator, which is poor with nodal elements because of this property, precisely. To cure that, anything that will replace this operator by a Laplacian is good, hence the guiding idea of somehow introducing* $\nabla \cdot (\mu^{-1}\nabla)$.". To benefit from this, a meshless algorithm based on a Laplacian formulation will be used. While vector-valued discretizations are not common in the meshless community this formulation should be consistent with existing meshless schemes.

The resulting system of partial differential equations has almost the same form for different gauging constraints. A general implementation allows a variety of formulations, while the main discretization for a three-dimensional conductivity structure needs to be based on a properly gauged system.

When using two-dimensional conductivity structures, Maxwell's equations separate into two sets of differential equation systems. Defining a geological strike direction, the

electrical field is parallel in one of the formulations and in the other set a magnetic field parallel to the strike occurs. As before, the systems are converted into second order partial differential equations, which will be discretized by the meshless scheme. As in the electrical formulation, the field is continuous at conductivity interfaces, the behavior of the transversal magnetic mode is different. Here, a Laplacian operator $\nabla \cdot (\hat{\sigma}^{-1} \nabla H_x)$ appears in the formulation, while the conductivity $\hat{\sigma}$ can be discontinuous at material interfaces. This resembles the well-known elliptic interface problem (Peskin, 2002; Gong et al., 2008; Bennoune et al., 2016). The numerical scheme should be able to handle the continuity of the flux $\mathbf{n} \cdot \left[\hat{\sigma}^{-1} \nabla H_x\right]_{\Gamma^{int}} = 0$ and provide an appropriate discretization for this kind of physical behavior. An overview about different methods is given in the book of Li and Ito (2006). This topic will be addressed and discussed in an upcoming chapter.
The magnetotelluric model provides some further simplifications to the physical description. With considering adjusted time scales and dilatation of the induction process in a magnetotelluric experiment, Maxwell's equations change from a system of hyperbolic partial differential equations to a parabolic system. Also, the total electrical current density must be divergence-free, while changes in charge density do not lead to a magnetic field.
A popular way to simplify the numerical approach is to divide the electromagnetic fields into two separate parts, in which one is generated by a homogeneous or vertically layered conductivity structure. Analytical methods to calculate those fields are available and the numerical algorithm only needs to solve for the anomalous part.

Meshless methods for Maxwell's equations

This chapter is devoted to the development of a meshless magnetotelluric forward calculation scheme. The aim is to calculate electromagnetic fields influenced by a given Earth's conductivity structure. This computational scheme will be able to calculate the electromagnetic fields only with spatial distributed points inside the modelling domain, no fixed mesh or grid is needed. Here, the meshless technique will be adapted to model magnetotelluric experiments.

3.1 Introduction

Meshless methods for the discretization of partial differential equations have become a popular field of research during the last decades. Since mathematical modelling has turned into an important tool in science and engineering, the numerical solution of partial differential equations has also become a crucial part of this modelling process. A various bunch of classical numerical techniques like the *finite differences* method, *finite volume* method, or the *finite element* method, and several other techniques have been developed. All of these methods rely on the discrete representation of the modelling domain through a mesh or grid. This dependence is sometimes a drawback, especially when complex geometries are involved (Dolbow and Belytschko, 1999). In order to avoid using a mesh or a grid representation for the numerical simulation, a lot of research has been done in numerical methods and engineering applications. All of these newly developed meshless algorithms have in common, that they will construct a discretization *"only in terms on nodes"* as noted by Belytschko et al. (1994). Only the distribution and location of the points (or nodes[4]) are used to discretize a partial differential equation, no connections or fixed global relations have to be considered. This property is of growing importance in the mathematical, as well as the engineering scientific community.
The need for new approximation techniques besides established, long-time developed methods like finite elements, was primary the difficulty to handle and generate meshes for

[4]Here in this thesis, points will be called points and not nodes, as used in many publications on meshless methods.

complex geometries. Generating quality meshes for complex models is not a trivial task and requires a serious amount of time in the total cost of a simulation (Owen, 1998). This is even more tedious for three-dimensional problems and dynamic, time-dependent tasks, which needs re-meshing at every time step. Here, a prominent examples are problems in the computational mechanics, where crack growth simulations account for complex adapted meshes (Barsoum, 1976). Directly linked to this topic is the rapid development of massively parallel algorithms for solving partial differential equations. Today's hardware architectures involve more and more parallel computations, where several (up to several thousand) multi-core or multi-processor units are linked together while each one working on small pieces of the numerical problem. In this regime it is essential for the algorithm to reduce the cost of communication to a minimum (Gropp et al., 1999). Here, simple point sets with no direct link among each other are preferable to fully adapted meshes. Furthermore, by constructing meshless approximations with arbitrary order of continuity and by building high-order approximation schemes for partial differential equations, it is possible to outbid actual processor architecture, where huge amounts of floating-point operations are available. If custom tailored schemes are demanded for problems where traditional methods perform poorly, creating customized approximation spaces, where some (physical) constrains or special enrichment are embedded, is one of the preferred tasks for meshless methods (Nguyen et al., 2008).

Many of these new methods can be coarsely categorized into two different types of discretizations. On the one hand, particle methods (Li and Liu, 2007) have been developed to solve classical physical phenomena like atomic, molecular (Plimpton, 1995) or galaxy (Barnes and Hut, 1986) behaviour. Here, the motion of interacting particles are calculated on a Langrangian description of discrete and continuum physical systems. They enforce an approximate solution of the PDE, depending on the particle interaction and the density of their distribution (Li and Liu, 2007). On the other hand, a different approach used for meshless algorithms is a discretization obtained by using methods from data fitting. Here, for every point a surrounding subset of n neighbouring points, called stencil, is gathered while the union of these local patches form an overlapping cover of the computational domain. This scheme is briefly diagrammed in Figure 3.5. Within these patches, local approximation or interpolation methods are used to generate meshless approximation functions. These functions, often called *shape functions*, are used to span finite dimensional meshless trial spaces to be used in a Galerkin or strong form collocation framework for solving a partial differential equation. In this step, several methods from the multivariate approximation theory can be chosen to set-up a linear system of equations which raises to a solution of the mathematical problem. It can be distinguished between

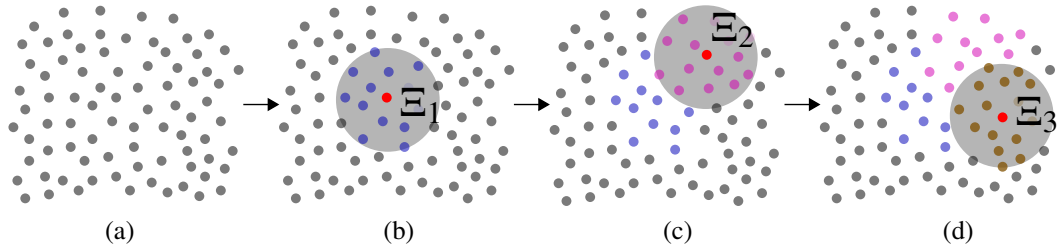

Figure 3.5: Overview of meshless computational scheme. From a set of points (a) local subsets (stencils) Ξ_i $i = \{1, 2, 3\}$ are selected as displayed in (b) to (c) to construct a meshless approximation.

direct approximations of the linear operator or explicitly constructing shape functions, according to the local point stencil. In contrast to univariate polynomial interpolation, where the polynomial space only depends on the number of used points and not on the chosen data-sites, multivariate approximation can only generate trial spaces which are data-depended (Mairhuber, 1956). Popular approximation techniques are least squares methods, especially moving least squares (Lancaster and Šalkauskas, 1981) and its variants, or kernel fitting techniques based on either radial basis functions (Franke and Schaback, 1998) or translates of kernel functions. The basis of all these underlying multivariate approximation or interpolation methods is the problem to reconstruct a d-dimensional unknown function $f : \Omega \subset \mathbb{R}^d \to \mathbb{R}$ from a discrete set of known values $(\mathbf{x}_i, f(\mathbf{x}_i)) \in \mathbb{R}^d \times \mathbb{R}$ for $i = 1, \ldots, N$. The numerical task is to find a function $\mathcal{P}_f : \Omega \subset \mathbb{R}^d \to \mathbb{R}$ which approximates function values such that $\mathcal{P}_f(\mathbf{x}_i) \approx f(\mathbf{x}_i)$ for all $i = 1, \ldots, N$. If an exact reproduction of the values is needed i.e. $\mathcal{P}_f(\mathbf{x}_i) = f(\mathbf{x}_i)$, then the underlying scheme is an interpolation. Independent of the chosen method, the recovery of unknown functions from data samples can be written as a linear combination of some coefficients c with corresponding known function values from a local stencil

$$\mathcal{P}_f(\mathbf{x}_i) \approx \sum_{j=1}^{n} c_j(\mathbf{x}_i) f(\mathbf{x}_j). \tag{3.1}$$

This local recovery scheme will be later generalized to the approximation of linear functionals from function values at the points.

These approximation schemes, especially the moving least squares technique, have their origin in surface generation. In a seminal paper by Lancaster and Šalkauskas (1981), the moving least squares technique was used to generate surfaces from scattered data and to generalize the metric interpolation technique of Shepard (1968). A first error analysis was given by Farwig (1986, 1991) and an approach using a different basis functions is

mentioned in Šalkauskas (1992).

First applications for solving partial differential equations were presented in the work of Nayroles et al. (1992) and Belytschko et al. (1994). Since then, the moving least squares technique has been established as a robust basis of many meshless applications in engineering an applied science. It is worth mentioning that a particular link to geophysical applications exists. The Backus-Gilbert inverse theory (Backus and Gilbert, 1968, 1970) is strongly related to moving least squares methods, as pointed out by Bos and Šalkauskas (1989) and both of them can be derived from each other. This is also true for a variant of Shepard's method (Abramovici, 2011).

While the classical theory of moving least squares addresses the case of function approximation, a first step towards a general scheme was done by Levin (1998). There, a moving least squares theory introduced to approximate bounded linear functionals from a normed function space. Later on, this theory was applied to Dirac's point evaluation functionals to approximate functions from a given data-set. In a following publication by Levin (1999), the author also applied this technique to produce multidimensional integration rules from scattered data. This scheme was also used for derivative recovery by Nayroles et al. (1992) as a *diffuse derivative* method. Later on, in the work of Mirzaei et al. (2012) this generalized approximation scheme was analysed, and for the recovery of derivatives the authors proved optimal rates of convergence towards true derivatives. The aim of their work was to simplify calculations in the Meshless Local Petrov-Galerkin (MLPG) method of Atluri and Zhu (1998). This weak-form based scheme utilizes a huge amount of integrals which have to be calculated. By using a generalized moving least squares scheme this effort can almost be avoided. Introducing successive an advanced Direct Meshless Local Petrov-Galerkin (DMLPG) method by Mirzaei and Schaback (2013) yields to varieties of new advanced meshless methods, using the generalized moving least squares approximation (Salehi and Dehghan, 2013; Taleei and Dehghan, 2014a; Mirzaei and Schaback, 2014; Ramezani et al., 2015; Mirzaei, 2015b; Mirzaei and Hasanpour, 2016).

Recently, the work of Trask et al. (2017) generalize staggered finite difference methods to the meshless case. The work is inspired by mimetic discretizations (Arnold et al., 2007), which mimic fundamental properties of the continuum partial differential equations. On this basis, a meshless local primal-dual grid complex with a virtual dual grid is used to chain a topological gradient operator locally on the primal complex with an approximation of the divergence on the dual grid by a generalized moving least squares method. Nevertheless, no real grid is used here, but a definition of virtual edges and faces generated from the local point stencils is used in the meshless discretization. Fortunately,

this kind of meshless discretization is capable to handle problems with discontinuous coefficients well. Therefore, it will be used in this thesis for extending the generalized moving least squares technique.

This chapter is organized as follows. First, the generalized moving least squares technique is derived and will be presented in Sub-chapter 3.2. This presentation also includes theoretical error estimates and the extension to the staggered moving least squares. These techniques are fundamental for all meshless calculations presented in this thesis. Then, a direct discretization scheme is given in Sub-chapter 3.3 to make use of these meshless techniques and provide a formulation to convert the discretization into a linear algebra problem. After presenting the meshless scheme, computational aspects will be illustrated in Sub-chapter 3.7. Here, the focus is placed on how suitable point sets could be generated and how computations can be done in parallel to speed up calculations. The chapter will close with several selected example calculations in Sub-chapter 3.8, a conclusion and a summary in Sub-chapter 3.9.

3.2 Generalized moving least squares

This subsection provides the basis for the following developments in constructing approximations for the boundary value problems discussed in Chapter 2.3. Since a more rigorous mathematical descriptive explanation is needed, this section follows the work of Levin (1998), Mirzaei et al. (2012) and Mirzaei and Schaback (2013).

Let $V \subseteq C^k(\Omega)$ be a function space, for functions that have continuous first $k \geq 0$ derivatives and let $u \in V$. The domain Ω is defined as before, with $\Omega \subseteq \mathbb{R}^d$ where d defines the dimensionality of the domain. Also, let $\{L_i(u)\}_{i=1}^n$ be a set of continuous, bounded, linear functionals from V^*, the dual space of V. The generalization of (3.1) is to find an approximation of a linear target functional $L(u) \in V^*$, utilizing the function u, with the help of a finite functional data set $\{L_i(u)\}_{i=1}^n$. Since a linear approximation is sought after, this process can be written as

$$L(u) \approx \widehat{L(u)} = \sum_{i=1}^{n} a_i(L) L_i(u). \tag{3.2}$$

The coefficients are linear in L and to calculate the coefficient vector $\mathbf{a} = (a_1, a_2, \ldots, a_N)^T$, one has to minimize the quadratic form

$$\frac{1}{2}\sum_{i=1}^{n}\frac{a_i^2(L)}{w(L, L_i)}, \tag{3.3}$$

subject to the linear constraints

$$\sum_{i=1}^{n} a_i(L)\, L_i(p) = L(p), \ \forall p \in \mathcal{P}. \tag{3.4}$$

Here, we assume that $\mathcal{P}_m(\mathbb{R}^d) = span\{p_1, p_2, \ldots, p_Q\}$ is the space of d-variate polynomials of absolute degree at most m and $Q = dim(\mathcal{P}) = \binom{m+d}{d}$. From Equation (3.4) follows that the approximation (3.2) is exact for the finite dimensional subspace $\mathcal{P} \subset V$. In (3.3) a non-negative weight function $w(L, L_i) > 0$, if $L_i \neq L$ is used which forms the stencil $\Xi := \left\{ j \in \{1, \ldots, n\} : w(L, L_j) > 0 \right\}$. Constructing a quadratic matrix $\mathbf{W} = diag\left(1/w(L, L_i)\right)_{(i\in\Xi)} \in \mathbb{R}^{n\times n}$, allows rewriting Equation (3.3) to

$$\frac{1}{2}\mathbf{a}^T\mathbf{W}\mathbf{a}. \tag{3.5}$$

Additionally, the linear constraints (3.4) can be recast into a matrix equivalent formulation using $\mathbf{P} = (L_i(p_m))_{(i\in\Xi,\ m=1,\ldots,Q)} \in \mathbb{R}^{n\times Q}$ and $\mathbf{L}_p = (L(p_1), \ldots, L(p_Q))^T \in \mathbb{R}^Q$

$$\mathbf{P}\mathbf{a} = \mathbf{L}_p. \tag{3.6}$$

Now, using Lagrange parameters $\boldsymbol{\delta} \in \mathbb{R}^Q$ and the constraints (3.6) gives

$$\frac{1}{2}\mathbf{a}^T\mathbf{W}\mathbf{a} - \boldsymbol{\delta}^T\left(\mathbf{P}^T\mathbf{a} - \mathbf{L}_p\right). \tag{3.7}$$

By differentiating (3.7) with respect to $\mathbf{a}$ and $\boldsymbol{\delta}$, the following system can be derived

$$\begin{pmatrix} \mathbf{W} & -\mathbf{P}^T \\ \mathbf{P} & \mathbf{0} \end{pmatrix}\begin{pmatrix} \mathbf{a} \\ \boldsymbol{\delta} \end{pmatrix} = \begin{pmatrix} \mathbf{0} \\ \mathbf{L}_p \end{pmatrix}. \tag{3.8}$$

This gives the solution for the coefficients

$$\mathbf{a}(L) = \mathbf{W}\mathbf{P}(\mathbf{P}^T\mathbf{W}\mathbf{P})^{-1}\mathbf{L}_p, \tag{3.9}$$

and allows to write the approximation (3.2) as

$$\begin{aligned} L(u) \approx \widehat{L(u)} &= \sum_{i=1}^{n} a_i(L) L_i(u) \\ &= \mathbf{L}(u)^T \mathbf{a}(L) \\ &= \mathbf{L}(u)^T \mathbf{W}\mathbf{P}(\mathbf{P}^T\mathbf{W}\mathbf{P})^{-1}\mathbf{L}_p \\ &= \mathbf{b}(L)^T \mathbf{L}_p. \end{aligned} \tag{3.10}$$

In Equation (3.10) it is evident, that the approximation of $L(u)$ can be done by a linear combination of the sample functionals $\{L_i(u)\}_{i=1}^n$ and the calculated coefficients $\mathbf{a}(L)$ or a linear combination of the target functionals evaluated at the basis and some basis functions $\mathbf{b}(L)$.
Similar, a solution to the approximation (3.2) can also be obtained, by a weighted least squares problem of finding one $p^* = \mathbf{b}(L)^T\mathbf{p} \in \mathcal{P}$ that is the solution of

$$min \left\{ \sum_{i=1}^{n} \left(L_i(u) - L_i(p)\right)^2 w_i \ : \ p \in \mathcal{P} \right\}. \tag{3.11}$$

It follows, that the two methods are connected through

$$L(u) \approx \widehat{L(u)} = L(p^*) = \sum_{i=1}^{n} a_i(L) L_i(u). \tag{3.12}$$

It can be shown (Mirzaei et al., 2012) that the weighted least squares problem (3.11) for identifying p^* is equivalent to finding the best weighted least-squares polynomial fit to the function values. This is done, by choosing the Dirac point evaluation functional

$$\delta_{\mathbf{x}} : u \mapsto u(\mathbf{x}), \tag{3.13}$$

for the target functional $L_x(u) := \delta_{\mathbf{x}} u = u(\mathbf{x})$ for a fixed $\mathbf{x} \in \Omega$. The functional data set is now $\{\delta_{\mathbf{x}_i} u\}_{i=1}^n = \{u(\mathbf{x}_i)\}_{i=1}^n$, the function u evaluated at a finite set of points $\{\mathbf{x}_i\}_{i=1}^n$. Also the weight function should be of the form $w(\mathbf{x}, \mathbf{x}_i) : \Omega \times \Omega \to \mathbb{R}$ and localized in a sense that w vanishes for arguments $\|\mathbf{x} - \mathbf{x}_i\|_2$ greater than a predefined threshold. Thus, p^* is the solution of

$$min \left\{ \sum_{i=1}^{n} \left(u(\mathbf{x}_i) - p(\mathbf{x}_i)\right)^2 w(\mathbf{x}, \mathbf{x}_i) \ : \ p \in \mathcal{P} \right\}, \tag{3.14}$$

where

$$p^*(\mathbf{x}) = \mathbf{b}(\mathbf{x})^T \mathbf{L}_p(\delta_\mathbf{x}) = \sum_{j=1}^{Q} b_j(\mathbf{x}) p_j(\mathbf{x}). \tag{3.15}$$

The coefficients can similarly be determined with the method above, to form the normal Equation (3.9). Mirzaei et al. (2012) came to the conclusion that the coefficients in (3.15) depend on the weights and index set on $\mathbf{x}$, but not on the functionals L. This allows to construct the approximation of $L(u)$ in (3.2) with

$$L(u(\mathbf{x})) \approx \widehat{L(u(\mathbf{x}))} = L(p^*) = \sum_{j=1}^{Q} b_j(\mathbf{x}) L(p_j) = \sum_{i=1}^{n} a_{i,L}(\mathbf{x})\, u(\mathbf{x}_i). \tag{3.16}$$

Nevertheless, the approximation (3.16) depends on $\mathbf{x}$ through the dependency of $b(\mathbf{x})$. If different functionals should be approximated by the same data, the coefficient vector $b(\mathbf{x})$ has to be computed only once. This is different for the coefficients $a(L)$ in the approximation (3.2). Here, a depends on the functional and must be recomputed every time when the target functional changes. In the presentation so far, some important aspects have been omitted due to the readability. To ensure that the problem (3.14) is uniquely determinable, the point set needs to be $\mathcal{P}$-unisolvent.

Definition 3.1 *The point set $\{\mathbf{x}_i\}_{i=1}^N \subseteq \mathbb{R}^d$ with $N \geq Q = \dim \mathcal{P}$ is called $\mathcal{P}$-unisolvent if the zero polynomial is the only polynomial from $\mathcal{P}$ that vanishes on all of them (Wendland, 2010).*

This also has to be valid for the generalization to linear functionals (Wendland, 2010). Obviously, the matrix term $\mathbf{PWP}^T$, which is often called '*moment matrix*', needs to be positive definite, to ensure a unique solution of the minimization problem (3.3-3.4) (Peypouquet, 2015). If the point set is $\mathcal{P}$-unisolvent, the matrix $\mathbf{P}$ in Equation (3.6) has full rank and $\mathbf{PWP}^T$ is positive definite (Salehi and Dehghan, 2013).

With this formulation, it is possible to approximate different linear target functionals acting on u using the data-set $\{u(\mathbf{x}_i)\}_{i=1}^n$. For the application to partial differential equations, two different target functionals are important. First, the approximation of derivatives of u

$$L(u) := \delta_\mathbf{x} \circ D^\alpha(u), \tag{3.17}$$

of the order $|\alpha|$ is possible with

$$\widehat{D^\alpha u(\mathbf{x})} = \sum_{j=1}^{Q} b_j(\mathbf{x}) D^\alpha p_j(\mathbf{x}) = \sum_{i=1}^{n} a_{i,\alpha}(\mathbf{x})\, u(\mathbf{x}_i). \tag{3.18}$$

In Equation (3.18) the coefficients $\tilde{a}_{i,\alpha}$ are calculated by the GMLS-approximation using $L := \delta_{\mathbf{x}} D^\alpha$. This type of approximation can be used in the collocation formulation of the boundary value problem. The second functional used in the weak formulations is

$$L(u) := \int_B v\,(\mathbf{x})\, \mathcal{L}u(\mathbf{x})\, d\mathbf{x}. \tag{3.19}$$

Here, $B = B(\mathbf{x}, r_0)$ or $\partial B(\mathbf{x}, r_0) \subset \mathbb{R}^d$ is the sphere (in three dimensions) or the circle (in two dimension) at a point $\mathbf{x}$ with radius r_0. Furthermore $\mathcal{L}$ is a linear differential operator and v is a compactly supported test function. Calculating coefficients using the GMLS method, the functional (3.19) can be easily approximated.

3.2.1 The GMLS divergence operator

Here, a summary of the generalized moving least squares divergence operator is given based on the work of Trask et al. (2017). The foundation of this operator is the geometric local structure of the meshless stencil as displayed in Figure 3.6. By defining a local

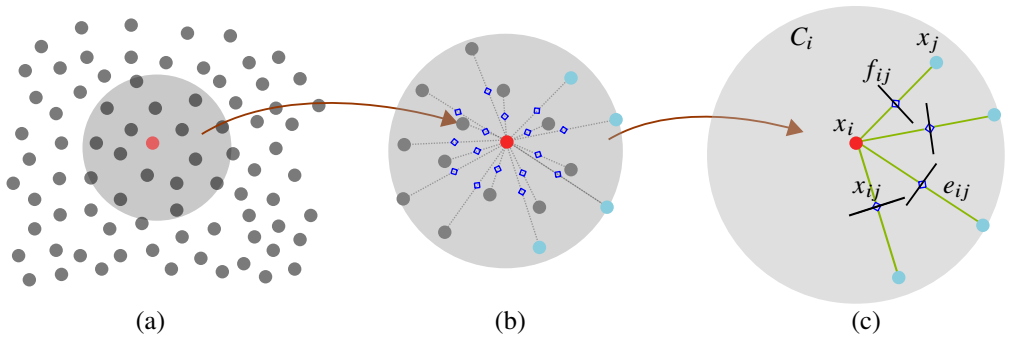

Figure 3.6: Stencil-wise construction of a local primal-dual grid complex. (a) Selecting enough points to form a stencil in a predefined neighbourhood. (b) Definition of midpoints (blue diamonds) from the central point to all other points. (c) Definition of the primal edges e_{ij} and dual faces f_{ij} inside a dual cell C_i from the definition of midpoints x_{ij}.

meshless stencil for points inside a predefined area $\Xi_i := \{\mathbf{x}_i \in \Omega \mid ||\mathbf{x}_i - \mathbf{x}_j||_2 < h\}$, a set of local vertex and edge points can be specified:

$$V_i := \{\mathbf{v}_i = \mathbf{x}_i \mid \mathbf{x}_i \in \Xi_i\}, \quad E_i := \{\mathbf{e}_{ij} = \mathbf{x}_i - \mathbf{x}_j \mid \mathbf{x}_i \in \Xi_i\}. \tag{3.20}$$

Using these definitions, a variety of approximation spaces can be derived to define a proper divergence operator. The edges defined in E_i have tangent vectors which can be derived by $\mathbf{t}_{ij} = (\mathbf{x}_i - \mathbf{x}_j)/||\mathbf{e}_{ij}||_2$. A local vertex and edge space can be derived as

$$V_i := \{u_i \in \mathbb{R} \mid \forall \mathbf{v}_i \in V_i\}, \quad E_i := \{u_{ij} \in \mathbb{R} \mid \forall \mathbf{e}_i \in E_i\}. \tag{3.21}$$

Dual to these two spaces, a cell (or stencil) space $C_i := \{u_i \in \mathbb{R}\}$ can be defined, which contains the function value at the stencil midpoint $\mathbf{x}_i$. As well as a dual face space

$$F_i := \{u_{ij} \in \mathbb{R} \mid \forall \mathbf{f}_{ij} \in F_i\}. \tag{3.22}$$

The face space and the edge space are isomorphic to each other. Because of this, the function values defined by the edge space $u_{ij} = \mathbf{u}_{ij} \cdot \mathbf{t}_{ij}$ can be written as values from the face space $u_{ij} = \mathbf{u}_{ij} \cdot \mathbf{n}_{ij}$ since tangential vectors $\mathbf{t}_{ij}$ on edges coincidence with normal vectors $\mathbf{n}_{ij}$ on faces.
Using the previous definitions of the stencil spaces the following gradient and divergence operators should be defined as

$$\nabla_i : V_i \to E_i, \quad \text{and} \quad \nabla_i \cdot : F_i \to C_i. \tag{3.23}$$

The key ingredient, presented in Trask et al. (2017), is to define a topological gradient operator by

$$\nabla_i(u) = \mathbf{u} \in E_i \quad \Leftrightarrow \quad u_{ij} = u_i - u_j \in V_i, \tag{3.24}$$

which can be "chained" with a divergence oprator $\nabla\cdot$. To define a divergence operator which utilizes the generalized moving least squares approximation the following Lemma proved in Trask et al. (2017) is necessary:

Lemma 3.1 *Let* $\mathbf{u} \in C^{k+1}(\Omega) \subseteq \mathbb{R}^d$ *and* $u_{i\to} \in C^{k+1}(\Omega) \subseteq \mathbb{R}$ *be the radial component function defined as* $u_{i\to}(\mathbf{x}_{ij}) = \mathbf{u}(x_{ij}) \cdot 2(\mathbf{x}_i - \mathbf{x}_j) = u_{ij}$*, then it holds*

$$\mathbf{u}(\mathbf{x}_i) = \frac{1}{2}\nabla_{i\to}(\mathbf{x}_i), \quad \textit{as well as} \quad \nabla \cdot \mathbf{u}(\mathbf{x}_i) = \frac{1}{4}\Delta_{i\to}(\mathbf{x}_i). \tag{3.25}$$

Now the task is to use the generalized moving least squares technique to approximate the gradient and divergence of the radial component function $u_{i\to}$. By defining a polynomial space $P^i := \{p \in \mathcal{P} \mid p(\mathbf{x}_i) = 0\}$, because $\mathbf{u}(\mathbf{x}_i) = 0$, and a finite functional data set

defined on the midpoint set M_i

$$\Lambda_i := \{\delta_{\mathbf{x}_{ij}} \circ u \mid \mathbf{x}_{ij} \in M_i\} \tag{3.26}$$

and furthermore a GMLS target functional

$$L_i(u) := \delta_{\mathbf{x}_i} \circ D^\alpha(u), \tag{3.27}$$

the following approximation can be done. First, solve the least-squares problem to calculate a $p^*(\mathbf{x}_i)$ which solves

$$min \left\{ \sum_{j=1}^{n} \left(\mathbf{u}(x_{ij}) \cdot 2(\mathbf{x}_{ij} - \mathbf{x}_j) - p(\mathbf{x}_{ij}) \right)^2 w(\mathbf{x}_i, \mathbf{x}_{ij}) \ : \ p \in P^i \right\}. \tag{3.28}$$

After solving the minimization problem, the calculated coefficients can be used to calculate the GMLS approximation:

$$\begin{aligned} \widehat{\mathbf{u}(\mathbf{x}_i)} &= \frac{1}{2}\widehat{\nabla} p^*(\mathbf{x}_i) = \frac{1}{2}\sum_{j}^{Q} b_j(\mathbf{x}_i) \nabla p_k^*(\mathbf{x}_i), \\ \widehat{\nabla \cdot \mathbf{u}(\mathbf{x}_i)} &= \frac{1}{4}\widehat{\Delta} p^*(\mathbf{x}_i) = \frac{1}{4}\sum_{j}^{Q} b_j(\mathbf{x}_i) \Delta p_k^*(\mathbf{x}_i). \end{aligned} \tag{3.29}$$

This forms the basis of approximating vector fields and their divergence in the framework of generalized moving least squares approximations. In Trask et al. (2016) the authors used this technique for the solution of the Stokes problem with application to suspension flows. In this thesis, it will be used for the discretization of the three- and two-dimensional magnetotelluric problem.

3.2.2 Error estimates

In order to determine the behavior of an approximation, theoretical results about the error should be given to serve as a basis for further investigations. Here, the error estimates are cited mainly from (Wendland, 2010; Mirzaei et al., 2012; Mirzaei, 2016; Trask et al., 2017). They are given for the generalized functional approximation. The task is to bound the approximation error in terms of a characteristic constant, which is linked to the organization of the used point set. A natural choice, frequently used in meshless methods, is the *fill distance* $h_{X,\Omega}$ for a specific point set X which covers the domain Ω

(Wendland, 2010; Fasshauer, 2007):

$$h_{X,\Omega} = \sup_{\mathbf{x}\in\Omega} \min_{\mathbf{x}_i\in X} \|\mathbf{x} - \mathbf{x}_i\|_2 \,. \tag{3.30}$$

This distance is a value for the maximal diameter of a sphere in Ω which includes no points. A point set is said to be *quasi-uniform* if there is a constant θ, which bounds the fill distance

$$\|\mathbf{x} - \mathbf{x}_i\|_2 \leq 2h_{X,\Omega} \leq \theta\|\mathbf{x} - \mathbf{x}_i\|_2 \,. \tag{3.31}$$

The main requirement to build approximations as (3.1) or (3.2) is the ability of the method to provide a local polynomial reproduction. If the approximation is able to do so, error estimates can be given, which are bounded by the fill distance (3.30) (Wendland, 2001). Formally, in the context of a GMLS approximation, some basis functions $a_i(L)$ provide a stable local polynomial reproduction, if

(a) $L(u) \approx \widehat{L(u)} := \sum_{i=1}^{n} a_i(L)L_i(u), \quad \forall u \in \mathcal{P},$

(b) $\sum_{i=1}^{n} |a_i(L)| \leq C_1, \quad \forall L \in V^*,$

(c) $a_i(L) = 0$ if $w(L, L_i) = 0.$

Here, these functions should be able to reproduce polynomials exactly from $\mathcal{P}$ (a), be bounded up to a constant C_1 (b) and should have a compact support defined by the weighting function (c). For the approximation of derivatives, Mirzaei et al. (2012) gives adapted properties for a stable polynomial reproduction, while Wendland (2001) defines properties for plain function approximation.
Various error estimates for moving least squares approximations were derived by several authors e.g. (Armentano, 2001; Wendland, 2001; Zuppa, 2003; Ren et al., 2014), some results for the generalized approximation scheme are given by Mirzaei (2016). Here, important is the:

Theorem 3.1 *(Mirzaei, 2016) Suppose that $\Omega \subset \mathbb{R}^d$ is a bounded domain with a Lipschitz boundary. Fix $m \in \mathbb{N}$, $p \geq 1$ and $q \geq 1$ and let $u \in W_p^{k+1}$. For α with $|\alpha| \leq m$, assume $m + 1 > |\alpha| + d/p$ for $p > 1$ and $m + 1 \geq |\alpha| + d$ for $p = 1$. If there are some constants C and h as defined in (Mirzaei, 2016, Theorem 3.6), such that for all points in X with $h_{X,\Omega} \leq h_0$, which are quasi-uniform with the same θ as in (3.31) it follows that*

$$\left\| D^\alpha u - \widehat{D^\alpha u} \right\|_{L^q(\Omega)} \leq C h_{X,\Omega}^{m+1-|\alpha|-d(1/p-1/q)_+} \|u\|_{W_p^{k+1}(\Omega)} \,, \tag{3.32}$$

while

$$\widehat{D^{\alpha}u}(\mathbf{x}) = \sum_{i=1}^{n} a_{i,\alpha}(\mathbf{x})\, u(\mathbf{x}_i) \tag{3.33}$$

is the GMLS derivative approximation of order α *and* $(1/p-1/q)_+ = max\{(1/p-1/q), 0\}$.

The Theorem 3.1 defines error bounds for GMLS derivatives through Equation (3.32) in dependence of the fill-distance $h_{X,\Omega}$. Mirzaei (2016) also provides error bounds for functionals (similar to 3.19), which are used in weak formulations like MLPG and DMLPG:

Theorem 3.2 *(Mirzaei, 2016) Suppose that all conditions of Theorem 3.1 are satisfied. If there are some constants C and h as defined in (Mirzaei, 2016, Theorem 3.6), such that for all points in X with* $h_{X,\Omega} \leq h_0$*, which are quasi-uniform with the same* θ *as in (3.31) it follows that*

$$\left\| L(u) - \widehat{L(u)} \right\|_{L^q(\Omega)} \leq C h_{X,\Omega}^{m+1-l-d(1/p-1/q)_+} \|u\|_{W_p^{k+1}(\Omega)} . \tag{3.34}$$

With an approximation defined as

$$\widehat{L(u)}(\mathbf{x}) = \sum_{i=1}^{n} a_{i,L}(\mathbf{x})\, u(\mathbf{x}_i), \tag{3.35}$$

which is a GMLS derivative approximation of $\widehat{L(u)}(\mathbf{x}) = 1/vol(B) \int_B v\,(\mathbf{x}-\mathbf{y})\, \mathcal{L}u(\mathbf{y})\, d\mathbf{y}$ *and l is the maximal order of the involved linear operator* $\mathcal{L}$*. The constant n is determined such that* $L(\mathbf{x}^{\alpha}) \neq 0$ *for some* α *with* $|\alpha| \leq k$ *and* $L(\mathbf{x}^{\alpha}) = 0$ *for all* α *with* $|\alpha| > k$.

Both Theorems 3.1 and 3.2 provide estimates for the approximation order, when using the generalized moving least squares scheme. It is obvious that the error is affected either by the order of the derivatives α and by the polynomial degree m. Using a weak formulation deploying functionals, which use integrals, the approximation order is influenced by the order of the linear operator $\mathcal{L}$. By using weak formulations the order of the involved linear operator is usually reduced by one degree in contrast to an equivalent strong formulation. By using the staggered approximation scheme, presented in the previous chapter, similar error estimates can be derived. By inspecting the approximation of $\mathbf{u}(\mathbf{x})$ and $\nabla \cdot \mathbf{u}(\mathbf{x})$ in Equation (3.29), two differential operators are involved. Thus, point-wise error estimates are given by Trask et al. (2017):

$$\left\| \mathbf{u}(\mathbf{x}_i) - \widehat{\mathbf{u}(\mathbf{x}_i)} \right\| \leq C h_{X,\Omega}^{m} \|u\|_{C^{k+1}(\Omega)} \tag{3.36}$$

and

$$\left\| \nabla \cdot \mathbf{u}(\mathbf{x}_i) - \widehat{\nabla \cdot \mathbf{u}(\mathbf{x}_i)} \right\| \leq C h_{X,\Omega}^{m-1} \|u\|_{C^{k+1}(\Omega)} \,. \tag{3.37}$$

The preconditions for these error bounds are comparable to the ones presented before. By comparing the order of the approximation, both schemes are equal. Special for the presented schemes is that the convergence rate cannot be increased, when going from $m = 2k$ to $m = 2k + 1, k \geq 1$. Here the contribution of odd powers from the polynomials are missed, as Mirzaei (2016) explains.

3.3 Discretizations

To derive a set of linear equations obtained from the formulation of Maxwell's equations, a variety of methods are available. Having derived a correct mathematical abstraction in form of the boundary value problem, as described in chapter 2.3, the next step is to make use of the generalized moving least squares technique. In order to proceed, the boundary value problem has to be reformulated for the discretization. This thesis represents a further development of the work presented in Wittke and Tezkan (2014), some formulations from this publication will be reused and serve as starting point for later developments in this thesis. All the formulations presented here, will make use of two schemes for the discretization of Maxwell's equations. First, a meshless Petrov-Galerkin (MLPG) scheme will be used as in Wittke and Tezkan (2014) to reformulate the boundary value problems and in a second step the generalized moving least squares technique will be deployed. By using such approximation techniques, a direct discretization as presented by Mirzaei and Schaback (2013) or Schaback (2013) can be utilized to produce an algebraic system of equations. The staggered approximation scheme will be used in a strong formulation. Here, the previously introduced boundary value problem can be directly transformed into an algebraic system of equations by approximating the differential operators.
Generally, the well-known discretization framework of the finite elements can be converted to a meshless setting. The idea of using trial and shape functions to construct the solution of a linear operator equation from a finite-dimensional function space V_h , where trial functions are generated by some specifically chosen shape functions, is not restricted by using a mesh. Shape functions can be calculated for some scattered points by using moving least squares techniques, translates of kernels or radial basis functions. For

example, a linear, partial differential system of equations is

$$\begin{aligned} \mathcal{L}u &= f \quad \text{in } \Omega, \\ \mathcal{B}u &= g \quad \text{on } \partial\Omega, \end{aligned} \tag{3.38}$$

utilizing a linear differential operator [5] $\mathcal{L} : V \to F$ and a boundary operator $\mathcal{B} : V \to F$ on some normed linear function space V. Also, $\{f, g\} \in F$ and $u \in V$ and the task is to find an approximation of $\hat{u} \in V_h$, for which meshless methods should generate the finite dimensional subspace $V_h \subset V$. This operator equation can be rewritten as a set of N linear functionals $\{L_i\}_{i=1}^N \in V^*$, which form the system

$$L_i(u) = f_i \ \in \mathbb{R}, \ \ 1 \leq i \leq N. \tag{3.39}$$

Here $N = |X|$ is the cardinality of the used point set. If a functional corresponds to a boundary operator, suitable values of g_i should be used instead of f_i (Schaback and Wendland, 1999). If a GMLS approximation is used to recover the linear functionals,

$$L(u) \approx \widehat{L(u)} = \sum_{i=1}^{n} a_i(L)u(x_i), \tag{3.40}$$

an algebraic system in the form of

$$\boldsymbol{A}\mathbf{u} = \mathbf{f} \tag{3.41}$$

can be written (Schaback, 2017), with components defined as

$$\begin{aligned} \boldsymbol{A} &= (a_i(L_j))_{1\leq i\leq N, 1\leq j\leq N} \in \mathbb{R}^{N\times N}, \\ \mathbf{u} &= (u(x_1), \ldots, u(x_N))^T \in \mathbb{R}^N, \\ \mathbf{f} &= (f_1, \ldots, f_N)^T \in \mathbb{R}^N. \end{aligned} \tag{3.42}$$

Now, two main options are possible to set-up the system matrix $\mathbf{A}$. The first one based on using meshless *shape* functions and the second method directly approximates the set of linear functionals used in the system (3.39). Both approximations can always be written as Equation (3.40) (Schaback and Wendland, 1999), but if using shape functions generated by a meshless method, the functionals (3.40) must act on them. As avowed in the previous section, the generation of suitable meshless approximation spaces heavily involves linear algebra and no closed form expressions are available. This is unfavorable if the functionals define derivatives or integration. In the case of integration, mostly

[5] For example a linear differential operator of the order k like $\mathcal{L} = \sum_{|\alpha|\leq k} a_\alpha D^\alpha$ so, $\mathcal{L} : C^k(\Omega) \to C(\Omega)$

Gaussian quadrature rules are used. This rules evaluate functions at selected Gauss points, which leads to an enormous amount of shape function evaluation and slows down the construction of the system matrix seriously. The main intention of direct methods developed in (Mirzaei et al., 2012; Mirzaei and Schaback, 2013, 2014) was to bypass these calculations, and it was also the main drawback of the method used in the work of Wittke and Tezkan (2014) compared to finite element formulations. This thesis adapts these newly developed direct methods and extends the work of Wittke and Tezkan (2014). Nevertheless, which path is chosen, a connection of the continuous partial differential system to a discrete counterpart, explicitly construct an approximation as Equation (3.40) can be done in several ways. Here, we use two schemes, which are commonly refereed in the literature as strong formulations and weak formulations (Sadiku, 2000).

3.4 Meshless formulations

Strong formulations, or often referred to as point collocation methods, are popular schemes for the meshless discretization of partial differential equations. A variety of several variants are available, using different approximation strategies. Most prominent are the Generalized Finite Differences (Seibold, 2006), the Finite Point Method (Oñate et al., 1996) or meshless collocation schemes (Franke and Schaback, 1998). Strong formulations do not weaken the partial differential formulation by integration over test functions and using identities from vector calculus. These formulations are simpler to use, but their convergence order are reduced in comparison to weak formulations. In this subsection the relevant implementations for the discretizations of Maxwell's equations are given. First, the three-dimensional formulations from chapter 2.3.1 are discretized and then subsequently the two-dimensional problem will be described.

3.4.1 Two-dimensional scalar field formulation

Compiling the strong formulation for a two-dimensional scalar field is more straightforward than using vector valued expressions. The basis are systems of partial differential equations for the TE- and TM-mode. Given in the chapter about second order formulations, the system used here is described through Equations (2.74) and (2.75). Both equations have the same characteristic structure and can be reformulated as a system of generic partial differential equations. To get a specific formulation, only a change in the coefficients is needed to get from one formulation to the other. Using Equations (2.74) and (2.75) and a generic place-holder $u \in \{E_x, H_x\}$ as well as the coefficients C^A and C^B, the simplified

system can be written as

$$\begin{aligned} \nabla \cdot \left(C^A(\mathbf{x}) \nabla u(\mathbf{x}) \right) + C^B(\mathbf{x}) u(\mathbf{x}) &= s(\mathbf{x}) \qquad \text{in } \Omega, \\ u(\mathbf{x}) &= u^{1D}(\mathbf{x}) \quad \text{on } \Gamma^D, \\ C^A(\mathbf{x}) \frac{\partial u}{\partial \mathbf{n}}(\mathbf{x}) &= g(\mathbf{x}) \qquad \text{on } \Gamma^N. \end{aligned} \tag{3.43}$$

Now, $\mathbf{x} \in \mathbb{R}^2$ and the point-set is $X = \{\mathbf{x}_i\}_{i=1,\dots,N}$ divided into $X = X_\Omega \cup X_d \cup X_n$, in which $X_\Omega \subset \Omega \subsetneq \mathbb{R}^2$ are points inside the domain Ω, while $X_D \subset \Gamma^D$ are points on a Dirichlet boundary and $X_N \subset \Gamma^N$ are points on a Neumann boundary. By comparing system (3.43) to (2.74) and (2.75), the coefficients for the TE-mode can be identified as $C^A(\mathbf{x}) = \mu_0^{-1}$ and $C^B(\mathbf{x}) = -i\omega\sigma(\mathbf{x})$. The TM-mode the coefficients are $C^A(\mathbf{x}) = \sigma(\mathbf{x})^{-1}$ and $C^B(\mathbf{x}) = -i\omega\mu_0$. A suitable set of functionals for interior points can be given as

$$L_i^\Omega(u) := \nabla \cdot \left(C^A(\mathbf{x}_i) \nabla u(\mathbf{x}_i) \right) + C^B(\mathbf{x}_i) u(\mathbf{x}_i), \quad \mathbf{x}_i \in X_\Omega \subset \Omega. \tag{3.44}$$

As in the vectorial case, presented before, the functional can be split into two parts and the correct coefficients for the selected mode has to be used. If functionals connecting the fields to boundary values are required, a suitable set is

$$L_j^D(u) := \delta_{\mathbf{x}_j} \circ u, \quad \mathbf{x}_j \in X_D \subset \Gamma^D, \tag{3.45a}$$

$$L_l^N(u) := C^A(\mathbf{x}_l) \frac{\partial u}{\partial \mathbf{n}}(\mathbf{x}_l), \quad \mathbf{x}_l \in X_N \subset \Gamma^N. \tag{3.45b}$$

Having all functionals defined, the whole formulation can be written as

$$L_i(u) = s(\mathbf{x}_i), \quad \forall \mathbf{x}_i \in \Omega \cup \Gamma^D \cup \Gamma^N, \tag{3.46}$$

where the index $i = 1, \dots, N$ contains all points from Ω including the boundary. Using the approximation of the functionals gives

$$\begin{aligned} L_i(u) &\approx \sum_{j=1}^{n} a_{ij}(L_i)\, u(\mathbf{x}_j) \\ &= s_i(\mathbf{x}_i), \quad \forall \mathbf{x}_i \in \Omega \cup \Gamma^D \cup \Gamma^N. \end{aligned} \tag{3.47}$$

Assembling all the coefficients into an algebraic system results in

$$\boldsymbol{A}\mathbf{u} = \mathbf{s}. \tag{3.48}$$

The complex-valued matrix $\boldsymbol{A} \in \mathbb{C}^{N\times N}$ should be constructed by the coefficients resulting from a GMLS expansion (3.47), while $u \in \{E_x, H_x\}$ is the vector for all field components at all N points, so for example in the TE-mode $\mathbf{u} = (E_x(\mathbf{x}_1), \ldots, E_x(\mathbf{x}_N))$. The right-hand side of Equation (3.43) is $\mathbf{s} \in \mathbb{C}^N$ including also all possible values for points at the boundary.

3.4.2 Three-dimensional potential field formulation

First, the simplified operator form notation (2.39) of the potential formulation will be used to identify the functionals used for the discretization

$$\begin{pmatrix} C_1 & 0 & 0 & P_x \\ 0 & C_2 & 0 & P_y \\ 0 & 0 & C_3 & P_z \\ P_x & P_y & P_z & D \end{pmatrix} \begin{pmatrix} A_x \\ A_y \\ A_z \\ \phi \end{pmatrix} = \begin{pmatrix} -\mu_0 J_x^e \\ -\mu_0 J_y^e \\ -\mu_0 J_z^e \\ \nabla \cdot \mathbf{J}^e \end{pmatrix}. \tag{3.49}$$

Using $\mathbf{x} \in \mathbb{R}^3$ and subdividing a point set $X = \{\mathbf{x}_i\}_{i=1,\ldots,N}$ into $X = X_\Omega \cup X_d \cup X_n$, in which $X_\Omega \subset \Omega \subsetneq \mathbb{R}^3$ are points inside the domain Ω, whereas $X_D \subset \Gamma^D$ are points on a Dirichlet boundary and $X_N \subset \Gamma^N$ are points on a Neumann boundary. As described in chapter 2.3.1 and summarized in Table 2.3, the diagonal coefficients for a Coulomb gauging are $C_{1,2,3} = \nabla^2 + i\omega\mu_0\hat{\sigma}(\mathbf{x})$ and $D = \nabla \cdot (\hat{\sigma}(\mathbf{x})\nabla)$. The off-diagonal coupling terms are the component wise representations of $P_i = \mu_0\hat{\sigma}(\mathbf{x})\partial_k$ with $k \in \{x, y, z\}$. This allows setting up functionals corresponding to interior points from the set X_Ω and the diagonal terms of (3.49) :

$$\left.\begin{aligned} L_i^{C_1}(A_x) &:= \nabla^2 A_x(\mathbf{x}_i) + i\omega\mu_0\hat{\sigma}(\mathbf{x}_i)A_x(\mathbf{x}_i) \\ L_i^{C_2}(A_y) &:= \nabla^2 A_y(\mathbf{x}_i) + i\omega\mu_0\hat{\sigma}(\mathbf{x}_i)A_y(\mathbf{x}_i) \\ L_i^{C_3}(A_z) &:= \nabla^2 A_z(\mathbf{x}_i) + i\omega\mu_0\hat{\sigma}(\mathbf{x}_i)A_z(\mathbf{x}_i) \\ L_i^{D}(\phi) &:= \nabla \cdot (\hat{\sigma}(\mathbf{x}_i)\nabla\phi(\mathbf{x}_i)) \end{aligned}\right\} \mathbf{x}_i \in X_\Omega \subset \Omega. \tag{3.50}$$

The diagonal terms C_1 to C_3 can also be decomposed into six different functionals. The off-diagonal coupling terms result in a set of functionals for the interior point set:

$$L_i^{P_l}(u) := \mu_0\hat{\sigma}(\mathbf{x}_i)\partial_k u(\mathbf{x}_i), \quad \mathbf{x}_i \in X_\Omega \subset \Omega. \tag{3.51}$$

The indices k in Equation (3.51) are used for the spatial direction $k \in \{x, y, z\}$ and $u \in \{A_x, A_y, A_z, \phi\}$. To complete the assembly of functionals, resulting from the description of the partial differential equations, a suitable set of functionals connecting

the fields to Dirichlet and Neumann boundary values should be established:

$$\begin{aligned} L_k^D(u) &:= \delta_{\mathbf{x}_j} \circ u, \quad \mathbf{x}_j \in X_D \subset \Gamma^D, \\ L_l^N(u) &:= \frac{\partial u}{\partial \mathbf{n}}(\mathbf{x}_l), \quad \mathbf{x}_l \in X_N \subset \Gamma^N. \end{aligned} \tag{3.52}$$

In Equations (3.52), the specific fields (A_x, A_y, A_z, ϕ) should be used instead of the generic place-holder u. Now, for every point inside the domain, a functional from Equations (3.50) through (3.52) can be used to set up a system of algebraic equations which, can be solved for the field values. Since this problem can be assembled from individual scalar functionals, the entire formulation requires a vector valued notation. The whole system, combining all functionals for all fields can be written as

$$L_i(\mathbf{u}) = \mathbf{s}_i(\mathbf{x}_i), \quad \forall \mathbf{x}_i \in \Omega \cup \Gamma^D \cup \Gamma^N. \tag{3.53}$$

Here, $d \in \{1, 2, 3\}$ describes the dimensionality, $\mathbf{s}_i^{(d)}(\mathbf{x}_i)$ is the right-hand side of Equation (3.49) evaluated at a point $\mathbf{x}_i$ and $\hat{\mathbf{u}} = (\hat{A}_x, \hat{A}_y, \hat{A}_y, \hat{A}_y)^T$. To set-up the algebraic system in terms of coefficients gained from an expansion of the functionals, the left-hand side of Equation (3.53) must be expanded as:

$$\begin{aligned} L_i(\mathbf{u}) &\approx \sum_{j=1}^{n} \mathbf{A}_{ij}\mathbf{u}(\mathbf{x}_j) \\ &= \sum_{j=1}^{N} \begin{pmatrix} a_{ij}^{(11)} & a_{ij}^{(12)} & a_{ij}^{(13)} & a_{ij}^{(14)} \\ a_{ij}^{(21)} & a_{ij}^{(22)} & a_{ij}^{(23)} & a_{ij}^{(24)} \\ a_{ij}^{(31)} & a_{ij}^{(32)} & a_{ij}^{(33)} & a_{ij}^{(34)} \\ a_{ij}^{(41)} & a_{ij}^{(42)} & a_{ij}^{(43)} & a_{ij}^{(44)} \end{pmatrix} \begin{pmatrix} A_x(\mathbf{x}_j) \\ A_y(\mathbf{x}_j) \\ A_z(\mathbf{x}_j) \\ \phi(\mathbf{x}_j) \end{pmatrix} \\ &= \mathbf{s}_i(\mathbf{x}_i), \quad \forall \mathbf{x}_i \in \Omega \cup \Gamma^D \cup \Gamma^N. \end{aligned} \tag{3.54}$$

As explained before, each functional must be approximated at each point i within its neighbourhood containing n points and by using Equation (3.49), the resulting algebraic system is complex-valued and can be constructed as

$$\boldsymbol{A}\mathbf{u} = \mathbf{s}. \tag{3.55}$$

Here, the matrix $\boldsymbol{A} \in \mathbb{C}^{4N \times 4N}$ is assembled block-wise by the coefficient matrices from expansion (3.54), while

$$\begin{aligned} \mathbf{u} = (&A_x(\mathbf{x}_1), A_y(\mathbf{x}_1), A_z(\mathbf{x}_1), \phi(\mathbf{x}_1), \\ &A_x(\mathbf{x}_2), A_y(\mathbf{x}_2), A_z(\mathbf{x}_2), \phi(\mathbf{x}_2), \\ &\ldots, A_x(\mathbf{x}_{4N}), A_y(\mathbf{x}_{4N}), A_z(\mathbf{x}_{4N}), \phi(\mathbf{x}_{4N}))^T, \quad \in \mathbb{C}^{4N} \end{aligned} \tag{3.56}$$

is the field vector for all field components at all $4N$ points and $\mathbf{s} \in \mathbb{C}^{4N}$ is the right-hand side of Equation (3.49) including possible values for points at the boundary. The generalized moving least squares approach should generate the coefficients used in the expansion (3.54). A detailed description, how to calculate these coefficients is given in chapter 3.5, which describes the specific implementation.

3.4.3 Weak formulation

Weak formulations of a boundary value problems are commonly used in Finite Element analysis. Here, the partial differential equation system is reformulated into an integral expression, where a bilinear form is connected to the integral of the source term multiplied by a test function. If the bilinear form is bounded and coercive, an unique solution can be found. A beneficial property of a weak formulation is the reduced order of partial derivatives. In a strong formulation, second order derivatives have to be used, whereas in a weak formulation one derivative is "transferred" to the test function. This lowers the requirement that the trial functions need to be continuously differentiable until at least second partial derivative.

In this thesis, a formulation by Wittke and Tezkan (2014) is used. While the context, a meshless formulation, is the same, the implementation differs. Here, a direct method is used to approximate the resulting integral formulations from the weak form instead of using meshless shape functions and quadrature rules. The derivation of the weak formulation will be geared to the well-known MLPG scheme of Atluri and Zhu (1998); Atluri et al. (1999); Atluri and Shen (2002). The general description of the boundary value problem (3.43) is transformed to a weak formulation using the weighted residual method. This is also a typical step in a finite element analysis. Therefore, the weighted (with a test function w), minimal residual of Equation (3.43) will be integrated over Ω

$$\int_{\Omega} \left[\nabla \cdot \left(C^A \nabla u \right) - C^B u - s \right] w \; d\Omega = 0. \tag{3.57}$$

Here, the generic place-holder u and the coefficients must be exchanged with the relevant fields and coefficients according to the actual magnetotelluric formulation. We finally derive the general weak form of Equation (3.43) by separating (3.57) into parts

$$\begin{aligned} \int_{\Gamma} \left[w C^A \frac{\partial u}{\partial n} \right] \, d\Gamma - \int_{\Omega} \left[C^A \nabla w \cdot \nabla u \right] \, d\Omega \\ - \int_{\Omega} w C^B u \, d\Omega = \int_{\Omega} w s \, d\Omega \ . \end{aligned} \tag{3.58}$$

A common vector identity $w\nabla \cdot (\alpha \nabla u) = \nabla \cdot (w\alpha \nabla u) - \nabla w \cdot (\alpha \nabla u)$ and the divergence theorem is used to derive the first integrals in Equation (3.58). Also, n is the unit normal outward to the boundary Γ. Now, the general weak statement of Equation (3.43) will be transformed to the MLPG formulation. Within the MLPG local sub-domains Ω_s are defined which can be equal to the support of the weight function Ω_{te} for one arbitrarily chosen point i. This definition is the main idea in the MLPG-fomulation. In a conventional Finite Element or Element-Free Galerkin method, the weak form of Equation (3.43) will be globally used all over the whole model domain. In a MLPG-formulation small sub-domains inside the global domain Ω are used. If the set of points $X = \{\mathbf{x}_1, \ldots, \mathbf{x}_N\}$

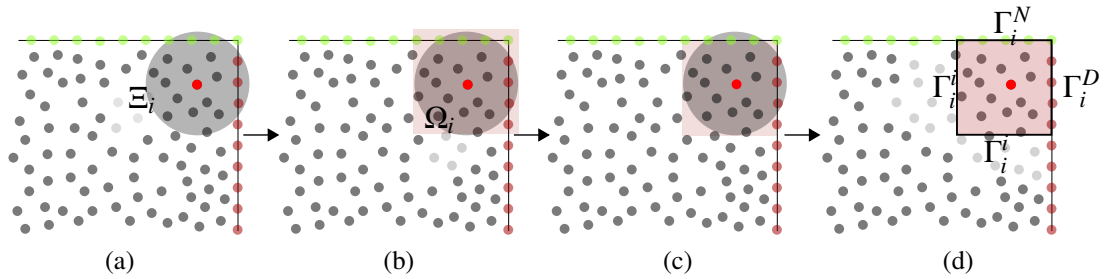

Figure 3.7: Overview of the MLPG integration domain generation construction. From a set of points (a) a local stencil Ξ_i is selected from the support of the weight function. In (b) the rectangular integration domain Ω_i is defined and clipped with the outer domain boundary (c). In (d) the outer boundaries of the integration domains are defined.

fills the model domain, patches of $\left\{\Omega_s^i\right\}_{i=1}^N$ sub-domains covers the whole model domain. Each point creates its own sub-domain and mentioned before, it is a Petrov-Galerkin formulation, so the approximation of the boundary value problem can be done with shape and weight functions from different function spaces. In Atluri et al. (1999) six different weight functions are examined which led to several MLPG schemes. Equation (3.58)

transforms to

$$\begin{aligned}&\int\limits_{\Gamma_s^i}\left[w_i C^A \frac{\partial u}{\partial n}\right]\, d\Gamma - \int\limits_{\Omega_s^i}\left[C^A \nabla w_i \cdot \nabla u\right]\, d\Omega - \int\limits_{\Omega_s^i} w_i C^B u\, d\Omega \\ &= \int\limits_{\Omega_s^i} w_i s\, d\Omega.\end{aligned} \tag{3.59}$$

The model boundary Γ (partly) includes all other boundaries $\left(\partial\Omega_s = \Gamma_s^i = \Gamma_i^i \cup \Gamma_i^D \cup \Gamma_i^N\right)$, thus

$$\begin{aligned}&\int\limits_{\Gamma_i^i \setminus \Gamma_i^N}\left[w_i C^A \frac{\partial u}{\partial n}\right]\, d\Gamma + \int\limits_{\Gamma_i^N}\left[w_i C^A \frac{\partial u}{\partial n}\right]\, d\Gamma \\ &- \int\limits_{\Omega_s^i}\left[C^A \nabla w_i \cdot \nabla u\right]\, d\Omega - \int\limits_{\Omega_s^i} w_i C^B u\, d\Omega = \int\limits_{\Omega_s^i} w_i s\, d\Omega\ .\end{aligned} \tag{3.60}$$

The index i identifies the actual test function point corresponding to the local sub-domain Ω_s^i. In the framework of MLPG a distinction is drawn between different weight functions due to the Petrov-Galerkin formulation. For the purpose of this thesis, a constant function $w_i(x) = 1$ is used. This simplifies the local weak formulation, because the first areal integration on the left hand side of Equation (3.60) vanishes and only the boundary integral remains. If the weight function is inserted into Equation (3.60), the final formulation reads

$$\int\limits_{\Gamma_i^i \setminus \Gamma_i^N} C^A \frac{\partial u}{\partial n}\, d\Gamma + \int\limits_{\Gamma_i^N} g\, d\Gamma - \int\limits_{\Omega_s^i} C^B u\, d\Omega = \int\limits_{\Omega_s^i} s\, d\Omega\ . \tag{3.61}$$

This is the MLPG-5 formulation proposed by Atluri and Zhu (1998) for the boundary value problem (3.43). The shape of local sub-domains can be arbitrarily chosen and for a two-dimensional problem rectangle shapes are used. By constructing these sub-domains, they are clipped against boundaries and the resulting polygon is used. Figure 3.7 illustrate the construction of sub-domains and/or integration domains. In opposite to the work of Wittke and Tezkan (2014), no approximation of u is constructed to use within the MLPG weak form (3.61). Instead, the direct GMLS approximation presented in the sub-chapter is used to directly approximate the integrals of (3.61), which was proposed by Mirzaei and Schaback (2013). Whichever MLPG formulation is chosen, a set of designated functionals can be defined to set up an algebraic system of equations. Starting from Equation (3.61), all integrals acting on u can be approximated by the GMLS formulation

using the functional set

$$\left.\begin{aligned} L_i^1(u) &:= \int_{\Gamma_s^i \setminus \Gamma_i^N} C^A \frac{\partial u}{\partial \mathbf{n}}(\mathbf{x}_i)\ d\Gamma \\ L_i^2(u) &:= -\int_{\Omega_s^i} C^B u(\mathbf{x}_i)\, d\Omega \end{aligned}\right\} \mathbf{x}_i \in X_\Omega \setminus \Gamma^N \subset \Omega. \tag{3.62}$$

While for the boundary functionals, the same procedure as using the collocation method can be used,

$$L_j^D(u) := \delta_{\mathbf{x}_j} \circ u, \quad \mathbf{x}_j \in X_D \subset \Gamma^D, \tag{3.63a}$$

$$L_l^N(u) := C^A(\mathbf{x}_l) \frac{\partial u}{\partial \mathbf{n}}(\mathbf{x}_l), \quad \mathbf{x}_l \in X_N \subset \Gamma^N. \tag{3.63b}$$

Having all functionals defined, the complete formulation can be written as

$$L_i(u) = S(\mathbf{x}_i), \quad \mathbf{x}_i \in X_\Omega \subset \Omega \cup \Gamma^D \cup \Gamma^N, \tag{3.64}$$

where the index $i = 1, \ldots, N$ selects every point from Ω including points on the boundary. Using the approximation of the functionals gives

$$\begin{aligned} L_i(u) &\approx \sum_{j=1}^{n} a_{ij}(L_i)\, u(\mathbf{x}_j) \\ &= s_i(\mathbf{x}_i), \quad \mathbf{x}_i \in X_\Omega \subset \Omega \cup \Gamma^D \cup \Gamma^N. \end{aligned} \tag{3.65}$$

Inspecting the weak formulation presented above, it is noticeable that it is possible to enforce the boundary conditions by using strong collocation. When using inhomogeneous boundary conditions or a formulation with a source term, the right-hand sides of Equations (3.43) need to be evaluated in terms of line and area integrals.
The MLPG formalism decreases the order of the partial derivatives of the first equation in (3.43) and in a second step with the specified constant weight function the first areal integral of Equation (3.60) vanishes.

3.5 Implementations

In the previous chapter the required functional formulations to set-up an algebraic system of equations have been presented. This step towards a fully discrete system was done without an explicit definition of the used coefficients and how they should be calculated. In this chapter the details for a feasible implementation will be presented.

First, a suitable basis should be defined and its properties will be discussed. Later on, a potential weight function will be given to complete the requirements for constructing the normal equations for the generalized moving least squares approximation. After defining a proper basis and weight function, it is possible to give explicitly the implementation for calculating the coefficients of the approximation.

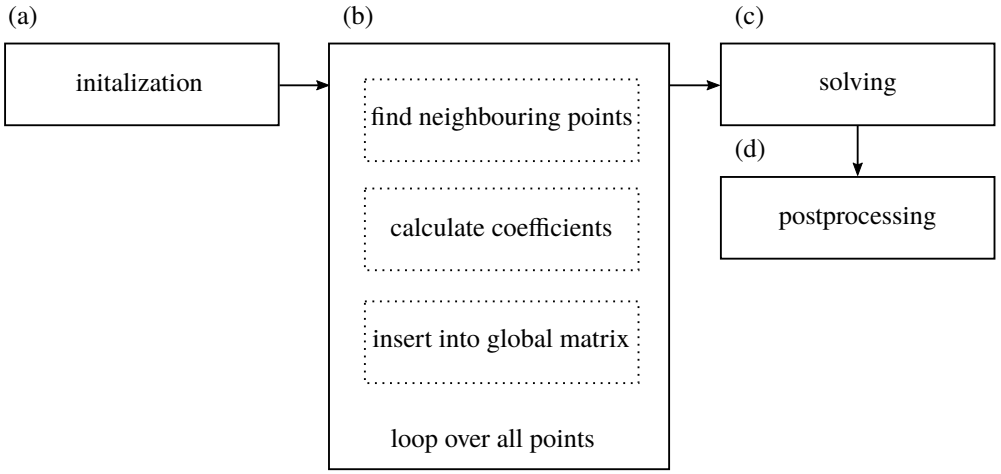

Figure 3.8: Overview of a meshless calculation scheme. After initializing the computational domain and generating the point cloud (a), for every point (b), its neighbouring points which forms a local stencil must be selected. From this stencil, the coefficients can be calculated and should be inserted into the global sparse matrix. After solving (c) the sparse matrix and post process the data (d) the results of the meshless simulations are ready.

3.5.1 General work flow

Now, it is possible to formulate a specific implementation for each of the earlier stated boundary value problems. To give a comprehensive overview, a flow chart is presented in Figure 3.8. Here, retrospect and in combination with Figure 3.5 the procedure of a meshless computational scheme can be seen. The general work flow is mostly the same for every meshless method (Dolbow and Belytschko, 1998), but varies in some specific points. After initializing the computational domain and generating the point cloud, for every point its neighbouring points, which forms a local stencil must be selected. From these stencils, the coefficients can be calculated and should be inserted into the global sparse matrix. After solving the sparse system of equations and post process the data, results of the meshless simulations can be used otherwise. The point cloud generation in the initialization will be discussed in a subsequent chapter as well as the stencil selection. For now, the actual implementation of part (b) as displayed in Figure 3.8 is for interest. After having defined a proper polynomial basis and a suitable weight function, the

computation of the coefficients will be described. Not all parts of the implementation will be described in detail, due to their similarity. Here, the focus lies in the implementation of the staggered generalized moving least squares approach for the two-dimensional magnetotelluric problem and an implementation of the three-dimensional potential formulation.

3.5.2 Polynomial basis

To solve the quadratic minimization problem (3.3) subject to the linear constrains (3.4) a suitable polynomial basis should be used. Inspecting Equation (3.15), the Generalized Moving Least Squares provides a polynomial from some polynomial space of d-variate polynomials of absolute degree at most m. A polynomial canonical basis, such that $\mathcal{P}_m(\mathbb{R}^d) = span\{p_1, p_2, \ldots, p_Q\}$ with $Q = \binom{m+d}{d}$, consists of monomials. In two dimension this is

$$\mathbf{p}(\mathbf{x}) = \mathbf{p}(x, y) = \{p_0\, p_1\, \ldots\, p_Q\} = \{1\; x\; y\; xy\; x^2\; y^2\; \ldots\; x^m\; y^m\}, \tag{3.66}$$

and in three dimensions, a basis like

$$\mathbf{p}(\mathbf{x}) = \mathbf{p}(x, y, z) = \{p_0\, p_1\, \ldots\, p_Q\} = \{1\; x\; y\; z\; xyz\; x^2\; y^2\; z^2\; \ldots\; x^m\; y^m\; z^m\} \tag{3.67}$$

can be used. Using such polynomial basis, care must be taken with regard to solve the normal system (3.9). The condition of the matrix $\mathbf{PWP}^T$ is directly linked to the used monomial basis. To ensure a well conditioned normal equation, it is superior to scale and shift the monomial basis to the evaluation point $\mathbf{x}_i$ (Saad, 1986; Mirzaei et al., 2012)

$$p_\alpha\,(\mathbf{x}) = \frac{1}{\alpha!}\left(\frac{\mathbf{x} - \mathbf{x}_i}{h}\right)^\alpha, \quad \alpha = 0, \ldots, Q. \tag{3.68}$$

The choice of the polynomial degree m is important for the convergence of the approximation. Inspecting the error bounds in Theorem 3.1 and 3.2, the polynomial order controls the error according to the used norm of the function space. Nevertheless, using high order polynomial degrees, a trade-off between stability while inverting the matrix $\mathbf{PWP}^T$, and a high order convergence must be found. In order to provide a convergent reconstruction and a stable local polynomial reproduction oversampling is needed: The number of points in the stencil $n = |\Xi|$ must be greater or at least equal to the used polynomial order $m = dim(\mathcal{P})$ (Wendland, 2010). A methodical way to reduce the stencil size and providing a more compact discretization was presented in Trask et al. (2016).

3.5.3 Weight function

In the Moving Least Squares framework a weight function is assigned to each point in the local stencil. This weight function should produce a spatial dependence and prefer points from the evaluation stencil, which are closer to the stencil mid-point. A possible choice is to use a weight function dependent on the Euclidean distance, which is rotationally invariant. The Euclidean distance in $\mathbb{R}^d$ between two points $\mathbf{x} = (x_1, \ldots, x_d)$ and $\mathbf{y} = (y_1, \ldots, y_d)$ is given by

$$d(\mathbf{x}, \mathbf{y}) = \|\mathbf{x} - \mathbf{y}\|_2 = \sqrt{\sum_{i=1}^{d} (x_i - y_i)^2}. \tag{3.69}$$

This suggests to use a weight $w : \Omega \times \Omega \to \mathbb{R}$ function like

$$z_i(\mathbf{x}) = z(d(\mathbf{x}, \mathbf{x}_i)). \tag{3.70}$$

If the argument of z vanishes and the value of z approaches infinity, the approximation scheme interpolates the wanted function values. Normally, the values of the weight function should attenuate rapidly with an increasing distance. Also, by choosing a maximum support distance $h_0 \leq h_{X,\Omega}$, the weight function should vanish if the argument is greater than this constant:

$$z_i(\mathbf{x}) = z(d(\mathbf{x}, \mathbf{x}_i)) = 0, \quad \forall d(\mathbf{x}, \mathbf{x}_i) > h_0. \tag{3.71}$$

If the weight function posses a k-smoothness (if $w \in C^k$), than the approximation $\mathcal{P}_f(\mathbf{x})$ is also in C^k (Wendland, 2010). A reasonable choice for a weight function is

$$z_i(\mathbf{x}) = z(d(\mathbf{x}, \mathbf{x}_i)) = \begin{cases} \frac{exp((-d(\mathbf{x},\mathbf{x}_i)/c)^2) - exp(-(h_0/c)^2)}{1 - exp(-(h_0/c)^2)} & \text{for } 0 \leq d(\mathbf{x}, \mathbf{x}_i) \leq h_0, \\ 0 & \text{for } h_0 < d(\mathbf{x}, \mathbf{x}_i). \end{cases} \tag{3.72}$$

In Equation (3.72), a constant value c is used to control the shape of the weight function and an often used value is $c = 0.6$ (Mirzaei and Schaback, 2013).

3.5.4 Two-dimensional implementations

As before, the computational domain is covered by a point set $X = \{\mathbf{x}_i\}_{i=1,\ldots,N}$ divided into $X = X_\Omega \cup X_d \cup X_n$, in which $X_\Omega \subset \Omega \subsetneq \mathbb{R}^2$ are points inside the domain Ω, whereas $X_D \subset \Gamma^D$ are points on a Dirichlet boundary and $X_N \subset \Gamma^N$ are points on a Neumann

boundary. A stencil $\Xi_i = \{\mathbf{x}_i, \mathbf{x}_1, \mathbf{x}_2, \ldots, \mathbf{x}_n\}$ for the point $\mathbf{x}_i$ is formed from a number of surrounding points $\{\mathbf{x}_j\}_{j=1}^n$, specifically: $\Xi_i := \{\mathbf{x}_j \in \Omega \mid ||\mathbf{x}_i - \mathbf{x}_j||_2 < h\}$. Now, for every stencil in the computational domain, the coefficients of the local expansion of the functionals for the specific boundary value problem have to be computed. The proposed generalized form of the two-dimensional magnetotelluric boundary value problem (3.43)

$$\begin{aligned} \nabla \cdot \left(C^A(\mathbf{x})\nabla u(\mathbf{x})\right) + C^B(\mathbf{x})u(\mathbf{x}) &= s(\mathbf{x}) \qquad \text{in } \Omega, \\ u(\mathbf{x}) &= u^{1D}(\mathbf{x}) \quad \text{on } \Gamma^D, \\ C^A(\mathbf{x})\frac{\partial u}{\partial \mathbf{n}}(\mathbf{x}) &= g(\mathbf{x}) \qquad \text{on } \Gamma^N, \end{aligned} \tag{3.73}$$

will be used for the two-dimensional calculations. The coefficients for the TE-mode can be identified as $C^A(\mathbf{x}) = \mu_0^{-1}$ and $C^B(\mathbf{x}) = -i\omega\sigma(\mathbf{x})$, whereas for the TM-mode the coefficients are $C^A(\mathbf{x}) = \sigma(\mathbf{x})^{-1}$ and $C^B(\mathbf{x}) = -i\omega\mu_0$. This gives two sets of functionals, one for the TE mode and one for the TM mode. First the functionals for the TE mode are given by

$$\begin{aligned} L_i^{\Omega}(E_x) &:= \nabla \cdot \left(\mu_0^{-1}\nabla E_x(\mathbf{x}_i)\right) - i\omega\sigma(\mathbf{x}_i)E_x(\mathbf{x}_i), && \mathbf{x}_i \in X_\Omega \subset \Omega, \\ L_j^{D}(E_x) &:= \delta_{\mathbf{x}_j} \circ E_x, && \mathbf{x}_j \in X_D \subset \Gamma^D, \\ L_l^{N}(E_x) &:= \mu_0^{-1}\frac{\partial E_x}{\partial \mathbf{n}}(\mathbf{x}_l), && \mathbf{x}_l \in X_N \subset \Gamma^N. \end{aligned} \tag{3.74}$$

The specific functionals for the TM mode are given by

$$\begin{aligned} L_i^{\Omega}(H_x) &:= \nabla \cdot \left(\sigma(\mathbf{x})^{-1}\nabla H_x(\mathbf{x}_i)\right) - i\omega\mu_0 H_x(\mathbf{x}_i), && \mathbf{x}_i \in X_\Omega \subset \Omega, \\ L_j^{D}(H_x) &:= \delta_{\mathbf{x}_j} \circ H_x, && \mathbf{x}_j \in X_D \subset \Gamma^D, \\ L_l^{N}(H_x) &:= \sigma(\mathbf{x})^{-1}\frac{\partial H_x}{\partial \mathbf{n}}(\mathbf{x}_l), && \mathbf{x}_l \in X_N \subset \Gamma^N. \end{aligned} \tag{3.75}$$

Now for every point inside the computational domain, the set of functionals will be approximated according to a local expansion based on the specific stencil of the point. The right functional will be selected according to the placement of the point. If a point does not belong to a boundary set, the first functional of Equations (3.74) or (3.75) will be used. If the point is on a boundary the corresponding functionals for the boundary will be used. The approximation of a functional according to the local stencil is

$$L_i^l(u) \approx \sum_{j=1}^{n} a_{ij}^l(L_i)\, u(\mathbf{x}_j), \tag{3.76}$$

where $l = \{\Omega, D, N\}$ is the descriptor of the functional. Using the introduced monomial basis and the weight functions, the coefficients can be calculated by Equation (3.9)

$$\mathbf{a}^l(L) = \mathbf{WP}(\mathbf{P}^T\mathbf{WP})^{-1}\mathbf{L}^l(\mathcal{P}). \tag{3.77}$$

The weighting matrix is explicitly given by

$$\mathbf{W} = diag(w(\mathbf{x}_1), \ldots, w(\mathbf{x}_n)) = \begin{pmatrix} w(\mathbf{x}_1) & \ldots & 0 \\ 0 & \ddots & 0 \\ 0 & \ldots & w(\mathbf{x}_n) \end{pmatrix}, \tag{3.78}$$

and the monomial basis is used for forming

$$\mathbf{P} = \begin{pmatrix} p_1(\mathbf{x}_1) & p_2(\mathbf{x}_1) & \ldots & p_q(\mathbf{x}_1) \\ p_1(\mathbf{x}_2) & p_2(\mathbf{x}_2) & \ldots & p_q(\mathbf{x}_2) \\ p_1(\mathbf{x}_3) & p_2(\mathbf{x}_3) & \ldots & p_q(\mathbf{x}_3) \\ \ldots & \ldots & \ldots & \ldots \\ p_1(\mathbf{x}_n) & p_2(\mathbf{x}_n) & \ldots & p_q(\mathbf{x}_n) \end{pmatrix}. \tag{3.79}$$

Special for the generalized moving least squares is the vector of functionals $\mathbf{L}^l(\mathcal{P})$ acting on the monomial basis, which should be calculated according to the selected functionals. By inspecting Equations (3.74) and (3.75) they can be written for the TE-mode as

$$\begin{aligned}
\mathbf{L}_i^{\Omega}(\mathcal{P}) &:= \left[\nabla \cdot \left(\mu_0^{-1}\nabla p_1(\mathbf{x}_i)\right) - i\omega\sigma(\mathbf{x}_i)p_1(\mathbf{x}_i), \ldots, \nabla \cdot \left(\mu_0^{-1}\nabla p_Q(\mathbf{x}_i)\right) - i\omega\sigma(\mathbf{x}_i)p_Q(\mathbf{x}_i)\right]^T, \\
\mathbf{L}_j^{D}(\mathcal{P}) &:= \left[p_1(\mathbf{x}_j), p_2(\mathbf{x}_j), \ldots, p_Q(\mathbf{x}_j)\right]^T, \\
\mathbf{L}_l^{N}(\mathcal{P}) &:= \left[\mu_0^{-1}\frac{\partial p_1}{\partial \mathbf{n}}(\mathbf{x}_l), \mu_0^{-1}\frac{\partial p_2}{\partial \mathbf{n}}(\mathbf{x}_l), \ldots, \mu_0^{-1}\frac{\partial p_Q}{\partial \mathbf{n}}(\mathbf{x}_l)\right],
\end{aligned} \tag{3.80}$$

and for the TM-mode as

$$\begin{aligned}
\mathbf{L}_i^{\Omega}(\mathcal{P}) &:= \left[\nabla \cdot \left(\sigma(\mathbf{x}_i)^{-1}\nabla p_1(\mathbf{x}_i)\right) - i\omega\mu_0 p_1(\mathbf{x}_i), \ldots, \nabla \cdot \left(\sigma(\mathbf{x}_i)^{-1}\nabla p_Q(\mathbf{x}_i)\right) - i\omega\mu_0 p_Q(\mathbf{x}_i)\right]^T, \\
\mathbf{L}_j^{D}(\mathcal{P}) &:= \left[p_1(\mathbf{x}_j), p_2(\mathbf{x}_j), \ldots, p_Q(\mathbf{x}_j)\right]^T, \\
\mathbf{L}_l^{N}(\mathcal{P}) &:= \left[\sigma(\mathbf{x}_l)^{-1}\frac{\partial p_1}{\partial \mathbf{n}}(\mathbf{x}_l), \sigma(\mathbf{x}_l)^{-1}\frac{\partial p_2}{\partial \mathbf{n}}(\mathbf{x}_l), \ldots, \sigma(\mathbf{x}_l)^{-1}\frac{\partial p_Q}{\partial \mathbf{n}}(\mathbf{x}_l)\right].
\end{aligned} \tag{3.81}$$

The next step is to make use of the previously described staggered scheme. As noted before, the numerical procedure should be able to handle discontinuous material coefficients.

Make use of the staggered scheme is a step towards an efficient implementation to handle discontinuous material coefficients. To proceed, the functional vector $\mathbf{L}_i^{\Omega}(\mathcal{P})$ will be split into two parts as

$$\begin{aligned}\mathbf{L}_i^{\Omega_a}(\mathcal{P}) &:= \left[\nabla\cdot\left(\mu_0^{-1}\nabla p_1(\mathbf{x}_i)\right),\ldots,\nabla\cdot\left(\mu_0^{-1}\nabla p_Q(\mathbf{x}_i)\right)\right]^T,\\ \mathbf{L}_i^{\Omega_b}(\mathcal{P}) &:= \left[-i\omega\sigma(\mathbf{x}_i)p_1(\mathbf{x}_i),\ldots,\ldots,-i\omega\sigma(\mathbf{x}_i)p_Q(\mathbf{x}_i)\right]^T,\end{aligned} \tag{3.82}$$

for the TE-mode and for the TM mode accordingly

$$\begin{aligned}\mathbf{L}_i^{\Omega_a}(\mathcal{P}) &:= \left[\nabla\cdot\left(\sigma(\mathbf{x}_i)^{-1}\nabla p_1(\mathbf{x}_i)\right),\ldots,\nabla\cdot\left(\sigma(\mathbf{x}_i)^{-1}\nabla p_Q(\mathbf{x}_i)\right)\right]^T,\\ \mathbf{L}_i^{\Omega_b}(\mathcal{P}) &:= \left[-i\omega\mu_0 p_1(\mathbf{x}_i),\ldots,\ldots,-i\omega\mu_0 p_Q(\mathbf{x}_i)\right]^T.\end{aligned} \tag{3.83}$$

Now, according to Trask et al. (2017) the minimization problem defined in Equation (3.28) will be used to form an expression like Equation (3.77) to calculate coefficients in a staggered approximation to the functionals $\mathbf{L}_i^{\Omega_a}(\mathcal{P})$ for the TE- and TM-mode.
Using the definition of the topological gradient in Equations (3.24) together with the minimization problem (3.28) gives

$$min\left\{\sum_{j=1}^{n}\left(\widetilde{c_{ij}}\,GRAD_i(u)-p(\mathbf{x}_{ij})\right)^2 w(\mathbf{x}_i,\mathbf{x}_{ij})\ :\ p\in P^i\right\}. \tag{3.84}$$

In this minimization problem, where $p^*(\mathbf{x}_i)$ is a solution, the gradient operator is defined through the relation $GRAD_i(u) = u(\mathbf{x}_j) - u(\mathbf{x}_i)$, which previously was written down in Equation (3.24). Also, included in the minimization is an average material parameter $\widetilde{c_{ij}}$ between points $\mathbf{x}_i$ and $\mathbf{x}_j$. The right calculation of this parameter will be justified in the next chapter. The solution of the minimization problem gives a *staggered* coefficient vector as

$$\mathbf{a}_{ij}^{stagg}(L) = \frac{1}{4}\mathbf{\Sigma}_{ij}\mathbf{W}\mathbf{P}(\mathbf{P}^T\mathbf{W}\mathbf{P})^{-1}\mathbf{L}^{stagg}(\mathcal{P}). \tag{3.85}$$

The material parameter enters the equation as a diagonal matrix $\mathbf{\Sigma}_{ij} = diag(\widetilde{c_{i1}},\ldots,\widetilde{c_{in}})$, assembled with all averaged values from the stencil and the factor of $\frac{1}{4}$ is due Lemma 3.1. The functional occurring in the last part of Equation (3.85) can explicitly be written as

$$\mathbf{L}_i^{stagg}(\mathcal{P}) := \left[\Delta p_1(\mathbf{x}_i),\ldots,\Delta p_Q(\mathbf{x}_i)\right]^T. \tag{3.86}$$

This staggered method *chains* the approximation, so that

$$\begin{aligned}\nabla \cdot \left(C^A(\mathbf{x}_i)\nabla u(\mathbf{x}_i)\right)_i &= DIV_i \circ \widetilde{c_{ij}}\, GRAD_i(u) \\ &= \frac{1}{4}\Delta p^*(\mathbf{x}_i) \\ &= \sum_j^n a_{ij}^{stagg}(u(\mathbf{x}_j) - u(\mathbf{x}_i)).\end{aligned} \tag{3.87}$$

It can be seen that an approximate solution for the boundary value problem (3.43) can be constructed in two ways using strong point collocation techniques. First, a pure collocation technique can be applied through an approximation of the functionals (3.74) and (3.75). In a second way, using the staggered divergence operator, both techniques can be mixed to form an approximation technique, which is capable to handle spatial varying material parameters. The difference, including these parameters can be seen in the formulation described up to now. Using the *classical* point collocation scheme, the material parameter enters the approximation with defining the functionals (3.80) and (3.81) this keeps the material parameter constant over the stencil. Using the staggered scheme, an averaged material parameter can be used in the functional approximation. This procedure will be analysed in the subsequent chapter about approximations in the presence of material interfaces.

To derive an implementation for the two-dimensional weak formulation, the functionals in (3.62) must be approximated. Luckily, compared to the pure point collocation technique, only the functionals for the interior points change. Boundary conditions can be implemented as before using the collocation technique. This gives a direct approximation of the boundary conditions and a local weak form approximation for the interior points. This rather mixed approach was already proposed in the seminal publication about the DMLPG method (Mirzaei and Schaback, 2013). To use the weak formulation, only the functionals (3.82) and (3.83) should be changed according to equations (3.62). The right functionals for the TE-mode are

$$\begin{aligned}L_i^1(E_x) &:= \int_{\Gamma_s^i \setminus \Gamma_i^N} (i\omega\mu_0)^{-1} \frac{\partial E_x}{\partial \mathbf{n}}(\mathbf{x}_i)\; d\Gamma, \\ L_i^2(E_x) &:= -\int_{\Omega_s^i} \sigma(\mathbf{x}_i) E_x(\mathbf{x}_i)\, d\Omega,\end{aligned} \tag{3.88}$$

whereas the index i referees to the interior point set. Also, for the TM-mode the functionals are

$$\begin{aligned} L_i^1(H_x) &:= \int\limits_{\Gamma_s^i \setminus \Gamma_i^N} \sigma(\mathbf{x}_i)^{-1} \frac{\partial H_x}{\partial \mathbf{n}}(\mathbf{x}_i)\ d\Gamma, \\ L_i^2(H_x) &:= -\int\limits_{\Omega_s^i} i\omega\mu_0 H_x(\mathbf{x}_i)\, d\Omega. \end{aligned} \tag{3.89}$$

Here, the indexing has to be done with caution. The domains of integration (Γ_s^i, Ω_s^i) should not be confounded with the computational domains. Now, by applying the functionals to the monomial basis, the functional vectors for the normal system (3.77) using different point sets, can be derived

$$\begin{aligned} \mathbf{L}_i^{\Gamma}(\mathcal{P}) &:= (i\omega\mu_0)^{-1} \left[\int\limits_{\Gamma_s^i} \frac{\partial p_1}{\partial \mathbf{n}}(\mathbf{x}_i)\ d\Gamma, \ldots, \int\limits_{\Gamma_s^i} \frac{\partial p_q}{\partial \mathbf{n}}(\mathbf{x}_i)\ d\Gamma \right]^T, \\ \mathbf{L}_i^{\Omega}(\mathcal{P}) &:= \left[-\int\limits_{\Omega_s^i} \sigma(\mathbf{x}_i) p_1(\mathbf{x}_i)\, d\Omega, \ldots, -\int\limits_{\Omega_s^i} \sigma(\mathbf{x}_i) p_q(\mathbf{x}_i)\, d\Omega \right]^T, \\ \mathbf{L}_j^{D}(\mathcal{P}) &:= \left[p_1(\mathbf{x}_j), p_2(\mathbf{x}_j), \ldots, p_Q(\mathbf{x}_j) \right]^T, \\ \mathbf{L}_l^{N}(\mathcal{P}) &:= \left[\mu_0^{-1} \frac{\partial p_1}{\partial \mathbf{n}}(\mathbf{x}_l), \mu_0^{-1} \frac{\partial p_2}{\partial \mathbf{n}}(\mathbf{x}_l), \ldots, \mu_0^{-1} \frac{\partial p_Q}{\partial \mathbf{n}}(\mathbf{x}_l) \right], \end{aligned} \tag{3.90}$$

for the TM-mode as

$$\begin{aligned} \mathbf{L}_i^{\Gamma}(\mathcal{P}) &:= \left[\int\limits_{\Gamma_s^i} \sigma(\mathbf{x}_i)^{-1} \frac{\partial p_1}{\partial \mathbf{n}}(\mathbf{x}_i)\ d\Gamma, \ldots, \int\limits_{\Gamma_s^i} \sigma(\mathbf{x}_i)^{-1} \frac{\partial p_q}{\partial \mathbf{n}}(\mathbf{x}_i)\ d\Gamma \right]^T, \\ \mathbf{L}_i^{\Omega}(\mathcal{P}) &:= -i\omega\mu_0 \left[\int\limits_{\Omega_s^i} p_1(\mathbf{x}_i)\, d\Omega, \ldots, \int\limits_{\Omega_s^i} p_q(\mathbf{x}_i)\, d\Omega \right]^T, \\ \mathbf{L}_j^{D}(\mathcal{P}) &:= \left[p_1(\mathbf{x}_j), p_2(\mathbf{x}_j), \ldots, p_Q(\mathbf{x}_j) \right]^T, \\ \mathbf{L}_l^{N}(\mathcal{P}) &:= \left[\sigma(\mathbf{x}_l)^{-1} \frac{\partial p_1}{\partial \mathbf{n}}(\mathbf{x}_l), \sigma(\mathbf{x}_l)^{-1} \frac{\partial p_2}{\partial \mathbf{n}}(\mathbf{x}_l), \ldots, \sigma(\mathbf{x}_l)^{-1} \frac{\partial p_Q}{\partial \mathbf{n}}(\mathbf{x}_l) \right]. \end{aligned} \tag{3.91}$$

Using these vectors together with Equation (3.77), the coefficients for the weak formulation can be derived. As it can be seen, the integration from the weak formulation is shifted to integration over the low-degree polynomials. This is beneficial compared to other

meshless formulations, where complex shape functions have to be evaluated inside high order quadrature routines.
The coefficients (3.77) and (3.85) as well as in the weak formulation, have compact support due to the local nodal stencil and the weight function. This leads to a sparse matrix, which has n-entries in each row, where n is the number of points used in the stencil. It follows that the sparse system (3.48)

$$\boldsymbol{A}\mathbf{u} = \mathbf{s}, \tag{3.92}$$

will be row-wise constructed and the i-th row is filled with the coefficient vector resulting from a solution of the normal system (3.77) with respect to the i-th point. Subsequently, the bandwidth of this sparse matrix depends on the number of points used in the stencil and can vary in each row. Therefore, there is a strong trade-off between a stable approximation and solving the sparse linear system of equation. Since oversampling is needed to provide a stable functional reconstruction, the limit has to be found, where additional points do not provide more stability to the approximation and do not increase the bandwidth of the system matrix. An algorithm to circumvent this problem, using kernel based approximation, was given by Schaback (2014) and used in solving heat conduction problems (Fadaei and Moghadam, 2017).

3.5.5 Three-dimensional implementation

By describing the two-dimensional approximation techniques first, the three-dimensional case naturally follows. Now, the difference is assuming a domain covered by a point set $X = \{\mathbf{x}_i\}_{i=1,\dots,N}$, which is divided into $X = X_\Omega \cup X_d \cup X_n$, in which $X_\Omega \subset \Omega \subsetneq \mathbb{R}^3$ are points inside the domain Ω, where $X_D \subset \Gamma^D$ are points on a Dirichlet boundary and $X_N \subset \Gamma^N$ are points on a Neumann boundary. A stencil $\Xi_i = \{\mathbf{x}_i, \mathbf{x}_1, \mathbf{x}_2, \dots, \mathbf{x}_n\}$ for the point $\mathbf{x}_i$ is formed, as before from a number of surrounding points $\{\mathbf{x}_j\}_{j=1}^n$, specifically: $\Xi_i := \{\mathbf{x}_j \in \Omega \mid ||\mathbf{x}_i - \mathbf{x}_j||_2 < h\}$.
The task now is to find coefficients for the approximations of the functionals, according to the vector potential description. Here, an approximation of the functionals (3.50 - 3.52) with the help of the generalized moving least squares technique must be derived. Luckily, all needed formulations are already given in the implementation for the two-dimensional scheme. As discussed before, the vector potential formulation can be treated as a system of independent, but weakly coupled equations. Therefore, it is possible to approximate each functional for each field component separately and no real vector formulation is required. Only the part, in which the coefficients are inserted into the global matrix needs

to be carefully implemented.
First, the basis monomials is now the weighted and scaled version of Equation (3.67) and used together with a three-dimensional implementation of the weight function in Equation (3.72). All operators such as the divergence or the gradient operator now act on three spatial dimensions, while possible derivatives with respect to a normal vector are also in three dimension[6]. With these preconditions, the two-dimensional scheme for the functional approximation can be transferred to the three-dimensional case only with slight modifications.
For the functionals (3.50) and (3.52) everything was defined in the previous description about the two dimensional implementation. For the approximation of the diagonal term in Equation (3.49) a mixed formulation is recommended. The parts which belong to the vector potential $\mathbf{A}$ will be discretized using the pure collocation scheme. Since the scalar potential comprises possible jumps at material interfaces, it will be discretized using the staggered scheme. For the sake of completeness, the vectors resulting from the application of the functionals onto the monomial basis will be repeated.
For the diagonal terms this will be

$$\begin{aligned}
\mathbf{L}_{A_x}^{\Omega_i}(\mathcal{P}) &:= \left[\nabla^2 p_1(\mathbf{x}_i) + i\omega\hat{\sigma}(\mathbf{x}_i)p_1(\mathbf{x}_i), \ldots, \nabla^2 p_Q(\mathbf{x}_i) + i\omega\hat{\sigma}(\mathbf{x}_i)p_Q(\mathbf{x}_i)\right]^T, \\
\mathbf{L}_{A_y}^{\Omega_i}(\mathcal{P}) &:= \left[\nabla^2 p_1(\mathbf{x}_i) + i\omega\hat{\sigma}(\mathbf{x}_i)p_1(\mathbf{x}_i), \ldots, \nabla^2 p_Q(\mathbf{x}_i) + i\omega\hat{\sigma}(\mathbf{x}_i)p_Q(\mathbf{x}_i)\right]^T, \\
\mathbf{L}_{A_z}^{\Omega_i}(\mathcal{P}) &:= \left[\nabla^2 p_1(\mathbf{x}_i) + i\omega\hat{\sigma}(\mathbf{x}_i)p_1(\mathbf{x}_i), \ldots, \nabla^2 p_Q(\mathbf{x}_i) + i\omega\hat{\sigma}(\mathbf{x}_i)p_Q(\mathbf{x}_i)\right]^T, \\
\mathbf{L}_{\phi}^{\Omega_i}(\mathcal{P}) &:= \left[\nabla\cdot\left(\hat{\sigma}(\mathbf{x}_i)\nabla p_1(\mathbf{x}_i)\right), \ldots, \nabla\cdot\left(\hat{\sigma}(\mathbf{x}_i)\nabla p_Q(\mathbf{x}_i)\right)\right]^T.
\end{aligned} \tag{3.93}$$

In comparison to the two-dimensional formulation, one functional included in the three-dimensional approach was not described. The off-diagonal terms, which couple the individual field components, should now be examined. Here the functionals are

$$L_i^{P_l}(u) := \mu_0\hat{\sigma}(\mathbf{x}_i)\partial_l u(\mathbf{x}_i), \tag{3.94}$$

with $l \in \{x, y, z\}$ and defined for interior points. Using the monomial basis, the resulting vector for the normal equation can be written as

$$\mathbf{L}_{P_l}^{\Omega_i}(\mathcal{P}) := \left[\mu_0\hat{\sigma}(\mathbf{x}_i)\partial_l p_1(\mathbf{x}_i), \ldots, \mu_0\hat{\sigma}(\mathbf{x}_i)\partial_l p_q(\mathbf{x}_i)\right]^T. \tag{3.95}$$

[6]For example when $\frac{\partial u}{\partial \mathbf{n}}$ is required, it should be calculated as $\frac{\partial u}{\partial \mathbf{n}} = \mathbf{n}\cdot\nabla u = n_x\partial_x u + n_y\partial_y u + n_z\partial_z u$, when $\mathbf{n} \in \mathbb{R}^3$ and $\nabla = (\partial_x, \partial_y, \partial_z)^T$, as well as $u : \mathbb{R}^3 \to \mathbb{R}$

Up to now, everything is defined to calculate the expansions of the functionals for the three-dimensional formulation. If a boundary condition should be approximated, for example as defined in Equations (3.52), the methods from the two-dimensional scheme could also be applied. However, even if some methods from the two-dimensional scheme can be reused, the critical part is the correct assembly of the sparse system matrix. Due to the coupling of the differential equation system the coefficients for the approximation of the occurring functionals should be treated with care. Starting from the block character of the coefficient matrix in the expansion (3.54) of the functional, the coefficients should be calculated according to the operator form notation from Equation (3.49). Writing the whole system of coefficients accordingly and with careful labeling, this reads

$$\begin{aligned} L_i(\mathbf{u}) \approx \sum_{j=1}^{n} \mathbf{A}_{ij}\mathbf{u}(\mathbf{x}_j) &= \sum_{j=1}^{N} \begin{pmatrix} a_{ij}^{A_x} & 0 & 0 & a_{ij}^{P_x} \\ 0 & a_{ij}^{A_y} & 0 & a_{ij}^{P_y} \\ 0 & 0 & a_{ij}^{A_z} & a_{ij}^{P_z} \\ a_{ij}^{P_x} & a_{ij}^{P_y} & a_{ij}^{P_z} & a_{ij}^{\phi} \end{pmatrix} \begin{pmatrix} A_x(\mathbf{x}_j) \\ A_y(\mathbf{x}_j) \\ A_z(\mathbf{x}_j) \\ \phi(\mathbf{x}_j) \end{pmatrix} \\ &= \mathbf{s}_i(\mathbf{x}_i), \quad \forall \mathbf{x}_i \in \Omega \cup \Gamma^D \cup \Gamma^N. \end{aligned} \tag{3.96}$$

The i-th row of the matrix $\mathbf{A}_{ij}$ represents the i-th block row of the coefficient matrix of the final sparse linear system. It should be noted, that this system is populated block-wise with the index j as column index. When describing boundary conditions the coefficient matrix from Equation (3.96) is a diagonal matrix without coupling terms.

3.6 Interface description

Up to now, one question remains unanswered: how to discretize the partial differential equations, when the conductivity σ is piecewise constant or varies smoothly over the computational domain. The latter case is already covered by the actual implementation. When $\sigma \in C^n$ with $n \geq 1$ and spatially varies over the computational domain the generalized moving least squares will produce high-order continuity fields. Nevertheless, the high-order continuity imposes difficulties when considering conductivity discontinuities, which incur jumps in electromagnetic fields across a conductivity interface.
As noted before, this behaviour can be observed in the partial differential equation for the two-dimensional case in the TM-mode, as well as in the partial differential equation for the scalar potential in the three-dimensional formulation. They are both described by a

differential equation of the form

$$\begin{aligned} \nabla \cdot (\sigma(\mathbf{x})\nabla u(\mathbf{x})) + \beta(\mathbf{x})u(\mathbf{x}) &= s(\mathbf{x}) \quad \text{in } \Omega^{1,2}, \\ u(\mathbf{x}) &= g(\mathbf{x}) \quad \text{on } \Gamma. \end{aligned} \tag{3.97}$$

Including the conductivity $\sigma(\mathbf{x})$ in the first term and a material parameter $\beta(\mathbf{x})$ in the second term. At an interface, the fields are connected to boundary values generated by $g(\mathbf{x})$. Inspecting the first equation of (3.97), it can be determined that if the conductivity is discontinuous at an interface Γ^{int} separating two domains Ω^1 and Ω^2, jump conditions at this interface must be considered. Here, the field u must comply with

$$\begin{aligned} \left[u(\mathbf{x})\right]_{\Gamma^{int}} &= u^1(\mathbf{x}) - u^2(\mathbf{x}) = k_1(\mathbf{x}), \\ \left[\sigma(\mathbf{x})\frac{\partial u(\mathbf{x})}{\partial \mathbf{n}}\right]_{\Gamma^{int}} &= \sigma^1(\mathbf{x})\frac{\partial u^1(\mathbf{x})}{\partial \mathbf{n}} - \sigma^2(\mathbf{x})\frac{\partial u^2(\mathbf{x})}{\partial \mathbf{n}} = k_2(\mathbf{x}). \end{aligned} \tag{3.98}$$

If $k_1(\mathbf{x}) = 0$ and $k_2(\mathbf{x}) = 0$, these conditions are called homogeneous. This is the case in magnetotelluric modelling. In the engineering community often a distinction is made, how the fields behave at an interface. If the field only has a kink at the interface, for example if the interface conditions are homogeneous, they belong to the family of weak discontinuities. If the field value has a jump in its magnitude at an interface, this case is often called a strong discontinuity (Fries and Belytschko, 2006). Nevertheless, this formulation resembles the well known *elliptic interface problem*, which is of great importance in the correct numerical description of partial differential equations. Generally in a broader setting, if the source s is a function of $L^2(\Omega)$ on the bounded domain Ω and the coefficient (in this case here, the conductivity) are functions of $L^\infty(\Omega)$, the numerical procedure must construct an approximation for a second order elliptic problem with rough coefficients. In the geosciences this problem arises, when Earth formations with high conductivity contrasts are existent. Normally, these problems are solved by mesh-based algorithms with elements, which are conform to the interfaces. But for example finite element methods can perform arbitrarily bad in these cases if the interfaces do not align to the mesh (Babuška and Osborn, 2000). Methods to construct approximations for Equation (3.97) have been developed since decades. A recent overview of homogenization techniques was presented, for example by Owhadi and Zhang (2011).

To put the main focus on meshless methods, some recent developments will be presented here. A first review on different techniques to handle material interfaces was presented by Herault and Marechal (1999). They present some early approaches to handle interface conditions, but their review does not include comparative results from these methods.

Thereafter, a lot of different methods to handle material interfaces had been developed. They can be coarsely catalogued in a following way:

- 'double node' approach,
- enrichment or modification of the approximation space,
- Lagrange multiplier technique,
- material averaging techniques.

One of the most used methods to incorporate interface conditions is the 'double node' approach. In the context of Equations (3.97), these methods directly approximate the interface conditions (3.98) using a meshless method. At the interface a 'double' layer of points is placed and for every side of the layer an approximation is done. Here, the field values are approximated as a linear combination of some coefficients (marked with an appropriate subscript) with the field values:

$$\begin{aligned}
\left[u(\mathbf{x}_i)\right]_{\Gamma^{int}} &= u^1(\mathbf{x}_i) - u^2(\mathbf{x}_i) \\
&\approx \sum_{j=1}^{n1} a_{ij}^{(\delta_x)}\, u(\mathbf{x}_j) - \sum_{j=1}^{n2} a_{ij}^{(\delta_x)}\, u(\mathbf{x}_j) = k_1(\mathbf{x}_i), \quad \forall \mathbf{x}_i \in \Gamma^{int}, \\
\left[\sigma(\mathbf{x}_i)\frac{\partial u(\mathbf{x}_i)}{\partial \mathbf{n}}\right]_{\Gamma^{int}} &= \sigma^1(\mathbf{x}_i)\frac{\partial u^1(\mathbf{x}_i)}{\partial \mathbf{n}} - \sigma^2(\mathbf{x}_i)\frac{\partial u^2(\mathbf{x}_i)}{\partial \mathbf{n}} \\
&\approx \sum_{j=1}^{n1} a_{ij}^{(\partial n)}\, u(\mathbf{x}_j) - \sum_{j=1}^{n2} a_{ij}^{(\partial n)}\, u(\mathbf{x}_j) = k_2(\mathbf{x}_i), \quad \forall \mathbf{x}_i \in \Gamma^{int}.
\end{aligned} \tag{3.99}$$

When using a 'double node' approach, these additional approximations, which are needed to fulfill the interface conditions, increases the size of the system matrix. Every point in the double layer increase the size of the system matrix by two. In addition, for each point on the interface two sets of coefficients have to be calculated. The point stencil will be split into two sets, according to the side of the interface. A schematic description of this process can be seen in Figure 3.9. This method increases the overall computational effort, nevertheless many researchers have used this method to increase the error performance of their computations. Cai and Zhu (2004) used this approach to model mechanical systems, while Aziz and Haider (2017) used this method in a collocation scheme. Recently, Taleei and Dehghan (2014b) used this approach to handle interface condition, while the same authors extend it to model electrostatic phenomena with a direct approximation method (Taleei and Dehghan, 2014a). In this thesis the 'double node' approach will

be used to handle interfaces with high material contrasts like the air-Earth interface. The reason, to use this method for magnetotelluric modelling, is the need of a precise air-Earth description. A layer of points is already present at this interface, because the apparent resistivities and phases should be computed here. To add another layer of points at this interface easily makes the 'double node' approach attractive. Besides using the 'double node' approach, the enrichment of the approximation space is also a very popular method to handle discontinuities in meshless approximation schemes. Here, an enrichment of the underlying basis functions takes place to construct custom-tailored approximation spaces, which can handle singularities, material interfaces or jumps in the field variables. Possible enrichments are due to incorporated special functions into the basis or by modifying the weight function. Examples for the first procedure are given for example by Fleming et al. (1997), Yoon et al. (2006) or Kim et al. (2007), while modifications of the weight function are described by Schweitzer and Wu (2014) or Belytschko et al. (1994). Modifications of the underlying basis can be problematic,

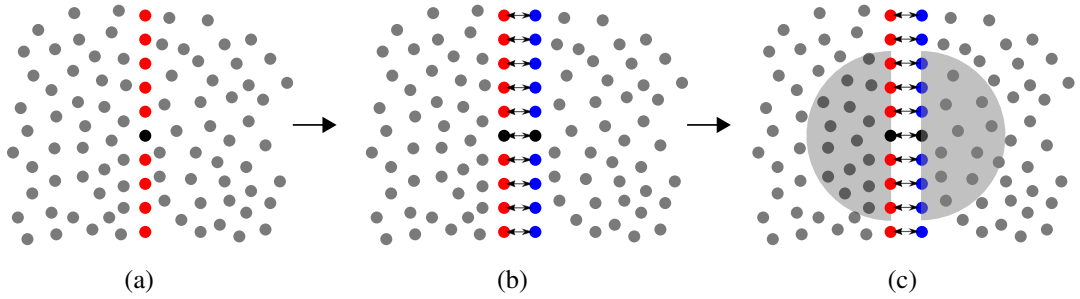

Figure 3.9: Schematic description of the 'double node' approach. (a) displays the point set with the interface points in red and a point which should be evaluated in black. (b) the points will be doubled at the interface. The blue and red points share the same position. (c) If the splitting is done, the approximation of equations (3.99) will be calculated on both sides of the interface.

because the special functions which should enrich the approximation scheme can have an effect on the inversion of the moment matrix (Joyot et al., 2006). When using weak meshless formulations, a possible way to enforce interface conditions is to apply the Lagrange multiplier technique. Here, special terms are added to the weak form of the partial differential equation and by introducing Lagrange multiplier the interface conditions can be described. Examples using this technique are given by Batra et al. (2007), Batra et al. (2004) or Cordes and Moran (1996). The discretization of partial differential equations with rough coefficients or interfaces using averaging schemes have a long history. Early finite difference schemes using material averaging can be dated back to Tikhonov and Samarskii (1962). Recently, special finite difference approximations have been developed, which are referred to as immersed interface methods originally

developed by Leveque and Li (1994). Nevertheless, finite volume schemes lead naturally to a material averaging. By constructing difference schemes from the integration of the flux over a control volume, material averaging occur (Samarskii, 2001; Chernogorova et al., 2002). The link to meshless methods was done in the framework of smoothed particle hydrodynamics, which was used to model heat conduction in heterogeneous media by Cleary and Monaghan (1999). Here, the physical model needs the continuity of heat fluxes across material interfaces, so Cleary and Monaghan (1999) used a simple averaging correction implemented into their numerical formulation successfully. Other smoothed particle hydrodynamic formulations used Taylor series expansions on both sides of the interface to implement a numerical correct scheme (Liu et al., 2003; Xu et al., 2013). These methods are essentially comparable to immersed interface techniques. Nearly all of the presented methods need to know the exact location of the material interface. Especially the 'double node' approach, which also needs a double point layer at the interface. Hence, a lot of enrichment methods use a technique called *level-set* method, originally proposed by Sethian (1999), to describe the evolution of interfaces. Even if high order convergence is obtained by these methods the prior needed location of the interface is often a drawback, especially when using these discretizations in a parameter estimation algorithm. Evolving conductivity contrasts should be easily described by the method, while keeping additional calculations to a minimum. Suitable methods to achieve this are the ones using an averaging technique. Only by considering the conductivity values at the points of the stencil, roughly varying material parameters should be resolved. The first step to handle these changes in the conductivity distributions is to exterminate possible averaging techniques in combination with the staggered moving least squares technique of Trask et al. (2017). Here, the combination of both methods will be physically justified and extended for the application to magnetotelluric modelling. In all computations, the air-Earth interface remains fixed. Here, the 'double node' approach will be used to describe this interface. Nevertheless, by inspecting the partial differential

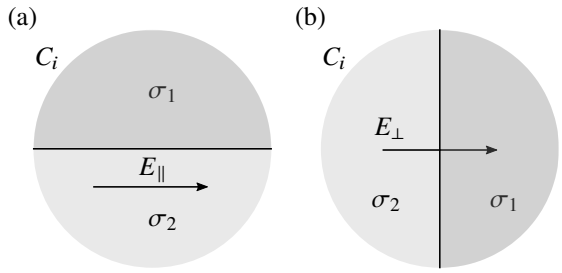

Figure 3.10: Dual Cell with two different conductivities σ_1 and σ_2. In (a), the electrical field is parallel to the contrast, in (b) the electrical field is perpendicular to the contrast.

equation systems defined in the chapter 2.7.5, similar assumptions can be made about different averaging techniques. This is also normally done in finite differences time domain methods (Bijan et al., 1997; Marcysiak and Gwarek, 1994; Przybyszewski, 2001). By using the dual cell C_i as before and dividing it into two parts, in which every part has his own conductivity, rules can be defined how an averaging should act on the conductivity. Here, two cases can be examined: where the electrical field is parallel to the conductivity contrast and in the latter an electrical field perpendicular to the contrast is present. A sketch of these cells is displayed in Figure 3.10. Now, using Ohm's law an averaged conductivity $\sigma_{\parallel}$ can be derived by

$$\sigma_{\parallel} = \frac{\bar{J}_{\parallel}}{\bar{E}_{\parallel}} = \frac{\frac{1}{S}\left(\iint_{S_1} \sigma_1 E_{\parallel} dS + \iint_{S_2} \sigma_2 E_{\parallel} dS\right)}{\frac{1}{S}\int_S E_{\parallel} dS}. \tag{3.100}$$

In Equation (3.100) the integration is done over parts of the dual cell. Here, S_1 denotes the area corresponding to the conductivity σ_1 and S_2 corresponds to σ_2. The whole area is denoted by S. Assuming a constant electrical field in the whole cell, the known arithmetic average conductivity is

$$\sigma_{\parallel} = \frac{\bar{J}_{\parallel}}{\bar{E}_{\parallel}} = \frac{(\sigma_1 S_1 + \sigma_2 S_2)}{S}. \tag{3.101}$$

In the second case, when the electrical field is perpendicular to the conductivity contrast, a similar averaging scheme can be derived. Here, one finds that

$$\sigma_{\perp} = \frac{\bar{J}_{\perp}}{\bar{E}_{\perp}} = \frac{\frac{1}{S}\int_S J_{\perp} dS}{\frac{1}{S}\left(\iint_{S_1} 1/\sigma_1 \, J_{\perp} dS + \iint_{S_2} 1/\sigma_2 \, J_{\perp} dS\right)}. \tag{3.102}$$

In Equation (3.100) the integration is done over parts of the dual cell. Here, S_1 denotes the area corresponding to the conductivity σ_1 and S_2 corresponds to σ_2. Assuming a constant current in the whole cell, the known harmonic average conductivity is

$$\sigma_{\perp} = \frac{\bar{J}_{\perp}}{\bar{E}_{\perp}} = \frac{S}{(S_1/\sigma_1 + S_2/\sigma_2)}. \tag{3.103}$$

Using these schemes in a finite differences approach, the resulting averages form the effective conductivity from the integro-interpolation formula of Moskow et al. (1998):

$$\sigma_x^{eff} = \left[\int_{x_1}^{x_2} \left[\int_{y1}^{y2} \sigma(x,y) dy \right]^{-1} dx \right]^{-1} . \tag{3.104}$$

In this formula the two presented averaging methods are combined. The effective conductivity σ_x^{eff} in the x-direction is assembled as a harmonic average along the x-direction in combination with an arithmetic average in the y-direction.
Using the staggered meshless method, the conductivity enters the discretization in Equation (3.85) as a diagonal matrix $\mathbf{\Sigma}_{ij}$. This matrix is built from individual averaged conductivities between the stencil mid-point and the surrounding points. As described above, the right average must be used for evaluating the effective conductivity.

3.7 Computational aspects

The numerical solution of partial differential equations is a wide and highly diversified field of research. Especially the use of meshless techniques covers a huge variety of mathematical methods and techniques. Since not all topics can be discussed in this thesis, two aspects should be presented. Beside the discussion of the generalized moving least squares technique, they are most different compared to a finite element or finite difference method. First, the proper generation of point sets will be discussed. The question, how to generate quality point sets in a reasonable amount of time is not a trivial task. In this discussion, the focus should be on how to generate good point sets, whereas the focus lies on domain coverage, spatial density adaption and the generation time.
The second aspect, which should be discussed in this thesis, is how to solve the sparse system of equations, which results from the discretization. Meshless schemes generate sparse linear systems, which can be different compared to a finite element system matrix. Some recent techniques will be discussed and illustrated examples are given in this section.

3.7.1 Generation of point sets

The generation of suitable point sets is a delicate task in a meshless algorithm and needs to be further discussed. Point sets should adapt naturally to the geometry of the computational problem. One of the main promise of meshless methods is to be more flexible than a

triangulation or mesh, which tries to capture the geometry of the problem. Interestingly, there are more scientific publications about meshless approximation techniques and not about generating suitable point sets for these methods. The computational domain should be covered with points somehow in order to make these methods work. Particularly, the simplest method, which can be applied, is to fill the computational domain with equally spaced points. Nevertheless, if a blocky geometry is at hand, this might be suitable for convergence studies, where homogeneity and constant parameters are needed all over the computational domain. But for a further description, where the model involves round or curved geometries, enhanced point distribution should be used. In the case of rectangular grids, the error from a discretization of round interfaces is referred as *staircase* effect. Aruliah (2001) showed that staircasing is not so problematic in the case of diffusive electromagnetic problems, as in dispersive electromagnetic problems. But to capture realistic geometries an increasing effort has to be made in grid refinement. Here, point discretizations are an improvement due to the absence of fixed connections among these points and samplings can be adapted flexibly to the geometric configuration. Nevertheless, some rules have to be made to successfully generate such point sets.
In order to fill a complex geometry with points and adapt the spatial sampling density, a lot of publications suggest to triangulating the domain first and then use these generated points from the triangulation (Du et al., 2002). Popular also is a partition of the domain with a Voronoi diagram and using Lloyd's algorithm to relax the generated point set (Iske, 2000; Du et al., 2002). Also *advancing front* methods (Fornberg and Flyer, 2015) could be used to generate spatially density adapted point sets. To produce a sequence of adapted point sets, it is also possible to turn the generation process upside down and use a thinning algorithm on many points (Iske, 2004). Further, the use of packed, interacting spheres with varying radii and combined with a relaxation algorithm can produce well-behaved computational meshes (Shimada and Gossard, 1995), but this idea can also be applied to generate point sets (Nie et al., 2014). Recently, when using approximation schemes based on radial basis functions, a promising technique has been developed by Schaback (2014). Here, an error functional is defined and a geedy method is used to select points for the computational stencil keeping the error optimal for each selected point. This reverses the process of a discretization, because the numerical procedure is adapted to the existing point set and not the point set is fit to the approximation. Another famous approach is to modify the approximation algorithm to promote sparsity of the resulting linear system of equations presented by Seibold (2006). Also, Davydov and Schaback (2016) prove optimal convergence rates for the approximations of functions from a Sobolev space $W_2^m(\mathbb{R}^d)$, no matter how many approximation points are used and where they are

placed. Nevertheless, this also modifies the approximation to fit to the point set. Here, the geometries of the model is known and the generation of the point set should be adapted to the approximation.

Also there exists a lot of point generating algorithms developed by scientists from the computer vision community. The motivation mainly comes from the development of realistic ray-tracing algorithms, which can be used to generate three-dimensional computer graphics. By using regular spaced sampling pattern, these algorithms generate aliasing artifacts which become noticeable, as for example by Moiré pattern in the pictures. One solution to avoid this problem is to add a small random displacement to the point sampling to alleviate aliasing. The foundation of these problems is the existence of frequencies above a so called Nyquist limit. Computer graphics is a sampling process, because it is build upon discrete pixels, hence it can be probed with tools from the Fourier analysis. This is also an important fact in understanding the human eye: it has a limited number of photoreceptors and therefore is a sampling process, which also suffers from the Nyquist limit. To avoid aliasing, the photoreceptors are places inside the eye in a special pattern. This point pattern is called a *Poisson disk distribution*. When generating such a Poission disk distribution, points are randomly placed, but with the restriction that a minimum separation distance is kept between the samples. When using this sampling for computer vision, the random process adds noise to the image and replaces the aliasing, while keeping a minimum separation distance helps to control the amount of noise (Cook, 1986). Due to the sampling process a Fourier spectra can be determined and these spectra resulting from a Poisson distribution is similar to a blue noise spectra (Kopf et al., 2006). The behavior of these point spectra can be linked to the image quality and generating point sets with carefully adapted frequency distributions to prevent noise or aliasing is a wide area of research (Ebeida et al., 2014).

Interestingly, besides computer vision, point sets with a blue noise characteristics also have a low discrepancy (Ahmed et al., 2016). This is beneficial for the Monte-Carlo integration, because the error of the integration only depends on the discrepancy of the point set and the mathematical statement for this is the famous Koksma-Hlawka inequality (Niederreiter, 1992), which bounds the error in terms of the discrepancy. Nevertheless, in this thesis, the Poisson disk sampling is used to generate point sets for the solution of partial differential equations. This method is chosen, because of the availability of different well-designed algorithms and the possibility to generate point sets, which have a good uniformity. Figure 3.11 displays different point sampling pattern. To characterize this behavior for a point set $X = \{\mathbf{x}_1, \ldots, \mathbf{x}_1\}$, the separation distance is defined by

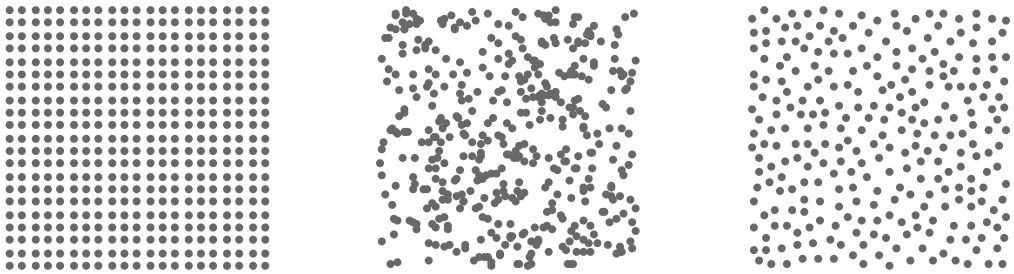

(a) (b) (c)

Figure 3.11: Example of three different point samplings. (a) displays a regular point pattern, (b) the points are placed randomly, (c) displays a Poisson disk sampling pattern.

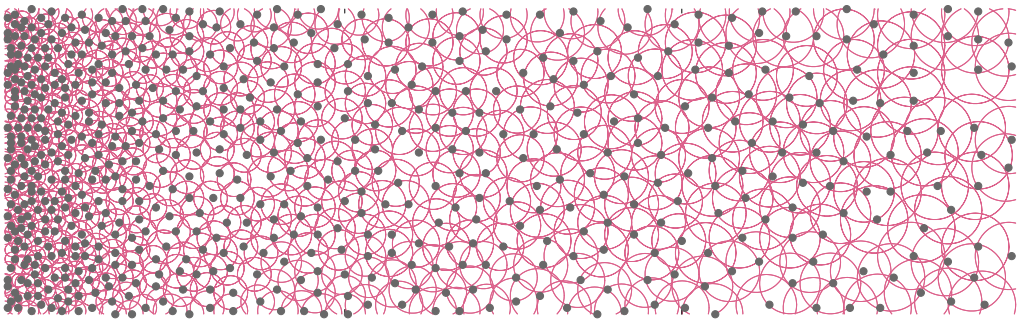

Figure 3.12: Adapted spatial density using a Poisson sampling pattern and variable $h(\mathbf{x})$. The plotted circles around each point are proportional to $h(\mathbf{x})$, while $h(\mathbf{x})$ is adapted to a Eriksson function as defined in Equation (3.107)

$$q_{X,\Omega} = \min_{i \neq j, \{\mathbf{x}_i, \mathbf{x}_j\} \in X} ||\mathbf{x}_i - \mathbf{x}_j||_2, \tag{3.105}$$

and the previously in Equation (3.30) defined fill distance

$$h_{X,\Omega} = \sup_{\mathbf{x} \in \Omega} \min_{\mathbf{x}_i \in X} \|\mathbf{x} - \mathbf{x}_i\|_2 \,. \tag{3.106}$$

As seen before, the fill distance bounds the error of the approximation. Nevertheless, a trade-off between the minimization of $h_{X,\Omega}$ and maximization of $q_{X,\Omega}$ has to be found. Proceeding with the generation of Poisson disk sampling, an algorithm has to be chosen to generate a suitable set of points. As noted before, a variety of algorithms are available to generate Poisson disc samplings e.g. (McCool and Fiume, 1992; Dunbar and Humphreys, 2006; Jones, 2006; Bridson, 2007; Wei, 2008; Lagae and Dutré, 2008; Ascencio-Lopez et al., 2010; Jones and Karger, 2011; Medeiros et al., 2014).

In this thesis, the algorithm of Bridson (2007) is used, because of its simplicity and ability

to generate N density adapted point samplings in $O(N)$ time. The pseudo-code of the

Algorithm 1 Poisson Disk sampling adapted from Bridson (2007)

```
 1: procedure PDSampling(h(x), area, points)
 2:     processList.setup()
 3:     pointList.setup()
 4:     firstpoint ← random(x, y)
 5:     processList.add(firstpoint)
 6:     pointList.add(firstpoint)
 7:     k ← number_of_trials
 8:     while processList.size() ≠ 0 do
 9:         point ← processList.get()
10:         for i ← 0, k do
11:             newpoint ← generate_Point_around(point)
12:             if newpoint.check_allowed(h(x), area) then
13:                 processList.add(newpoint)
14:                 pointList.add(newpoint)
15:             end if
16:         end for
17:     end while
18:     points ← pointList.extract()
19:     return points
20: end procedure
```

used sampling algorithm is listed in Algorithm 1. While maintaining a list, where active points are stored, the algorithm processes this list until it is empty. This is the case, when no new point can be generated and the area, which should be sampled, is full of points. The algorithm will check a number of *trial* points if they are suitable and inside the area, which should be sampled. The critical part of the algorithm is, where it must be checked if a new point has neighbours or not. If there are no direct neighbours below a distance less than $h(\mathbf{x})$ and if the point is inside the area, it will be accepted as a candidate for the output list. It returns a point set, which has a minimal fill distance, which is proportional to a function $h(\mathbf{x})$. The algorithm is linear, only if the test for existing neighbours can be done also in $O(N)$. Here, a Verlet list can be used efficiently to look up potential neighbours (Verlet, 1967). A spatial adapted sampling pattern can be realized, if the minimal separation distance is varied according to the needed adaption. In the end, this procedure can be used to generate adapted point sets to handle complex geometries. In the subsequent chapter on example calculations an adapted point sampling is used to discretize a curved interface problem.

It is well known, that magnetotelluric simulations can significantly benefit from adapting the discretization exponential to the air-Earth interface (Wannamaker et al., 1985). To

adapt point samplings towards the air-Earth interface, in this thesis the grid stretching formula of Eriksson (1982) is used. If a grid, or in this thesis a point sampling, should be adapted exponentially to an interface at the depth of $z = z_i$, this could be done using

$$z = \begin{cases} z_i \left[(e^{\alpha} - e^{\alpha(1-z/z_i)})/(e^{\alpha} - 1) \right], & \text{for } 0 \leq z \leq z_i, \\ z_i + (1 - z_i) \left[(e^{\alpha(z-z_i)/(1-z_i)} - 1)/(e^{\alpha} - 1) \right], & \text{for } z_i < z < z_{max}. \end{cases} \tag{3.107}$$

The parameter α controls the point spacing towards the interface and can be adapted according to the physical settings. Values between $\alpha = 0.0 \ldots 2.5$ can be commonly used to enhance the accuracy at the interface. The chapter about magnetotelluric example calculations will show a study on how different point spacings affect the accuracy of the modelling study. Using this 'stretching' formula, point samplings as the one pictured in Figure 3.12 can be done, if the sampling distance function $h(\mathbf{x})$ varies according to the Eriksson scaling. The Figure 3.13 displays the adaptivity towards the interface (here at $z = 0$) for various α values, while the total number of points remain the same. Only the spatial position is transformed using the Eriksson function.

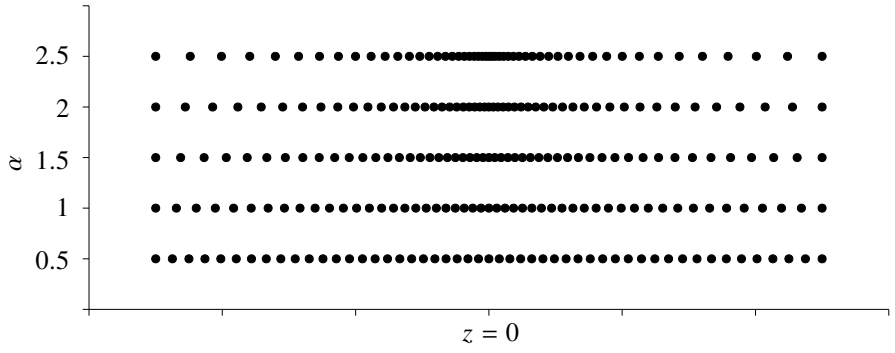

Figure 3.13: Adapted spatial density using the Eriksson function as defined in Equation (3.107) for different α.

3.7.2 Solving the linear system

The bottleneck of every discretization is the solution of the resulting sparse linear system of equations. High accuracy needs either high polynomial order or small-scale discretization. This leads to large-scale sparse linear systems, which needs to be solved. Using two dimensional approximations, the situation can be handled with less effort. A variety of ready-to-use solvers are available and can be used. Here is the question, if this modelling scheme will be used in an inverse algorithm or only as a stand-alone application. If an inverse scheme is involved, a factorization of the system matrix is indispensable. The inverse process needs to calculate the Jacobian matrix of the model parameter. This involves solving many algebraic systems assembled from the sparse matrix of the forward algorithm. The benefit of using a factorization is the rapid solution of algebraic systems with different right-hand sides. Once the factorization is computed, the solution can be calculated directly by forward and backward substitution. In this thesis, the freely available multifrontal solver of Amestoy et al. (2000) is used to solve algebraic systems, which results from a two-dimensional discretization. Also, this solver is used in the inverse scheme to improve the speed of the algorithm by utilizing the factorization of the system matrix.
Generally, the bandwidth of a sparse matrix which results from a meshless discretization, is controlled by the amount of neighbouring points used in the calculation of the approximation coefficients. Using many neighbouring points in the approximation results in many non-zero elements in the sparse matrix, because every neighbour generates one entry in the sparse matrix. The approximation scheme, which is used here in this thesis, generates complex-valued, unsymmetrical, sparse algebraic systems. Two example

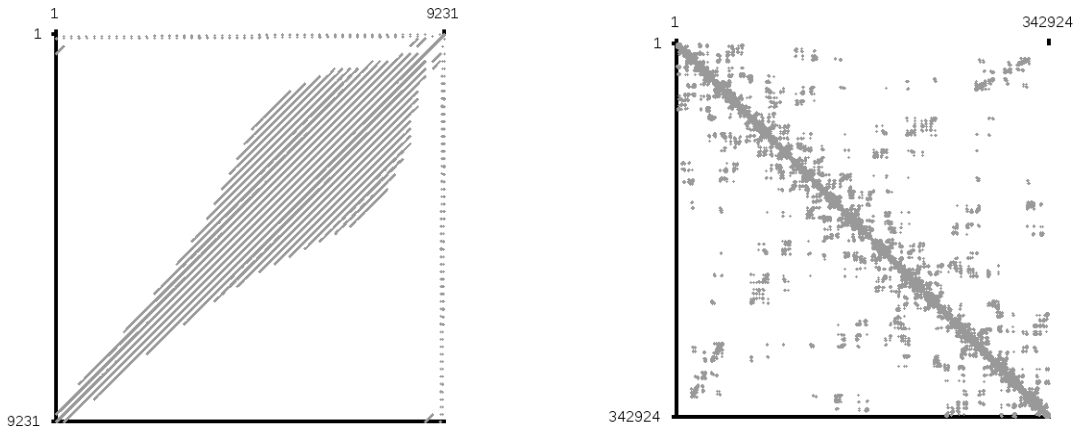

Figure 3.14: Sparsity pattern for the two-dimensional meshless calculation for the model of Schwalenberg and Edwards (2004) displayed in the left picture and the sparsity pattern for the three-dimensional example calculation pictured on the left right-side.

sparsity pattern of the sparse matrices can be seen in Figure 3.14. One for the meshless calculations using the model of Schwalenberg and Edwards (2004), and an adapted point sampling and a sparsity pattern for the system matrix resulting from the discretization of the three-dimensional conductivity structure. As is can be clearly seen in the pattern for the two-dimensional case, the point sampling is adapted at the interface. This results in more neighbours and therefore in more entries per row. Even if the pattern look symmetrical, it is only structural symmetric. This results from the numbering of the points in the calculations and from the neighbouring search procedure. In the sparsity pattern for the three-dimensional case, it can be seen that a three dimensional discretization leads to a more scattered non-zero pattern in the sparse matrix. Here, the matrix is highly diagonal dominant as in the two-dimensional case, but with many off-diagonal entries. Compared to the two-dimensional case, the overall degrees of freedom in the three-dimensional calculations is determined by the amount of nodes times four, because for every node four equations must be approximated. Also, the approximation needs at least ten times more neighbours as in the two-dimensional case. For the example, sparsity pattern given in the Figure 3.14 the number of non-zero elements is more then 100^6. In the end, the number of non-zero elements is significant higher compared to a two-dimensional discretization scheme. The algebraic system of the three-dimensional discretization will be solved, using a multilevel incomplete LU decomposition as preconditioner in combination with an iterative GMRES solver as described by Bollhöfer and Saad (2006).
The overall computations can be coarsely categorized into four different stages. These different components can be seen in Figure 3.8. All these parts of the computation, need different amount of time to process. An overview of these times are given in Figure

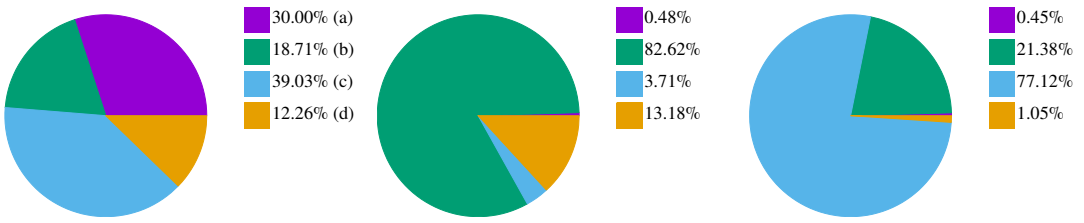

Figure 3.15: Timing diagrams for three different meshless calculations. All values are normalized onto the whole computational time. Two-dimensional calculation times left chart, two-dimensional calculation times from Wittke and Tezkan (2014) for a comparable amount of points middle chart and three-dimensional calculation times, right chart. The percentaged values are for the pre-processing (a), the assembling of the sparse matrix (b), the solving time (c) and the post-processing (d). The labelling corresponds to the labelling in Figure 3.8.

3.15. In this figure, the percentaged times of each computational stage is displayed for a two-dimensional meshless calculation with approximately ten thousand points, values for

the implementations of Wittke and Tezkan (2014) and values for the three-dimensional meshless case from this thesis. It is obvious, by comparing the implementation presented in this thesis and the one given by Wittke and Tezkan (2014), that the time used to assemble the sparse matrix can be significantly reduced by using the direct meshless formulations presented in this thesis. The time spend to solve the algebric system is nearly equal when compared to the overall run-time. The post processing is also equal. The significant differences in the pre processing is due to different point sampling strategies and different point definitions inside the algorithm. By comparing the two-dimensional run-times to the three-dimensional case, it can be seen that in the three-dimensional case the overall process is dominated by solving the sparse system. This is due to the huge amount of non-zero elements, which slows down the computation of the preconditioner. The overall run-times of the two-dimensional computations are comparable to run-times of finite element implementations. Using the three-dimensional scheme the overall run-time is about one minute for approximately 10^3 points and can be increase up to twenty minutes using approximately 10^5 points.

3.8 Magnetotelluric example calculations

This section will present some magnetotelluric example calculations to verify the correctness of the algorithm. Also, the meshless scheme will be used to calculate magnetotelluric responses for some selected Earth models published in the literature. First, convergence results for the two-dimensional algorithms are presented to investigate the behaviour of the two-dimensional implementations in terms of error. Afterwards, two specific Earth models will be used to investigate some selected properties of the two-dimensional modelling scheme. In the end of this section a three-dimensional modelling example will be presented.

3.8.1 Two-dimensional example calculations - convergence results

The quality of the proposed meshless algorithms can be mainly described by the accuracy of its solution. To investigate the behaviour of this accuracy, theoretical assumptions have been made in the Chapter 3.2.2. From the error bounds presented there it is obvious, that there should be an decrease in the error if the fill distance is reduced or if the polynomial degree is increased. Using the theoretical error bounds to describe the behaviour of the numerical calculations, two aspects are important. To compare the results of the general error bound given in Theorem 3.1 and convergence rates from Franke-Börner (2013) with

the numerical computations, the errors in the convergence study are given with respect to a point-wise $L_2(\Omega)$ norm in a relative root mean square sense and $L_\infty(\Omega)$ norm defined by

$$||e||_{rms} = \left(\frac{\sum_{i \in X} (\hat{u}_i - u_i)^2}{N \sum_{i \in X} u_i^2} \right)^{1/2}, \tag{3.108}$$

and

$$||e||_\infty = \max_{i \in X} |\hat{u}_i - u_i|. \tag{3.109}$$

Whereas the computed solution is denoted by $\hat{u}$ and the exact solution is u, given by an analytical expression (Wait, 1953). For the two-dimensional magnetotelluric example, in the TE-mode u will be $u = E_x$ and in the TM-mode $u = H_x$. Using a strong collocation meshless scheme should give approximately linear convergence for a polynomial degree of $m = 2$ and third order convergence by using $m = 4$, if the underlying partial differential system has a smooth solution. As explained in the previous chapter, the conductivity is piecewise constant and the differential equations belong to the class of elliptic interface problems. This will lower the convergence and optimal rates as in a smooth case will not be achieved. Because of the strong interface between Earth and air, at which the conductivity jumps several decades. Here, convergence studies are presented in which both parameters, the point distance and polynomial degree, are varied. For two polynomial degrees $m = 2$ and $m = 4$ and regular $h_{X,\Omega}$-refinement the convergence of different meshless formulations for a homogeneous half-space model will be presented. The results of the errors will be given in dependence to the overall degrees of freedom of the whole discretization. To classify the results from these studies, comparable convergence estimates for the finite element method taken from Franke-Börner (2013) are given. Making all numerical convergence studies comparable, one reference Earth model, a homogeneous half-space with a $\sigma = 0.01\mathrm{S\,m}^{-1}$ Earth conductivity, was used together with a frequency of $f = 0.1\mathrm{Hz}$ and a regular equidistant point spacing. This model was also used in convergence studies by Franke-Börner (2013). First, an implementation only using the material averaging from Chapter 3.6 will be presented. In this example only pure point collocation will be used and this needs to compute the coefficients by Equation (3.77) in combination with the functionals presented in Equations (3.80) and (3.81). Figure 3.16 displays the convergence of this implementation for both modes in comparison with convergence results from Franke-Börner (2013). The errors in both norms are plotted for two polynomial degrees, as well as the convergence result from the FEM calculations. It can be seen from the left graph in figure 3.16 that using the TE-mode calculations the error can be decreased, while in the TM-mode no convergence is achieved. Also no better convergence is achieved when using an increased polynomial

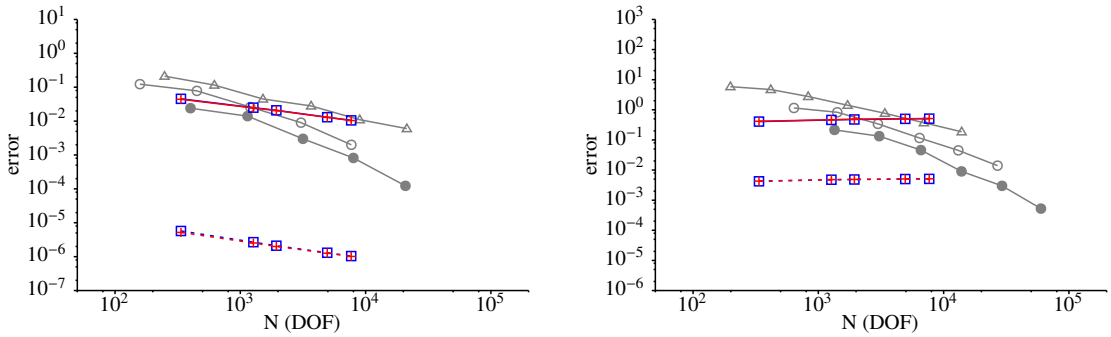

Figure 3.16: Convergence of the meshless algorithm using the magnetotelluric half-space example only with material averaging, regular points. The left figure displays the TE-mode and the right figure the TM-mode calculations. The solid lines show the error for $m = 2$ and for $m = 4$ using the L_2 norm, the dashed lines the error in L_∞. For comparison, the FEM results from Franke-Börner (2013) with $p = 1$, $p = 2$ and $p = 3$ are also plotted in both graphs.

degree. This behaviour is predictable, because in the calculation of the TM-mode, no interface condition is considered. Here, the averaging will not be applicable to solve this interface problem successfully for the TM-mode. Similar results, if the interface is not explicitly considered, have been reported by Chen et al. (2009) using a radial basis collocation approach for heterogeneous materials. In opposite to a pure collocation

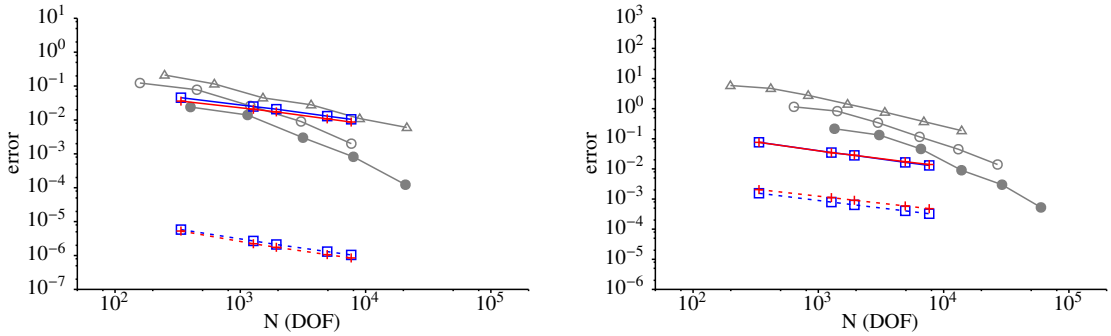

Figure 3.17: Convergence of the staggered meshless algorithm using the magnetotelluric half space example with material averaging, regular points. The left figure displays the TE-mode and the right figure the TM-mode calculations. The solid lines show the error for $m = 2$ and for $m = 4$ using the L_2 norm, the dashed lines the error in L_∞. For comparison, the FEM results from (Franke-Börner, 2013, Fig. 5.1) with $p = 1$, $p = 2$ and $p = 3$ are also plotted in both graphs.

scheme, the staggered moving least squares algorithm of Trask et al. (2017) is able to handle the interface in both magnetotelluric modes. As Trask et al. (2017) explain, the capability to handle interface problems correctly is the similarity of the scheme to compatible discretization methods. Nevertheless, they do not provide convergence results for the staggered scheme using rough or piecewise material parameters. The convergence of the calculations for the magnetotelluric case can be seen in Figure 3.17

using the calculated coefficients from Equation (3.85). In both modes the algorithm converge, but the results from the TE-mode show no better performance than using the plain averaging scheme. In the TM-mode, convergence is achieved and the overall error is almost one decade less than in the TE-mode. Also, the maximum error in both magnetotelluric modes is clearly less than the relative rms error. Nevertheless, an increase in the polynomial degree do not enhance the quality of the solutions. To overcome the

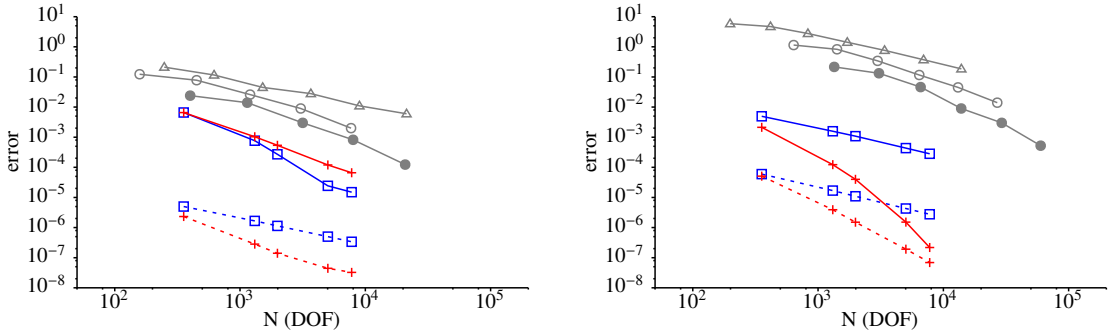

Figure 3.18: Convergence of the meshless algorithm using the magnetotelluric half-space example with double nodes, regular points. The left figure displays the TE-mode and the right figure the TM-mode calculations. The solid lines show the error for $m = 2$ and for $m = 4$ using the L_2 norm, the dashed lines the error in L_∞. For comparison, the FEM results from (Franke-Börner, 2013, Fig. 5.1) with $p = 1$, $p = 2$ and $p = 3$ are also plotted in both graphs.

poor convergence rate, provided by the collocation and staggering methods in combination with averaging, the 'double node' approach was implemented to handle the interface conditions (3.99) exactly. Now, the two methods using plain averaging will be tested again, using the explicit interface descriptions. As displayed in Figure 3.18, it is obvious that the convergence rates for both magnetotelluric modes can be improved. In contrast to the plain averaging, the convergence for the calculations using a polynomial degree of $m = 2$ are comparable with the FEM convergence rates using second order polynomials in the TE-mode and comparable to fist order polynomials in the TM-mode. Unfortunately in the TE-mode calculations the convergence for the rms error using fourth degree polynomials is not improved in comparison using a second order polynomial degree. In opposite to the TE-mode calculations, the convergence of the TM-mode can be improved by using polynomials with higher degrees. Here, the convergence rate for the fourth order polynomial calculations can be significantly increased. By using the staggered collocation scheme, no improvement in the convergence rate should be expected, because the averaging here only works on points with equal conductivity. As seen in Figure 3.19, similar convergence rates as using the plain collocation scheme can be observed. In the TM-mode calculation using fourth order polynomials the overall error is increased, but the convergence rate could be preserved. Nevertheless, the staggered scheme will

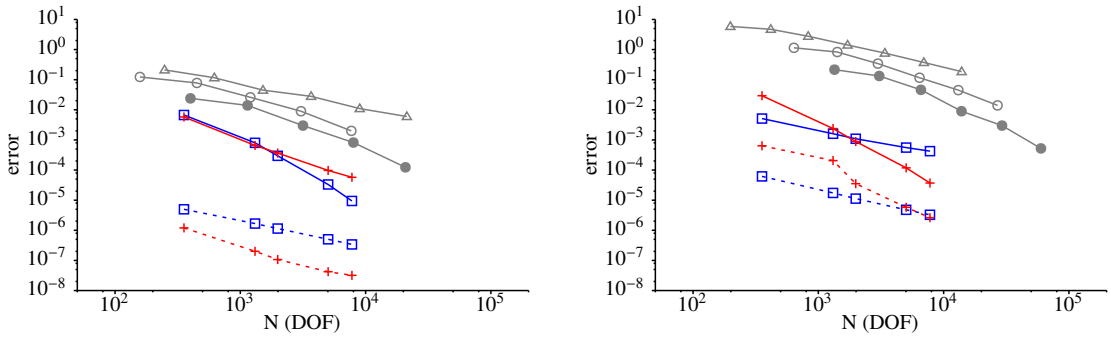

Figure 3.19: Convergence of the staggered meshless algorithm using the magnetotelluric half-space example with double nodes, regular points. The left figure displays the TE-mode and the right figure the TM-mode calculations. The solid lines show the error for $m = 2$ and for $m = 4$ using the L_2 norm, the dashed lines the error in L_∞. For comparison, the FEM results from (Franke-Börner, 2013, Fig. 5.1) with $p = 1$, $p = 2$ and $p = 3$ are also plotted in both graphs.

be used if conductivity contrasts are present inside Earth. The last convergence test is

	av-only	av-stagg	dn-only	dn-stagg	dn-stagg pd
TM $m = 4$	bounded (-0.07)	0.56	2.21	2.00	2.00
TM $m = 2$	bounded (-0.06)	0.55	0.88	0.87	0.72
TE $m = 4$	0.45	0.46	1.51	1.80	0.95
TE $m = 2$	0.45	0.43	1.43	1.63	1.65

Table 3.4: Overview of the convergence rates of the rms error in the point-wise $L_2(\Omega)$ norm, displayed in the Figures 3.16 to 3.20. The row labelling is: 'av-only' denotes only material averaging, 'av-stagg' denotes the staggered scheme with material averaging, 'dn-only' denotes a plain collocation scheme with the 'double node' approach, 'dn-stagg' is the staggered scheme with the 'double node' approach and 'dn-stagg pd' is the same algorithm as before, using a Poisson disk sampling pattern.

done by using the staggered scheme with the 'double node' approach and the Poisson point sampling. Here, a point sampling was generated, using the described Poission disk sampling method from the previous chapter. The result is displayed in Figure 3.20. As expected, only slight differences compared to the regular point sampling can be encountered. For all convergence calculations, the Table 3.4 summarizes all rates for the rms error.

As it is well known, that refining the discretization towards the air-Earth interface will improve the solution and decrease the overall error, some studies will be presented to investigate these effects. As noted in the previous chapter about point sampling, an adapted sampling near the interface can be done using the Eriksson function (3.107). To study the effect of adaptation near the air-Earth interface, the homogeneous half-space

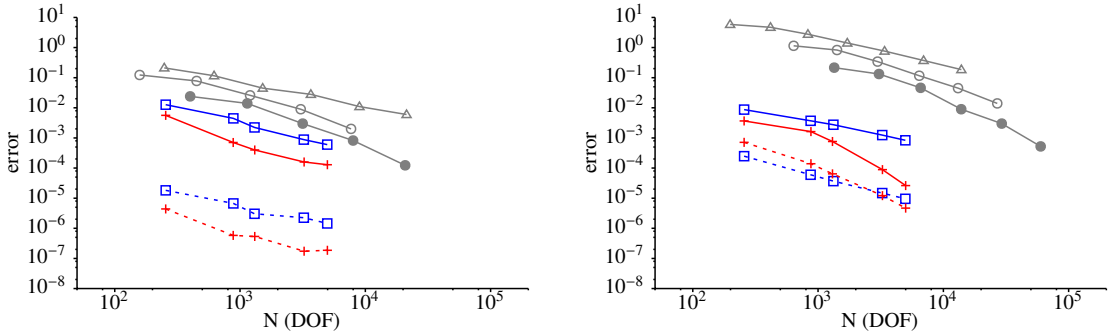

Figure 3.20: Convergence of the staggered meshless algorithm using the magnetotelluric half space example with double nodes, Poisson disk sampling points. The left figure displays the TE-mode and the right figure the TM-mode calculations. The solid lines show the error for $m = 2$ and for $m = 4$ using the L_2 norm, the dashed lines the error in L_∞. For comparison, the FEM results from (Franke-Börner, 2013, Fig. 5.1) with $p = 1$, $p = 2$ and $p = 3$ are also plotted in both graphs.

model applied in the convergence studies was used in combination with a spatially adapted point sampling. Different values for the parameter α in Equation (3.107) have been tested and a increasing adaptation towards the interface should reduce the overall error. The result from this study can be seen in Figure 3.21. Using different point samplings with an initial regular distribution and then increasing the parameter α lead to smaller overall errors. The calculations have been done with a second order polynomial degree and a fixed frequency with the same value as in the convergence study. For the TE-mode results it can be seen, that decreasing the regular point sampling distance will lead to a smaller error as well as increasing α. Here the point set can be optimized according to the magnetotelluric skin depth as explained in Wannamaker et al. (1985). For the TM-mode this procedure is also possible, as the right panel in Figure 3.21 suggests, but using an initial small regular point sampling can reverse the effect of reducing the error.

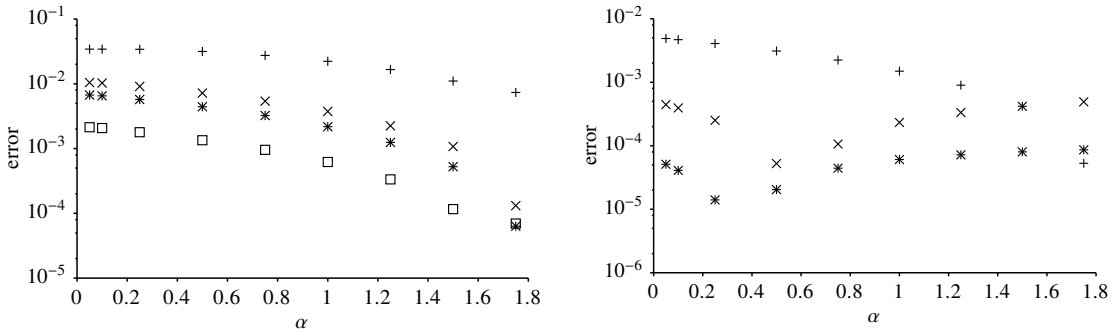

Figure 3.21: Effect of an exponential point distribution by changing α. The left figure displays the TE-mode and the right figure the TM-mode calculations. The different point graphs show the L_2 error versus α for the regular point separation of $10000m$ +, $5000m$ ×, $2500m$ ✳ and $2000m$ □.

3.8.2 Two-dimensional example calculations - Earth models

After studying the convergence of the meshless algorithms, some more complex examples will be given to test the computational scheme. Upon now, magnetotelluric parameters as the apparent resistivity and phase are used to display the results of the computations. All examples will be calculated with the staggered scheme using conductivity averaging and a polynomial degree of $m = 2$. Exceptions to this will be noted in the text. For all model studies using a regular equidistant point sampling, this point sampling will not be shown here. If a model has a special, adapted point sampling, it will be displayed in the Appendix A.2. Here, these parameters are derived from Equations (2.91) and (2.92).

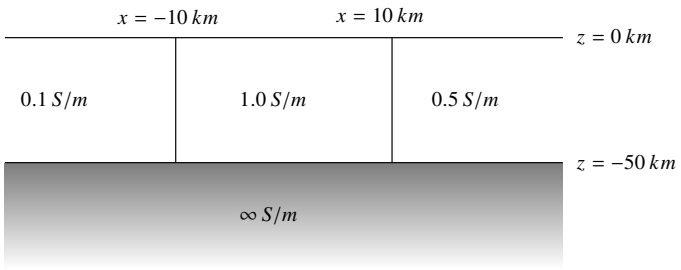

Figure 3.22: Schematic drawing of the model from Weaver et al. (1986) used in the calculations below.

Since these parameters need two fields in each mode, the field which was not given by the modelling scheme will be calculated according Equation (2.63b) for the TE-mode and with the help of Equation (2.64b). In this section the choice of example calculations is according to analytical results or comparable numerical values published in the literature. The first example uses a conductivity model given by Weaver et al. (1985, 1986). For this conductivity model analytical results are given and the meshless calculations will be compared with them. Figure 3.22 displays the model, which consists of three different regions of conductivities with horizontal contrasts of 1 : 10 and 2 : 1. To compare the results properly with the values from the literature, regular spaced point samplings will be used. The first meshless calculation is done for the TE-mode using a frequency of $f = 0.033$Hz. The electrical field E_x is smooth across the conductivity boundaries. This can be also seen in the apparent resistivity and phase. Figure 3.23 shows the result of the meshless computations along a profile. Both results, the one for the apparent resistivity and for the phase are in a good agreement with the analytical results. After comparing the values for the TE-mode, results for the TM-mode will be given. This is the first

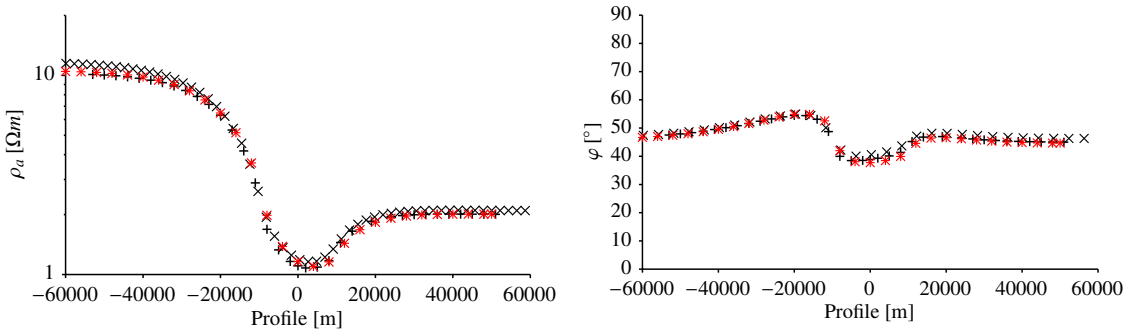

Figure 3.23: Example calculations for the model of Weaver et al. (1986). The left figure displays the apparent resistivity, the right figure the phase. The figures display meshless calculations ✱, analytical results from Weaver et al. (1986) + and a FEM caclulation ×.

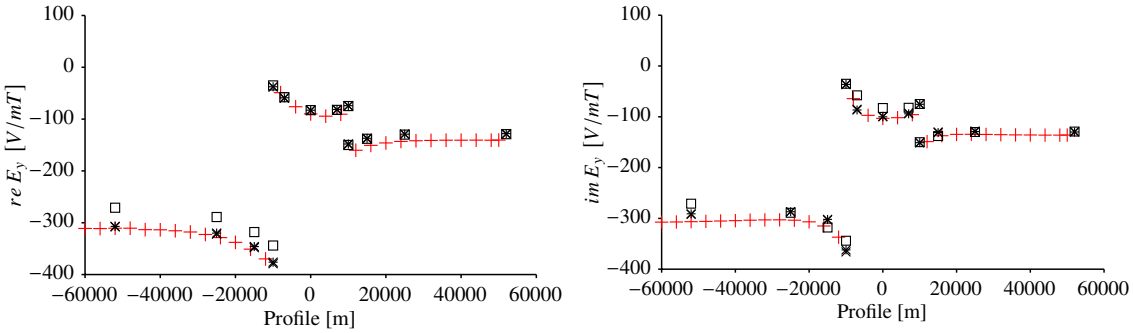

Figure 3.24: Example calculations for the model of Weaver et al. (1985). The left figure displays the imaginary part of the electrical field, the right figure the imaginary part. The figures display meshless calculations +, analytical results from Weaver et al. (1985) + and a FEM caclulation × from Kisak and Silvester (1975) and FD calculation □ from Brewitt-Taylor and Weaver (1976).

serious test for the meshless algorithm, because the electrical field E_y jumps according to the conductivity structure. In this example the staggered meshless scheme in combination with the conductivity averaging is used. To start, field values will be given for the electrical field E_y and Figure 3.24 displays the results. From this Figure, it can be clearly seen, that the electrical field is discontinuous at the conductivity contrasts. Nevertheless, Figure 3.24 shows the good agreement of the meshless results in comparison to the analytical solution and the other values computed by some classical numerical schemes. This result generated by the staggered meshless scheme with conductivity averaging shows the correctness of the algorithm and its ability to handle conductivity contrasts accurately. Since the electrical field is discontinuous in the TM-mode, the apparent resistivity and phase should also have jumps at the conductivity contrasts. In the next example, the apparent resistivities and phase values are compared to the analytical ones. Also, the effect of the averaging is demonstrated. The result is displayed in Figure 3.25. Here, it can be seen that the combination of harmonic and arithmetic averaging lead

to correct results. Using only arithmetic averaging as suggested by Trask et al. (2017) can not handle conductivity contrasts in the TM mode right. Nevertheless, when using the right averaging the results of the meshless scheme are in a good agreement with the analytical values given by Weaver et al. (1985). After having confirmed the accuracy

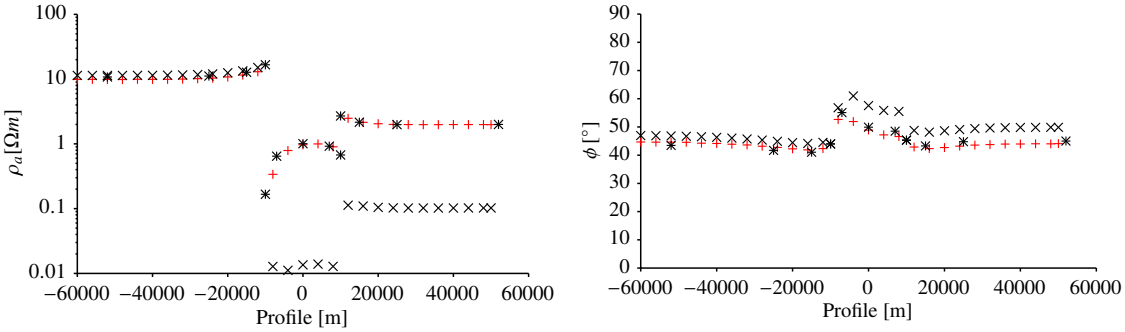

Figure 3.25: Example calculations for the model of Weaver et al. (1986) with different averaging. The left figure displays the apparent resistivity, the right figure the phase. The figures display meshless calculations using the right averaging + and false averaging ×, as well as the analytical ✳ solution from Weaver et al. (1986)

of the meshless schemes with respect to the simulated fields and capabilities to handle conductivity contrasts, an example should be given demonstrating the ability to handle complex geometries. Schwalenberg and Edwards (2004) gives semi-analytical results for magnetotelluric fields over an Earth with topography. Here, their results will be compared to meshless simulations using the same conductivity model. This conductivity model is a homogeneous half-space, but the Earth surface is described by a sinusoidal interface as displayed by Figure 3.26. This sinusoidal interface is modeled with a wavelength of $\lambda = 1000\text{m}$ and an Earth conductivity of $\sigma = 0.01\text{S}\,\text{m}^{-1}$. Two versions of this model should be used in the calculations. The first one has an amplitude of $\triangle = 50\text{m}$ and the topography of the second one has an amplitude of $\triangle = 100\text{m}$. Only the one model with an amplitude of 50m is displayed in Figure 3.26. By using this kind of model, topographic distortion should occur in the magnetotelluric fields. Nevertheless, the TM-mode will be more distorted than the fields of the electrical mode. Here, the model parameters for the simulation are given as the parameters Schwalenberg and Edwards (2004) used in their 'standard model'. It consists of a sinusoidal homogeneous half-space with a conductivity of $\sigma = 0.01\text{S}\,\text{m}^{-1}$ beneath an air layer with a conductivity of $\sigma = 10.0^{-10}\text{S}\,\text{m}^{-1}$. A frequency of $f = 100.0\text{Hz}$ was used and the profile covers a length of 2000m. The apparent resistivity and phase will be calculated every 50m along the profile. The frequency was increased in comparison to the calculations of Schwalenberg and Edwards (2004), because the TE-mode will not be effected by the topography using low frequencies. This was also noted by Franke et al. (2007). Now, a meshless calculation will be presented

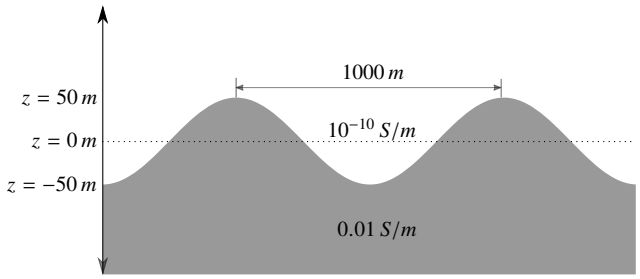

Figure 3.26: Schematic drawing of the model from Schwalenberg and Edwards (2004), used in the calculations below with an amplitude of $\triangle = 50$m.

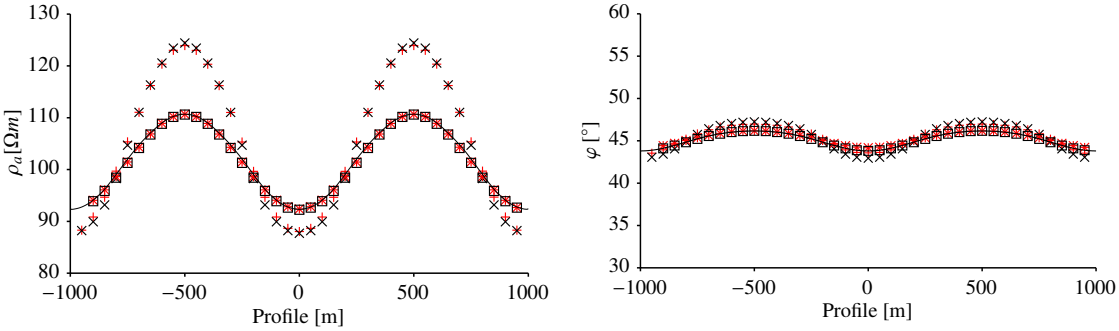

Figure 3.27: TE-mode example calculations for the model of Schwalenberg and Edwards (2004) with a regular point distribution. The left figure displays the apparent resistivity, the right figure the phase. The figures display meshless calculations ✱ *(*$\triangle = 50m$*) and* + *(*$\triangle = 100m$*). Also the values from the analytic calculations* □ *(*$\triangle = 50m$*) and* × *(*$\triangle = 100m$*) are plotted, as well as the FEM results for (*$\triangle = 50m$*) as a black solid line .*

using an adapted point sampling to handle the sinusoidal interface. This sampling was created by increasingly adapting the amplitude of the sinusoidal function from zero to the final amplitude. A sampling distance of $h_{X,\Omega} = 50$m was used in this examples. The whole point sampling for the model can be seen in Figure A.50 in the Appendix A.2. Using this point sampling, the TE-mode solution for two sinusoidal interfaces are calculated using the staggered scheme with averaging. The results can be seen in Figure 3.27, where the meshless calculation and the analytical results are plotted. For both amplitudes the meshless results, apparent resistivities and phases, are in a good agreement to the analytical calculated values. Since for the TE-mode the resistivities and phases only vary moderate due to the topographic distortion, in the TM-mode higher deviations can be expected. As seen in the Figure 3.28, the apparent resistivities for both amplitudes are in a good agreement with the analytical results. Only in the peak values around profile meter zero, deviations between the meshless results and the analytical solution can be detected. This effect is more visible in the apparent resistivity than in

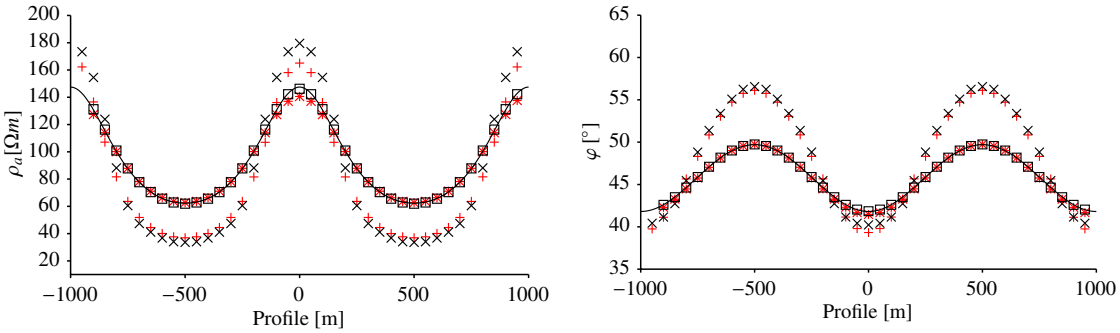

Figure 3.28: TM-mode example calculations for the model of Schwalenberg and Edwards (2004) with a regular point distribution. The left figure displays the apparent resistivity, the right figure the phase. The figures display meshless calculations ✳ ($\triangle = 50m$) and + ($\triangle = 100m$). Also the values from the analytic calculations □ ($\triangle = 50m$) and × ($\triangle = 100m$) are plotted, as well as the FEM results for ($\triangle = 50m$) as a black solid line .

the values for the phases. As it can be seen from the two Figures 3.27 and 3.28, results

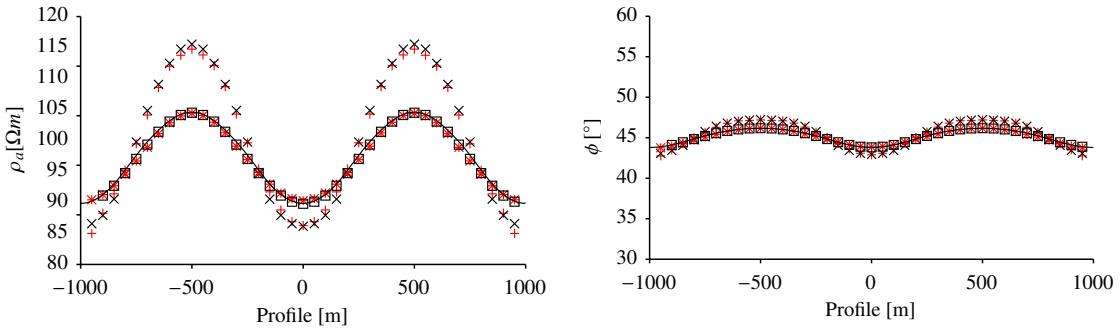

Figure 3.29: TE-mode example calculations for the model of Schwalenberg and Edwards (2004) with an adapted point distribution. The left figure displays the apparent resistivity, the right figure the phase. The figures display meshless calculations + ($\triangle = 50m$). Also the values from the analytic calculations × ($\triangle = 50m$) are plotted, as well as the FEM results for ($\triangle = 50m$) as a black solid line.

from a FEM calculation are included in the graphs as solid black line for the amplitude of $\triangle = 50$m. The adapted mesh for the FEM calculations can be seen in Appendix A.2 in Figure A.55 . Using a second order polynomial degree and the high adapted mesh which results in 24353 degrees of freedom for the system matrix, are slightly better than the meshless solution, which has only 2540 degrees of freedom. To gain more accuracy and to improve the meshless results, the point sampling will be spatially adapted at the sinusoidal interface. The resulting point sampling can be seen in Figure A.51 in the Appendix A.2. Using this adapted point sampling, which has the same amount of points, the meshless solution can be improved. The calculations for the TE-mode can be seen in Figure 3.29. Here, for both sinusoidal amplitudes the meshless accuracy can slightly be improved. While the effect of the improvement is not very noticeable, the results

for the TM-mode could be significant improved. The calculations for the TM-mode, using normal point distribution, can be seen in the Figure 3.28. Observing a deviation

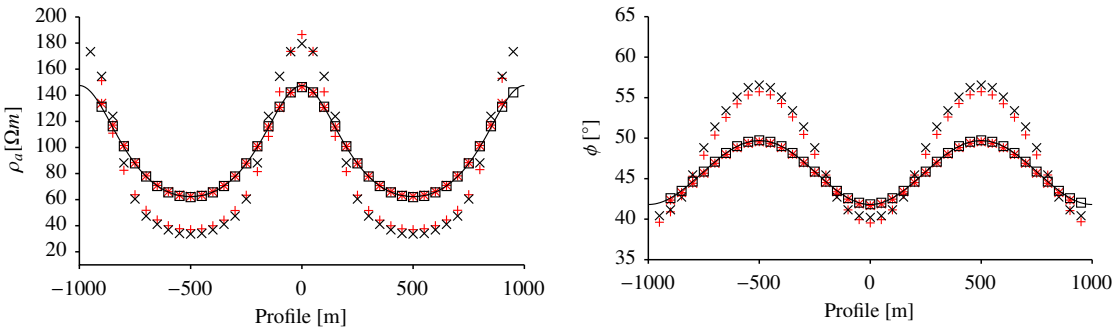

Figure 3.30: TM-mode example calculations for the model of Schwalenberg and Edwards (2004) with an adapted point distribution. The left figure displays the apparent resistivity, the right figure the phase. The figures display meshless calculations ✱ ($\triangle = 50m$) and + ($\triangle = 100m$). Also the values from the analytic calculations □ ($\triangle = 50m$) and × ($\triangle = 100m$) are plotted, as well as the FEM results for ($\triangle = 50m$) as a black solid line .

between the meshless values and the results from the analytical calculations, it can be seen from Figure 3.30 that a spatial adaption towards the sinusoidal interface cures this inaccuracy for the apparent resistivities. Here, an adaptation parameter $\alpha = 1.5$ has been chosen to refine the sampling near the interface. To emphasize the improvement between the results of the normal point sampling and an adapted point sampling, a figure was compiled, which visualize the differences better. Figure 3.31 shows the differences for the two point samplings with a magnification around the peak values. Here it is obvious, that the adapted point set performs better, and the results are more accurate especial for the sinusoidal interface with an amplitude of $\triangle = 50$m.

Studying the results for the model of Schwalenberg and Edwards (2004) it can be said, that the meshless scheme can capture topographic distortions well. Using a regular point sampling, the calculations are almost as accurate as the finite element results. Using a spatially adapted point sampling, the accuracy of the scheme can be raised and the results are accurate as the finite element solution. Comparing the costs of the calculation, it can be stated that the meshless solution only needs one tenth of the degrees of freedom. While the finite element calculations need a highly adapted mesh, the point sampling can be done in a few lines of Fortran code. Here, the simplicity using a unconnected point sampling is beneficial over using a highly adapted computational mesh. As last example, to test the two-dimensional algorithm, the model of Schwalenberg and Edwards (2004) is calculated using a Poisson disk point sampling generated with the methods described in Sub-chapter 3.7. The whole point sampling for the model can be seen in Figure A.52 in the Appendix A.2. The magnetotelluric responses can be seen in Figure 3.32. It can be

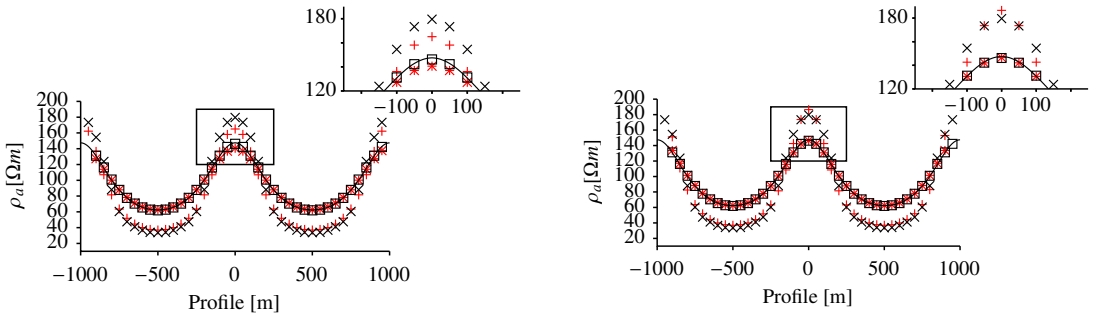

Figure 3.31: TM-mode example calculations for the model of Schwalenberg and Edwards (2004) with a regular point distribution. The left figure displays the apparent resistivity for the normal point sampling, the right figure displays the calculation for the adapted point sampling. The values around the peak at $z = 0$m are magnified in the upper right corner. The figures display meshless calculations ✳ ($\triangle = 50m$) and + ($\triangle = 100m$). Also the values from the analytic calculations □ ($\triangle = 50m$) and × ($\triangle = 100m$) are plotted, as well as the FEM results for ($\triangle = 50m$) as a black solid line .

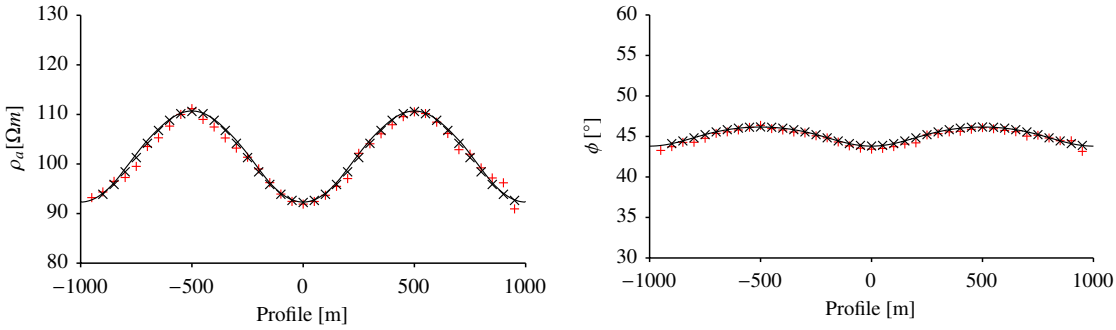

Figure 3.32: TM-mode example calculations for the model of Schwalenberg and Edwards (2004) with a Poisson disk point distribution. The figures display meshless calculations + ($\triangle = 50m$). Also the values from the analytic calculations × ($\triangle = 50m$) are plotted, as well as the FEM results for ($\triangle = 50m$) as a black solid line .

noted, that a unorganized point sampling can be used to calculate the magnetotelluric responses for this model. As seen in Figure 3.32 only slight deviations of the results compared to the analytical calculated values can be recognized. These deviations from the analytical values are due to random distances from the air-Earth interface to the points in Earth or air, due to the random nature of this point sampling method. Nevertheless, convergence of this approximation scheme have been showed before.

3.8.3 Three-dimensional example calculations

In this subsection, example calculations using the three-dimensional potential formulations are given. This calculations are done using the Coulomb gauged version, as described in Sub-section 2.3.3. The implementation was done using a mixed formulation using

a pure collocation scheme with material averaging for the vector potential **A** and a staggered scheme using material averaging for the skalar potential ϕ. Also, the coulomb gauged version of the potential formulation was used here. The meshless algorithm was given in 3.5.5 and here we use second order polynomials $m = 2$ as basis functions. As boundary conditions Neumann boundaries where used at the sides of the model and Dirichlet boundaries are imposed at the top and bottom for all vector potential components A_x, A_y, A_z and for the scalar potential ϕ. For the two magnetotelluric modes (XY, YX) Dirichlet conditions for the vector potential have been adjusted give an incident H_{0x}-Field in the XY-mode and an incident H_{0y}-Field generates a in the YX-mode. This allows to calculate **E** and **B** fields to define an three-dimensional magnetotelluric impedance and calculate the apparent resistivities and phases with Equations (2.93) and (2.94). All calculations are done using a spatially adapted point sampling based on a regular separation distance. The conductivity model which was used is shown in Figure 3.33. It is a conductive prism embedded into a more resistive homogeneous half-space. The prism has the dimension of 6km × 6km × 3km and is buried 3km beneath the surface. Here magnetoelluric responses have been calculated along a profile which pass the

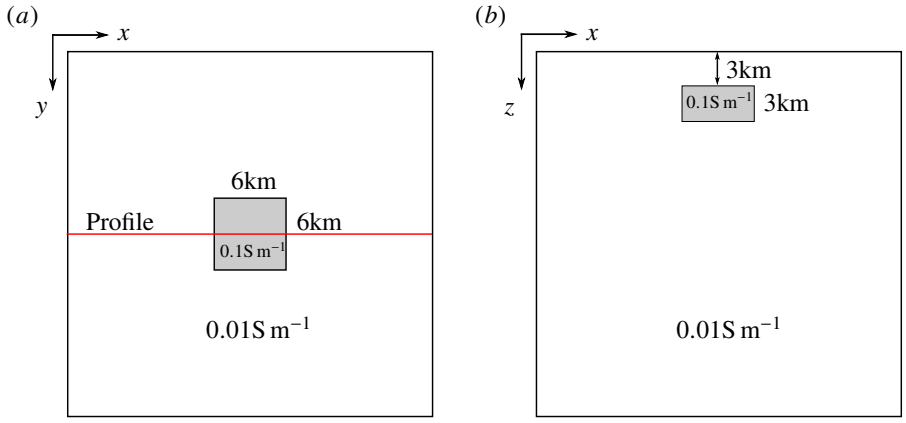

Figure 3.33: Conductivity model for the three-dimensional calculations. A conductive prism with $0.1\,\mathrm{S\,m^{-1}}$ *embedded into a homogeneous half-space with a conductivity of* $0.01\,\mathrm{S\,m^{-1}}$. *(a) Map-view, showing the xy-plane. The measurement profile is drawn in red. (b) Side-view showing the depth and height od the conductive prism.*

middle of the conductive prism at the Earths surface into the x-direction. The profile is marked in red in Figure 3.33 (*a*), which shows a sketch if it. For four different frequencies (0.3Hz □ , 0.1Hz ✱ , 1.0Hz × 3.0Hz +) and both polarizations (XY, YX), apparent resistivities and phases have been computed with the meshless algorithm. Here, these results will be compared with numerical results from the three-dimensional finite differences implementations described in Mackie et al. (1994). The meshless calculations

have been done using a spatially adapted point sampling with an value of $\alpha = 2.0$. By comparing Figure 3.13, the adaptivity around $z = 0$ can be seen.
The results for the XY-mode are displayed in Figure 3.34 and Figure 3.35. The results for the YX-mode can be seen in Figure 3.36 and Figure 3.37. For every solution, the reference results from the algorithm of Mackie et al. (1994) is plotted accordingly. At it can be

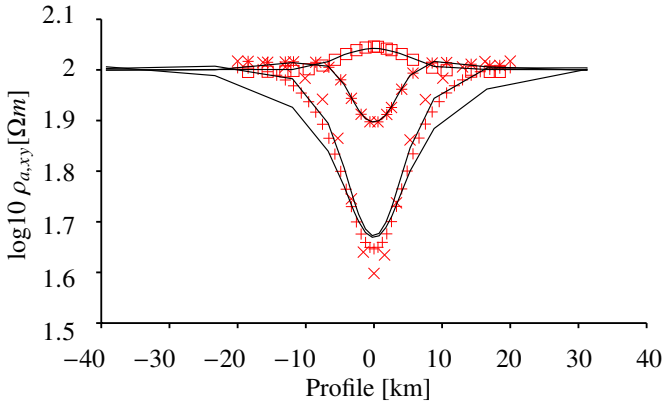

Figure 3.34: Three-dimensional example calculations results for the buried prism model. The figure displays the apparent resistivity for the xy-mode. Meshless calculations using the frequencies 0.3Hz □, 0.1Hz ✱, 1.0Hz × 3.0Hz + *in red, the finite difference solutions in black.*

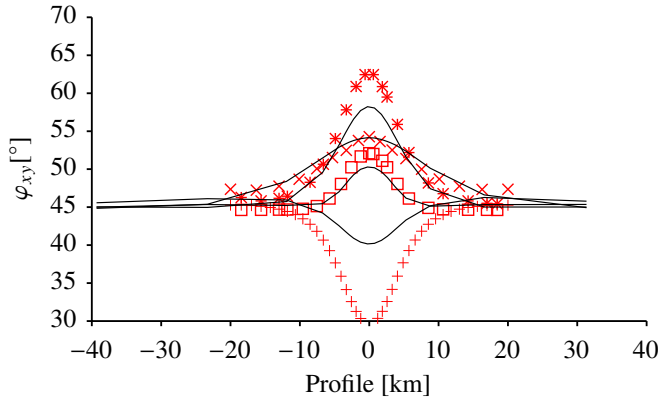

Figure 3.35: Three-dimensional example calculations results for the buried prism model. The figure displays the phase for the xy-mode. Meshless calculations using the frequencies 0.3Hz □, 0.1Hz ✱, 1.0Hz × 3.0Hz + *in red, the finite difference solutions in black.*

seen in Figure 3.34, the values for the last three frequencies are in a good agreement to the finite difference solutions, while lowering the frequency deviations between booth algorithms occur. The meshless algorithm overestimates the apparent resistivities for the frequency of 0.1Hz. Here, also the phases differ significantly. This can be seen in Figure 3.35. Nevertheless, the values show a same behavior, compared to the solution of Mackie et al. (1994). Crucial to gain the correct values for the three-dimensional meshless

results is the right point sampling. For different adapted samplings the three-dimensional algorithm is more sensitive to point distances at the interface, where the magnetotelluric transfer functions will be calculated. In comparison to the results of the XY-mode, the

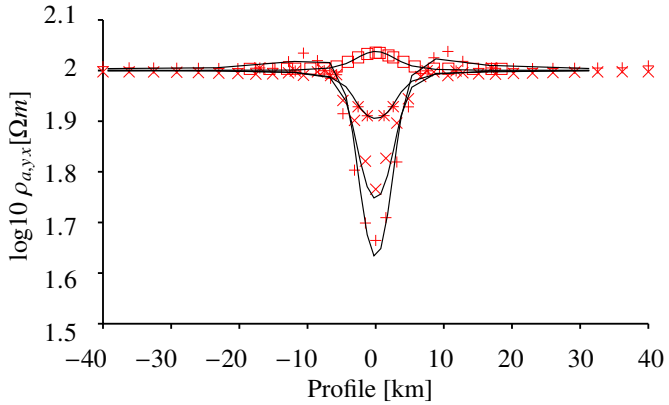

Figure 3.36: Three-dimensional example calculations results for the buried prism model. The figure displays the apparent resistivity for the yx-mode. Meshless calculations using the frequencies 0.3Hz □, 0.1Hz ✱, 1.0Hz × 3.0Hz + *in red, the finite difference solutions in black.*

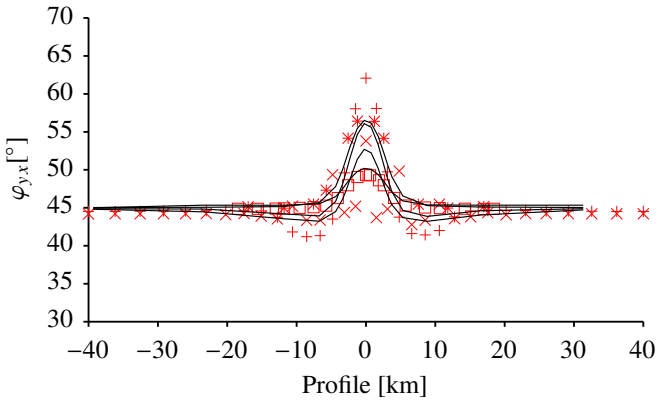

Figure 3.37: Three-dimensional example calculations results for the buried prism model. The figure displays the phase for the yx-mode. Meshless calculations using the frequencies 0.3Hz □, 0.1Hz ✱, 1.0Hz × 3.0Hz + *in red, the finite difference solutions in black.*

meshless algorithm for the YX-mode perform better. Here the results, which can be seen in Figure 3.36 and Figure 3.37, are in a better agreement to the finite differences values calculated by the algorithm of Mackie et al. (1994). Slight differences in the apparent resistivity can be seen in Figure 3.36. Also in the phase, which is displayed in Figure 3.37 performs reasonable well. The crucial part of this computations for the YX-mode is the conductivity contrast in the profile direction. As a consequence the skalar potential ϕ will rapidly change at the conductivity interface. As a consequence this generates a rapidly changing galvanic part in the electrical field and therefore a more narrow magnetotelluric

response. Comparing both modes, this behavior can be seen. Also, by comparing the values of the YX-mode, it can be presumed that the generation of the galvanic part is described correct in the meshless potential formulation.

3.9 Summary and Conclusions

In this chapter, meshless formulations for approximating Maxwell's equations have been developed and tested. After an introduction about general meshless computational methods, a method called generalized moving least squares was introduced. This technique can be applied on general, unstructured point sets to approximate linear target functionals from some functional data sampled at the point set. These linear target functionals can be derivatives, integral formulation or plain function evaluations. Having this numerical framework at hand, special approximation schemes can be constructed. Here, a formulation for the divergence operator was presented using a staggered meshless scheme, which is able to handle material contrasts and non-smooth solutions of the underlying partial differential equations. After presenting the main approximation schemes, error bounds are cited from the literature. They can give a preliminary error estimation in terms of the point separation distance and polynomial degree. As the error theory predict, stability and consistence leads to the convergence of the approximation scheme, here convergence of the formulations have been numerical assured. The method of a direct discretization of a partial differential equation was discussed and combining it with the generalized approximation gives various discretization schemes, which can be applied to simulate a magnetotelluric experiment. In this thesis a strong collocation scheme is mainly used. Nevertheless, a weak formulation was presented, but it was not used in this thesis. The reason is the overall simplicity of the collocation scheme compared to the weak formulation. Even if using the direct approximation, this weak scheme can be simplified, but the overhead of performing the integration leads to choose the point collocation scheme. Formulations for the two and three-dimensional magnetotelluric problems have been given, whereas the two-dimensional formulation split in two schemes. Here, one for the TE-mode and one for the TM-mode are needed to simulate the electromagnetic fields properly. The implementation for the staggered scheme was given in addition to a plain point collocation method. Here, a material averaging can be included to handle spatial variable conductivities and interfaces.
Thanks to the potential formulation for the three-dimensional partial differential system, several parts developed for the two-dimensional scheme can be reused. An important

aspect is the correct consideration of interface descriptions. While the fields occurring in the TE-mode are smooth all over the domain, for the TM-mode the fields behave different. Here, the computational scheme has to take care of interface conditions at jumps in the conductivity. Using an average scheme in the numerical formulation, a combination of harmonic and arithmetic averaging produces the most accurate results. The performance of the numerical scheme can be increased if the interface between Earth and air will be described by a 'double node' approach. Here, the points on the interface will be doubled and constrains for the fields can be imposed on each layer separately. This improves the overall solution and enhance the convergence of the numerical scheme, but the degrees of freedom will be increased. Using this approach only for the air-Earth interface is reasonable, because at this interface the steepest jump in the conductivity appears.

In the last section of this chapter magnetotelluric example calculations are given. Convergence results have been given first and example simulations for Earth models from the literature follow. In the part in which the convergence of the numerical schemes is tested several observations can be made. First, a second order accuracy scheme can be provided to solve the magnetotelluric problem. The best performing formulations in terms of convergence are the pure point collocation and the staggered schemes using material averaging and the 'double node' approach. Second, by only using these schemes with averaging, low convergence can be achieved and also for the Poisson disk sampling the algorithms are convergent in the same way as for the regular point samplings. The presence of the interface interferer the meshless schemes to gain full convergence, as predicted before in the theory part. Nevertheless, modifying the numerical schemes this disadvantage can be compensated.

Some magnetotelluric example calculations from the literature have been presented with comparable meshless results. Here, the fist example was the three-segment model given by Weaver et al. (1985, 1986). This model includes three adjacent conductive parts on top of an infinitely conductive basement. For both, the TE-mode and the TM-mode, analytical solutions are available and the meshless algorithm have been tested against them. The case where the electrical currents are perpendicular to the conductive interfaces are the most critical. Also here, the meshless scheme provides accurate solutions to this kind of problems. Important to use a right averaging scheme, to gain the best performance of the meshless algorithm. The second magnetotelluric example was given by a model of Schwalenberg and Edwards (2004), where topographic distortion effects the fields at the Earth interface. This model, described by a sinusoidal interface is tailored for using a meshless method and as the results suggest, the meshless scheme outperforms the finite element solution. Here, with less then a tenth of degrees of freedoms the accuracy of

both numerical schemes are comparable. With a spatially adapted point sampling the accuracy can be increased.
Beside two-dimensional examples, three-dimensional meshless example calculations are given and compared to the finite differences algorithm of Mackie et al. (1994). These calculations show a good agreement compared to the results calculated by a finite differences algorithm. Nevertheless, even if slight deviations occur the correctness of the algorithm could be proved.

Meshless inversion of magnetotelluric data

This chapter is devoted to the development of a meshless magnetotelluric inversion scheme. By interpreting geophysical data, an Earth model is calculated during an inversion. In contrast to the previous chapter, in which a conductivity structure was given and the numerical procedure must calculate the electromagnetic fields according this structure, is the task to calculate a conductivity distribution with the help of measured data. The process, in which the conductivity structure is reconstructed on the basis of measured data, is called an *inversion*. A general overview about geophysical inverse theory is given, for example, in the books by Menke (1984), Zhdanov (2002) or Aster et al. (2005).

Here in this chapter, a two-dimensional meshless inversion algorithm is proposed, which can handle magnetotelluric data from the two magnetotelluric modes. At the beginning, a general introduction is given on the basic theory of geophysical inversion. Due to the nature of the magnetotelluric experiment, the problem is ill-posed and needs a regularization to constrain the solution to a reasonable set of Earth models. Here, Tikhonov regularization yields to a regularized parametric functional which has to be minimized. In magnetotellurics, this results in a well-posed nonlinear optimization problem. For a proper minimization of the Tikhonov functional several methods are available. Here, a damped Gauss-Newton method in combination with a least squares solver will be used. Nevertheless, this needs to calculate the Jacobian matrix using the meshless framework. It turns out, that using the proposed meshless schemes the calculations for the Jacobian matrix are unstable and no reasonable results for the TM-mode can be calculated. Therefore, the actual implementation only inverts magnetotelluric data from the TE-mode successfully. But to improve these calculations and adapt it to the meshless setting a method based on electromagnetic reciprocity is applied, in which the discretization from the froward modelling can be reused. In addition, by using a factorization of the system matrix calculated in the forward modelling, solutions using different right-hand sides can be solved efficiently. This chapter is organized as follows. After describing the fundamental principles of an inversion algorithm, the adoption to the meshless case will be made. All relevant parts, which differ from a conventional scheme, are given and explained. After describing the meshless inversion algorithm,

example applications are done. Then, synthetic generated data will be inverted to test the algorithm and its implementation. The chapter closes with a summary and a discussion.

4.1 Basic inversion theory

To find a conductivity model from a set of given data, using some mathematical algorithm, a data vector should be defined. Here,

$$\mathbf{d} = \left(d_1, d_2, \ldots, d_{N_{data}}\right)^T \tag{4.1}$$

corresponds to all given measured data. This, for example can be different apparent resistivities or phases evaluated at the receiver stations for several frequencies. The amount of used data, or the length of the data vector will be denoted with N_{data}, so $\mathbf{d} \in \mathbb{R}^{N_{data}}$. The optimization problem, described here, is presented by

$$\mathcal{F}[m] + \mathbf{e} = \mathbf{d}. \tag{4.2}$$

The task is to find a model $m \in H$, whereas H denotes a Hilbert space and $\mathbf{e}$ the measurement noise. The operator $\mathcal{F} : H \to \mathbb{R}^{N_{data}}$ is the forward modelling operator. The result in this calculations is a model vector

$$\mathbf{m} = \left(m_1, m_2, \ldots, m_{M_{model}}\right)^T, \tag{4.3}$$

containing all values needed to characterize an appropriate parametrization of the model. Using a meshless method, the parametrization of the model conductivity is done using only the points from the forward modelling. In the case of two-dimensional magnetotelluric inversion, this vector holds all conductivities (or resistivities). Therefore, the transformation $\mathcal{F}$ becomes discrete: $F : \mathbb{R}^{M_{model}} \to \mathbb{R}^{N_{data}}$ and the inverse problem is now

$$\mathbf{F}[\mathbf{m}] + \mathbf{e} = \mathbf{d}. \tag{4.4}$$

In the case of an electromagnetic method, Equation (4.4) is

$$\mathbf{F}^{em}[\boldsymbol{\sigma}] + \mathbf{e} = \{\mathbf{E}, \mathbf{H}\}. \tag{4.5}$$

A mathematical solution to this problem can be by defining an inverse operator $(\mathbf{F}^{em})^{-1}\{\mathbf{E}, \mathbf{H}\} = \boldsymbol{\sigma}$, acting on the fields to give the model parameter. Nevertheless, the operator, which connects the model parameter to the fields, is generally non-linear. The inverse problem also is usually ill-posed, in the sense that there are more than one model, which fits the noisy data. This is the case, when $N_{data} < M_{model}$ and the inverse problem is underdetermined. Also, an inverse operator for this kind of problems may not exist. To address the problem of finding a solution to this ill-posed task, it can be regularized by a standard procedure called Tikhonov regularization (Tikhonov and Aesenin, 1977). In the framework of the Tikhonov regularization one seeks a model $\mathbf{m}^*$, which minimizes the parametric functional

$$\phi^{\beta}(\mathbf{m}, \mathbf{d}) = ||\mathbf{F}[\mathbf{m}] - \mathbf{d}||_2^2 + \beta||\mathbf{W}(\mathbf{m} - \mathbf{m}_{ref})||_2^2 = \phi_d + \beta\phi_m. \tag{4.6}$$

In this minimization, a trade-off between the first term, which is the data misfit $\phi_d = ||\mathbf{F}[\mathbf{m}] - \mathbf{d}||_2^2$, and a stabilization functional $\phi_m = ||\mathbf{W}(\mathbf{m} - \mathbf{m}_{ref})||_2^2$ can be achieved by selecting a proper regularization parameter β. The stabilization functional in Equation (4.6) referrers to a reference model $\mathbf{m}_{ref}$, which can be chosen in advanced. While the choice of selecting a good regularization parameter, which balances the minimization problem, is not a trivial task (Engl et al., 1996; Hansen, 1998). Two possible computational schemes are mainly used. The first one assumes a fixed regularization parameter and minimizes the given parametric functional. A popular way of selecting the right regularization parameter β is the L-curve scheme developed by Hansen (1998). The second method, finding an appropriate model, is to apply a two-stage method. Here, an adaptive regularization parameter is used and the data misfit ϕ_d will be reduced first. Than in the second stage, while trying to keep the data misfit constant, the model norm is reduced. A popular implementation of this scheme is Occam's inversion (Constable et al., 1987; Degroot and Constable, 1990).

Beside constraining the model space, to add regularization to the ill-posed problem, a non-linear functional has to be minimized. The classical mathematical way therefore is to differentiate Equation (4.6) with respect to $\mathbf{m}$ and set the result equal zero. This results in

$$\frac{\partial\phi^{\beta}(\mathbf{m}, \mathbf{d})}{\partial\mathbf{m}} = \mathbf{J}[\mathbf{m}]^T\,(\mathbf{F}[\mathbf{m}] - \mathbf{d}) + \beta\mathbf{W}^T\mathbf{W}(\mathbf{m} - \mathbf{m}_{ref}) = 0. \tag{4.7}$$

In this equation, $\mathbf{J}$ is the Jacobian or sensitivity matrix, describing how changes of the $j-th$ model parameter m_j affects the $i-th$ forward calculation $F_i(\mathbf{m})$, which is expressed

as

$$\mathbf{J}[\mathbf{m}] = \frac{\partial F_i[\mathbf{m}]}{\partial m_j}. \tag{4.8}$$

Using a Newton method to solve Equation (4.7) would include calculating the Hessian of $\mathbf{F}[\mathbf{m}]$, which involves second order Fréchet derivatives. To avoid this, the forward operator should be linearized by a Taylor expansion

$$\mathbf{F}[\mathbf{m} + \triangle\mathbf{m}] = \mathbf{F}[\mathbf{m}] + \mathbf{J}[\mathbf{m}]\triangle\mathbf{m} + O(\triangle\mathbf{m}^2). \tag{4.9}$$

The last term of the linearized forward operator can be assumed as small and can be neglected according to Aster et al. (2005). Using this linearization in Equation (4.7) gives

$$\mathbf{J}[\mathbf{m}]^T \left(\mathbf{F}[\mathbf{m}] + \mathbf{J}[\mathbf{m}]\triangle\mathbf{m} - \mathbf{d}\right) + \beta\mathbf{W}^T\mathbf{W}(\mathbf{m} + \triangle\mathbf{m} - \mathbf{m}_{ref}) = 0. \tag{4.10}$$

Rearranging terms and simplifying leads to

$$\mathbf{J}(\mathbf{m})^T\mathbf{J}[\mathbf{m}]\triangle\mathbf{m} + \beta\mathbf{W}^T\mathbf{W}\triangle\mathbf{m} = \mathbf{J}(\mathbf{m})^T \left(\mathbf{d} - \mathbf{F}[\mathbf{m}]\right) + \beta\mathbf{W}^T\mathbf{W}(\mathbf{m} - \mathbf{m}_{ref}). \tag{4.11}$$

This equation can be rearranged to a linear system, in which a perturbation $\triangle\mathbf{m}$ is its solution

$$\triangle\mathbf{m} = \left(\mathbf{J}[\mathbf{m}]^T\mathbf{J}[\mathbf{m}] + \beta\mathbf{W}^T\mathbf{W}\right)^{-1} \mathbf{J}[\mathbf{m}]^T \left(\mathbf{d} - \mathbf{F}[\mathbf{m}]\right) + \beta\mathbf{W}^T\mathbf{W}(\mathbf{m} - \mathbf{m}_{ref}). \tag{4.12}$$

In the end, this problem must be solved iterative until the right Earth model is obtained. This will be done with an iterative process solving for the next model with

$$\mathbf{m}_{k+1} = \mathbf{m}_k + \alpha\triangle\mathbf{m}. \tag{4.13}$$

The perturbation of the k-th step, should be calculated according to Equation (4.12) with

$$\triangle\mathbf{m} = \left(\mathbf{J}[\mathbf{m}_k]^T\mathbf{J}[\mathbf{m}_k] + \beta\mathbf{W}^T\mathbf{W}\right)^{-1} \mathbf{J}[\mathbf{m}_k]^T \left(\mathbf{d} - \mathbf{F}[\mathbf{m}_k]\right) + \beta\mathbf{W}^T\mathbf{W}(\mathbf{m}_k - \mathbf{m}_{ref}). \tag{4.14}$$

The parameter α in the update Equation (4.13) controls the step-length of the model update. To prevent an update, which overshoots the minimum and cause an increase in the parametric functional, a step-length of $0.1 < \alpha < 0.5$ was suggested by Armijo (1966). In this work, the formulation of Haber and Oldenburg (2000) is used to solve the

system (4.14). Thereby, the equivalent formulation

$$\begin{bmatrix} \mathbf{J}\left[\mathbf{m_k}\right] \\ \sqrt{\beta}\mathbf{W} \end{bmatrix} \triangle\mathbf{m} = \begin{bmatrix} \mathbf{d} - \mathbf{F}\left[\mathbf{m_k}\right] \\ -\sqrt{\beta}\mathbf{W}\left(\mathbf{m}_k - \mathbf{m}_{ref}\right) \end{bmatrix}, \tag{4.15}$$

is solved by an iterative solver (Paige and Saunders, 1982). In this implementation the regularization parameter is kept fix. The step-length α can be chosen by a line search method if a complex magnetotelluric data should be inverted. Here, setting α small enough, the non-linearity of the Gauss step will be linearized enough (Haber and Oldenburg, 2000).

4.2 Meshless Fréchet Derivatives

One main difficulty in deploying an inverse scheme is the calculation of a Fréchet derivative matrix or Jacobian matrix, which links a perturbation of the mode parameters to a change of the data. The difficulties are not to construct such Jacobian matrix, but involving a lot of solutions of the sparse linear system of equations makes the assembling suffering from this computational effort. When using traditional methods like finite elements or finite differences, several schemes have been proposed to calculate the Jacobian matrix efficiently (Rodi, 1976; Farquharson and Oldenburg, 1996; Lugão et al., 1997; Rodi and Mackie, 2001). In a magnetotelluric inversion the data, which is incorporated in the inversion process, are normally the apparent resistivities and phases. In this case, the Jacobian consists of Fréchet derivatives of the apparent resistivities and phases with respect to the model parameters, the conductivities of the Earth model.
The aim of this section is to give an overview, how these derivatives of the apparent resistivities and phases with respect to the model conductivities, can be calculated in a meshless framework. The work here follows the ideas of Lugão and Wannamaker (1996) and Lugão et al. (1997) as well as Jupp and Vozoff (1977) and Schwarzbach and Haber (2013), adapted to the meshless framework.
First, the apparent resistivities in Equation (2.93) and phases from Equation (2.94) are derived by using the magnetotelluric impedance. Now, the basic building block are derivatives of the electromagnetic fields for both magnetotelluric modes with respect to the model conductivities. On the other hand, the magnetotelluric impedance is derived by the electromagnetic fields at the observation site. The first task is to derive the Fréchet derivatives of the fields with respect to the model conductivities. As in Jupp and Vozoff

(1977) this is done by direct differentiation of the linear system that was assembled in the forward calculation

$$\mathbf{A}(\boldsymbol{\sigma})\mathbf{u} = \mathbf{S}. \tag{4.16}$$

The coefficient matrix is assembled from two individual matrices, depending on the chosen magnetotelluric mode

$$\mathbf{A}(\boldsymbol{\sigma}) = \begin{cases} \mathbf{A}^a + i\omega\mathbf{A}^b(\boldsymbol{\sigma}), & \boldsymbol{\sigma} = (\sigma_1, \ldots, \sigma_N) \text{ TE-mode}, \\ \mathbf{A}^a(\boldsymbol{\sigma}) + i\omega\mathbf{A}^b, & \boldsymbol{\sigma} = (\sigma_1^{-1}, \ldots, \sigma_N^{-1}) \text{ TM-mode}, \end{cases} \tag{4.17}$$

and as defined before, the solution vector is $\mathbf{u} \in \{\mathbf{E}_x, \mathbf{H}_x\}$. Here, the coefficient matrix is parametrized by the conductivity vector $\boldsymbol{\sigma}$, which holds the conductivities at all points. In this formulation the source vector vanishes. Deviating Equation (4.16) with respect to a conductivity at point i, for example in the TE-mode, gives

$$\begin{aligned} \mathbf{A}(\boldsymbol{\sigma})\frac{\partial \mathbf{E}_x}{\partial \sigma_i} &= -\frac{\partial \mathbf{A}(\boldsymbol{\sigma})}{\partial \sigma_i}\mathbf{E}_x \\ &= -i\omega\frac{\partial \mathbf{A}^b(\boldsymbol{\sigma})}{\partial \sigma_i}\mathbf{E}_x. \end{aligned} \tag{4.18}$$

The matrix on the left hand-side of Equation (4.18) is sparse and has only n entries. In this case, n is the number of neighbours used to calculate the coefficients for the approximation of the functionals. Thus, Equation (4.18) consists of coefficients calculated from Equation (3.77). These coefficients are already formed during the forward calculation. To proceed, solving Equation (4.18) needs to invert the coefficient matrix $\mathbf{A}(\boldsymbol{\sigma})$. This rather numerical expensive task can be avoided by explicitly calculating individual rows of the inverse coefficient matrix. As explained by Lugão and Wannamaker (1996), this task has his origin in the principle of electromagnetic reciprocity, in which the roles of sources and receivers are interchangeable. In the notation of Lugão et al. (1997) this is

$$\mathbf{A}(\boldsymbol{\sigma})\hat{\mathbf{G}} = \mathbf{S}(1), \tag{4.19}$$

in which the source vector is assembled with an unit source at the point i

$$\mathbf{S}(1) = \begin{pmatrix} 0 \\ \vdots \\ 1 \\ \vdots \\ 0 \end{pmatrix}. \tag{4.20}$$

Solving this equation gives the responses for all points in the domain and multiplying the solution vector with Equation (4.18), gives a formula for the Fréchet derivatives of the fields with respect to the model conductivities. This results in

$$\frac{\partial \mathbf{E}_x}{\partial \sigma_i} = -i\omega \hat{\mathbf{G}} \frac{\partial \mathbf{A}^b(\boldsymbol{\sigma})}{\partial \sigma_i} \mathbf{E}_x, \tag{4.21}$$

and

$$\frac{\partial \mathbf{H}_x}{\partial \sigma_i} = \hat{\mathbf{G}} \frac{\partial \mathbf{A}^a(\boldsymbol{\sigma})}{\partial \sigma_i} \mathbf{H}_x. \tag{4.22}$$

The advantage of this procedure is a numerical cheaper way to calculate the Jacobian matrix, without solving for each model conductivity. Only $N_{receiver} \times N_{freq}$ solutions of Equation (4.19) are needed, in which $N_{receiver}$ is the number of receivers and N_{freq} is the number of used frequencies. This task demands a numerical algorithm, in which capable to solve a system of equation with different right-hand sides many times. Thus factorizing $\mathbf{A}(\boldsymbol{\sigma})$ during the forward calculation allows the solution of Equation (4.19) with many right-hand sides at almost no extra costs. Using the meshless framework, the derivatives of the system matrix with respect to the model conductivity σ_i can be done by deviating the vectors $\mathbf{L}_i^{\Omega}(\mathcal{P})$ in Equations (3.80) for the TE-mode

$$\frac{\mathbf{L}_i^{\Omega}(\mathcal{P})}{\partial \sigma_i} := \left[-i\omega p_1(\mathbf{x}_i), \ldots, -i\omega p_Q(\mathbf{x}_i) \right]^T, \tag{4.23}$$

and deviating the vectors $\mathbf{L}_i^{\Omega}(\mathcal{P})$ in Equations (3.81) for the TM-mode

$$\frac{\mathbf{L}_i^{\Omega}(\mathcal{P})}{\partial \sigma_i} := \left[\nabla \cdot \left(\sigma(\mathbf{x}_i)^{-2} \nabla p_1(\mathbf{x}_i) \right), \ldots, \nabla \cdot \left(\sigma(\mathbf{x}_i)^{-2} \nabla p_Q(\mathbf{x}_i) \right) \right]^T. \tag{4.24}$$

By examining Equation (4.24) it can be seen that a second order operator needs to be approximated. This is problematic in the case of the proposed meshless algorithm presented here. If combining Equation (4.24) with Equation (4.22) the resulting formulation for the TM-mode is unstable and gives no results when using it in forming the Jacobian matrix. Here, more research has to be done to stabilize this process to successful calculate the Jacobian matrix in this meshless formulations. Nevertheless, if the Fréchet derivatives of the fields have been calculated, derivatives of the auxiliary fields should be derived. For the TE-mode this is

$$\frac{\partial H_y^k}{\partial \sigma_i} = -\frac{1}{i\omega\mu_0} \frac{\partial}{\partial z} \frac{\partial E_x^k}{\partial \sigma_i}. \tag{4.25}$$

Where $\partial E_x^k/\partial\sigma_i$ is the electrical field at the surface for k-th frequency-receiver combination. As well as for the vertical magnetic field

$$\frac{\partial H_z^k}{\partial\sigma_i} = \frac{1}{i\omega\mu_0}\frac{\partial}{\partial x}\frac{\partial E_x^k}{\partial\sigma_i}. \tag{4.26}$$

Using the TM-mode the auxiliary fields can be computed with

$$\frac{\partial E_y^k}{\partial\sigma_i} = \frac{1}{\sigma_i}\left(\frac{\partial}{\partial z}\frac{\partial H_x^k}{\partial\sigma_i} - \sigma_i E_y\right). \tag{4.27}$$

and also

$$\frac{\partial E_z^k}{\partial\sigma_i} = -\frac{1}{\sigma_i}\left(\frac{\partial}{\partial x}\frac{\partial H_x^k}{\partial\sigma_i} + \sigma_i E_z\right). \tag{4.28}$$

When utilizing a magnetotelluric inversion, the Jacobian matrix consist of partial derivatives of the data with respect to the model conductivities. Normally in this case, the data consists of apparent resistivities and phases. This requires partial derivatives with respect to model resistivities which should also be logarithmically scaled as explained in Wheelock et al. (2015). As all Fréchet derivatives of the fields for both magnetotelluric modes can be derived, as the k-th apparent resistivity logarithmically scaled derivative with respect to the i-th model parameter (Jupp and Vozoff, 1977):

$$\frac{\partial \log\rho_a^k}{\partial \log\rho_i} = \frac{2}{\omega\mu_0} Re\left(\frac{\partial Z^k}{\partial\rho_i}\bar{Z}^k\right)\left(\frac{\rho_i}{\rho_{a,i}}\right), \tag{4.29}$$

and for the derivative of the phase

$$\frac{\partial\varphi^k}{\partial \log\rho_i} = \frac{\rho_i\,\cos^2\varphi_k\left(Im\left(\frac{\partial Z^k}{\partial\rho_i}\right) - \tan\varphi_k Re\left(\frac{\partial Z^k}{\partial\rho_i}\right)\right)}{Re(Z^k)}. \tag{4.30}$$

In both Equations (4.29) and (4.30), the partial derivatives of the impedance Z is used, while $\bar{Z}$ denotes the complex conjugate. For both magnetotelluric modes, the derivatives of the impedance can be derived with the help of the Fréchet derivatives of the field, which is

$$\frac{\partial Z^k}{\partial\rho_i} = \frac{1}{H^k}\left(\frac{\partial E^k}{\partial\rho_i} - Z^k\frac{\partial H^k}{\partial\rho_i}\right). \tag{4.31}$$

By applying Equation (4.31), the fields have to be chosen according to the used magnetotelluric mode. For the TE mode E_x, H_y should be used in Equation (4.31) and for the TM mode H_x, E_y, while Z^k is the normal magnetotelluric impedance.

4.3 Regularization

Due to the non-linearity of the inverse problem, a regularization of the iterative scheme has to be done. Here in this work, a smoothness regularized inversion is applied. Inspecting the parametric functional in Equation (4.6), the norm of the stabilization term can be expressed as

$$\phi_{\nabla_m} = \frac{1}{2}||\nabla(\mathbf{m} - \mathbf{m}_{ref})||_2^2 = \frac{1}{2}\int_\Omega |\nabla(\mathbf{m} - \mathbf{m}_{ref})|^2 \, d\Omega, \tag{4.32}$$

or as

$$\phi_{\nabla_m^2} = \frac{1}{2}||\nabla^2(\mathbf{m} - \mathbf{m}_{ref})||_2^2 = \frac{1}{2}\int_\Omega |\nabla^2(\mathbf{m} - \mathbf{m}_{ref})|^2 \, d\Omega, \tag{4.33}$$

for either gradient smoothing or the latter Laplace smoothing. By using finite element formulations, this task is non-trivial, because the conductivity assumes to be piecewise constant on the elements and at an element interface, singularities occur. A primal-dual finite element formulation using Raviart-Thomas elements must be used to calculate the regularization functional, as Schwarzbach and Haber (2013) explain. But by defining special gradient operators, as defined by Lelièvre and Farquharson (2013), the regularization can be implemented with less effort. Here, the meshless framework is used to calculate Equation (4.32) and (4.33). Thanks to the previously discretized partial differential equation from the forward modelling, the coefficients from this discretization can be reused. Here, the coefficients matrices defined in Equation (3.77) are already calculated and only the convenient functionals need to be used to approximate Equation (4.32) or (4.33). Therefore, for all points in the modelling domain, which should be included into the inversion process, the functional $\phi_m(m)$ will be calculated using the direct approximation and at the i-th point this is

$$\phi_{\nabla_m}(m_i) = \frac{1}{2}\int_\Omega |\nabla(m_i - m_{i,ref})|^2 \, d\Omega \approx \sum_{k=1}^{n} a_{k,\int \nabla}(\mathbf{x}) m(\mathbf{x}_k), \tag{4.34}$$

and

$$\phi_{\nabla_m^2}(m_i) = \frac{1}{2}\int_\Omega |\nabla^2(m_i - m_{i,ref})|^2 \, d\Omega \approx \sum_{k=1}^{n} a_{k,\int \nabla^2}(\mathbf{x}) m(\mathbf{x}_k). \tag{4.35}$$

Thus, Equations (4.32) and (4.32) can be approximated by calculating the integrals locally at the points inside the modelling domain, and then summing over all approximations. This procedure is also used by Levin (1999) to calculate stable integration rules.

4.4 Magnetotelluric example inversions

In this section some example inversions will be presented. There will be four synthetic models, which will be inverted to test the capabilities of the inverse algorithm. All inversions use the TE-mode and eight selected frequencies from 0.4Hz to 0.003125Hz. Thus, starting with 0.4Hz every next frequency is the half of the previous one, until 0.003125Hz is reached. The data, which should be inverted, will be synthetically calculated, using the conductivity models presented in Figures 4.38, 4.44 and 4.47. Here a fixed regularization parameter $\beta = 100$ will be used. This choice, based on trail and error, performs the best for all models. In all example inversions the Laplacian smoothing stabilizer will be used and a model update step length of $\alpha = 0.3$ is selected. The stopping criteria is in all cases a RMS-misfit calculated by

$$RMS = \sqrt{\frac{\sum_{i=1}^{N_{data}} |\frac{d_i - F[\mathbf{m}]}{e_i}|^2}{N_{data}}}, \tag{4.36}$$

reaching a predefined value. Also if the misfit is not reduced in an iteration, the algorithm stops the inversion. The example inversions should deliver insights into four different aspects. First, a simple prism embedded into a homogeneous half-space will be inverted to proof if the algorithm performs right. Therefore, every step of its iteration a Figure will be presented here, to see how the conductivity model evolves during the iterations. The second step, will be done with the same data, but 5% noise was added. This should

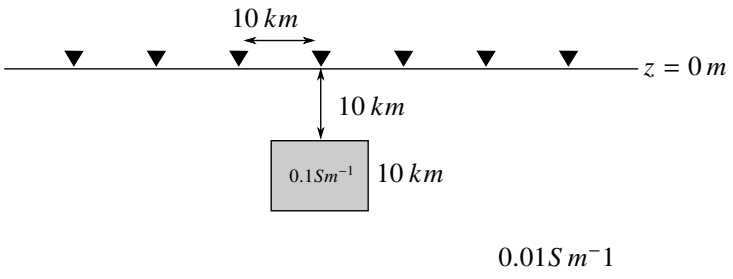

Figure 4.38: Conductivity model used in the first inversion example. The triangles mark the receiver positions.

give a first insight how the algorithm perform with noisy data. The third test will be a resolution test. Here, a model should be recovered, which consists of different conductive bodies inside a homogeneous half-space. One of the conductors is thinner than the other and the question is if it can be resolved. The last example will show the advantage of

using a meshless model by incorporating topography. Here, an Earth surface including topography will be used to recover the conductivity structure of a buried prism. Using a point sampling instead of a mesh gives more flexibility. Beginning with the first example, the conductivity model pictured in Figure 4.38 should be inverted, using seven receiver stations with a separation distance of $10\,km$. First, the synthetic data was produced using the meshless forward algorithm and afterwards this data will be inverted. The inverse algorithm should give a precise recover of the conductivity model used in the forward calculations. The final model is displayed in Figure 4.39. As it can be seen,

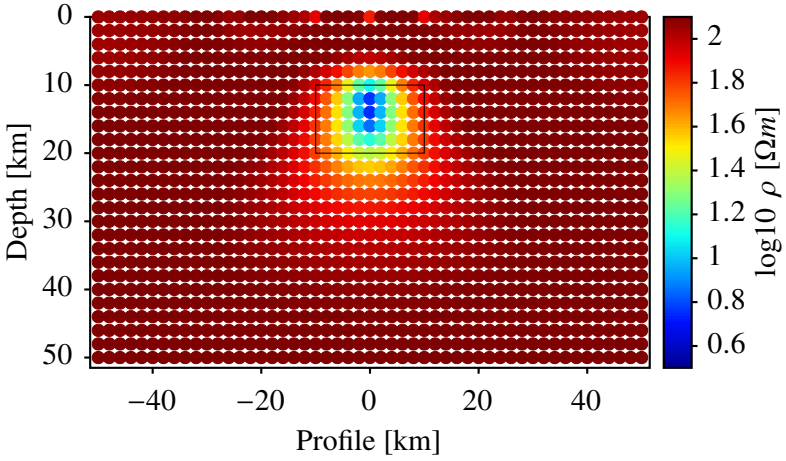

Figure 4.39: Final conductivity model produced in the first inversion example.

the conductivity structure is reproduced at the place where it should be. The inverse algorithm overshoots the conductivity of the prism by $4\mathrm{S\,m^{-1}}$, but this can be avoided by a step length selected with an adaptive algorithm. For this inversion, the algorithm needs seven iterations and stops at a RMS-misfit of 1.45.

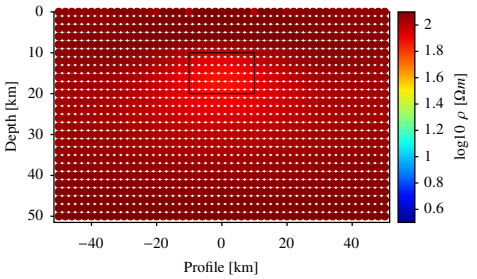

(a) 1. iteration (96.72 rms)

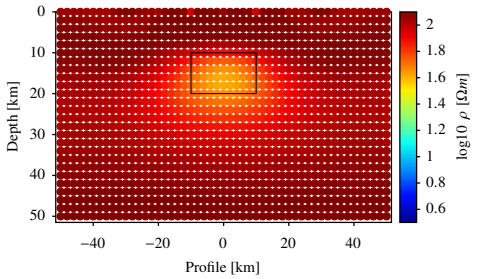

(b) 2. iteration (37.07 rms)

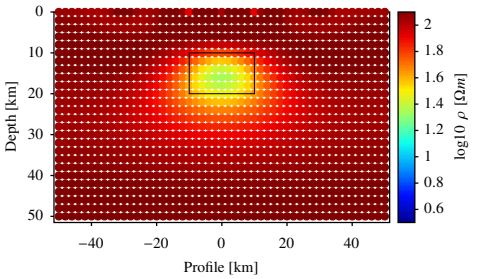

(c) 3. iteration (10.35 rms)

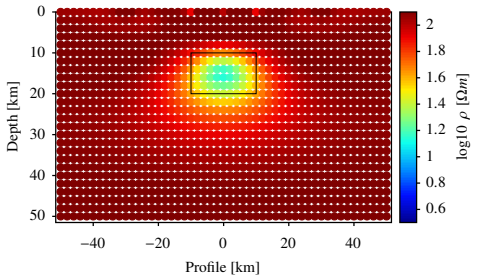

(d) 4. iteration (9.45 rms)

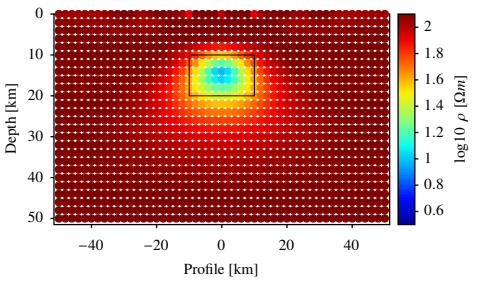

(e) 5. iteration (2.45 rms)

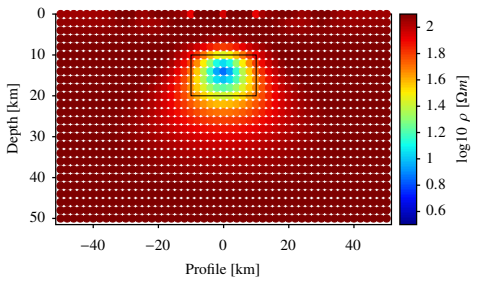

(f) 6. iteration (2.80 rms)

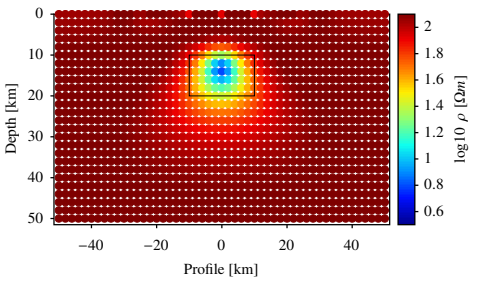

(g) 7. iteration (2.41 rms)

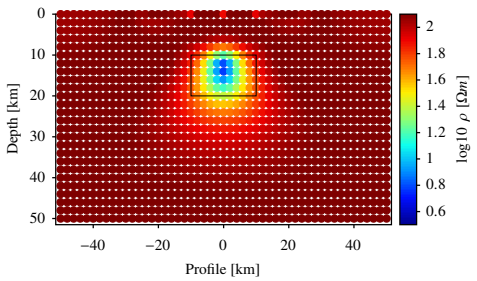

(h) 8. iteration (1.87 rms)

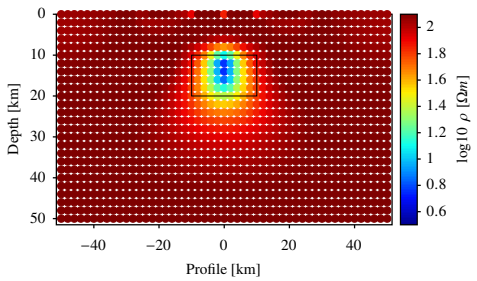

(i) 9. iteration (1.45 rms)

Figure 4.40: All iterations for the first example inversion

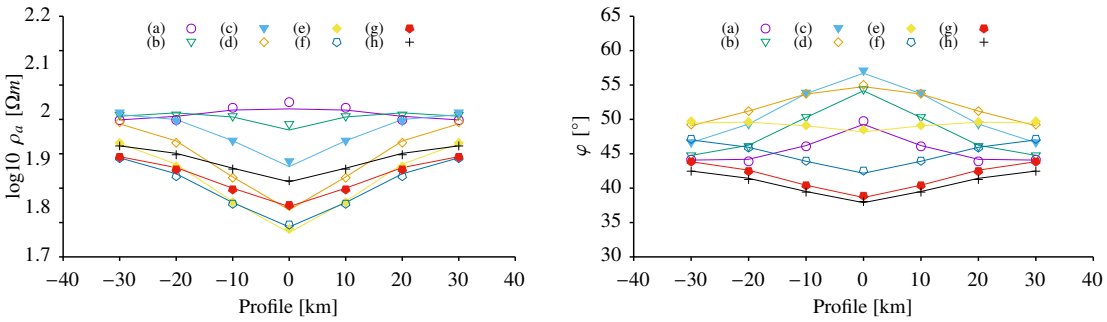

Figure 4.41: Synthetic data (solid lines) and modelled data (symbols) for the first inversion example plotted for all stations and for the frequencies (a) 0.4Hz*, (b)* 0.2Hz*, (c)* 0.1Hz*, (d)* 0.05Hz*, (e)* 0.025Hz*, (f)* 0.0125Hz*, (g)* 0.00625Hz*, (h)* 0.003125Hz*.*

Every single iteration step can be seen in Figure 4.40. From these figures, it can be seen that the algorithm reproduces geometry of the conductivity structure good until iteration six. After this iteration, it begins to overestimate the conductivity values and the structure begins to narrow. The synthetic data and the modelled data are pictured in Figure 4.41. The next step will be to add random noise to the synthetic data, to test the algorithm if it can handle data, which was polluted by noise. In this example 5% noise was added to the synthetic generated apparent resistivities and phases. The results of the inversion can be seen in Figure 4.42. This figure displays the final conductivity model. As it can be seen in the inversion results, the added noise prevent the algorithm to perform as accurate as without noise. The inversion routine stops with an RMS-misfit of 9.93 and the modelled data, which can be seen in Figure 4.43, shows different estimates than using no noise. Nevertheless, the depth and lateral position of the conductive prism can be estimated even in the presence of noise. The next example which will be given, will test the resolution

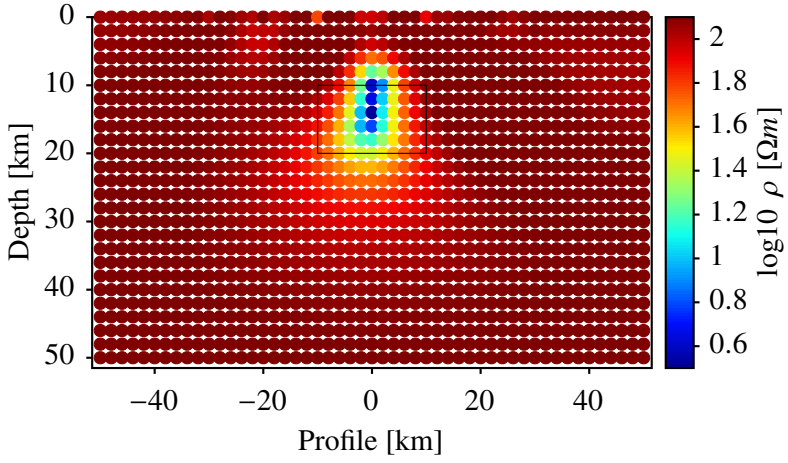

Figure 4.42: Final conductivity model produced in the first inversion example using noisy data.

of the inverse algorithm. For this test a homogeneous half-space model was used with

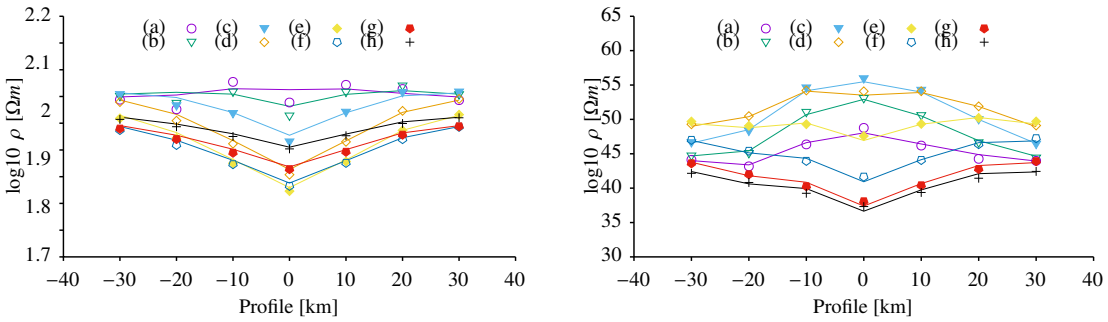

Figure 4.43: Synthetic noisy data (solid lines) and modelled data (symbols) for the first inversion example plotted for all stations and for the frequencies (a) 0.4Hz, *(b)* 0.2Hz, *(c)* 0.1Hz, *(d)* 0.05Hz, *(e)* 0.025Hz, *(f)* 0.0125Hz, *(g)* 0.00625Hz, *(h)* 0.003125Hz.

two vertical long conductivity structures. One structure is in a depth of ten kilometres and is ten kilometres thick. The other structure is a shallow thin conductive structure. The model is displayed in Figure 4.44. For this algorithm synthetic data was produces with the meshless algorithm. The question, which should be answered, is if the inversion algorithm can produce a conductivity model, in which both structures can be recovered. Also, if it is possible to image thin conductive structures. For this example nine receivers are placed in top of the surface in a distance of ten kilometres to each other. By using the

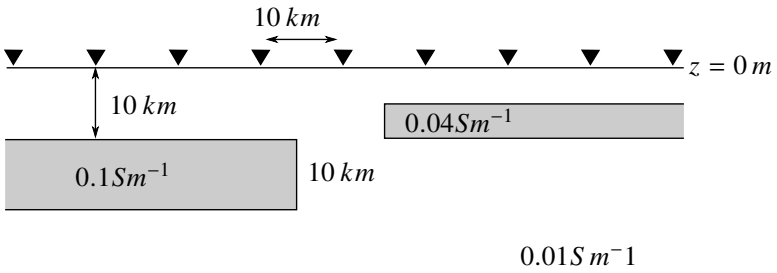

Figure 4.44: Schematic of the conductivity model used in the inversion resolution test. The triangles mark the position of the receivers.

same frequencies as before, a conductivity model was recovered in 13 iterations. The final RMS-misfit of 1.69 is nearly good as in the case of the single prism model. The final conductivity model can be seen in Figure 4.45. Here, it can be clearly seen, that both of the conductivity structures can be distinguished. Also the thinner conductivity structure can be recovered well. The thickness of these structures are good estimated. Only the thicker structure is somehow larger at the middle of the model. Nevertheless, the algorithm also performs well in this case. The synthetic data and the predicted values can be seen in Figure 4.46.

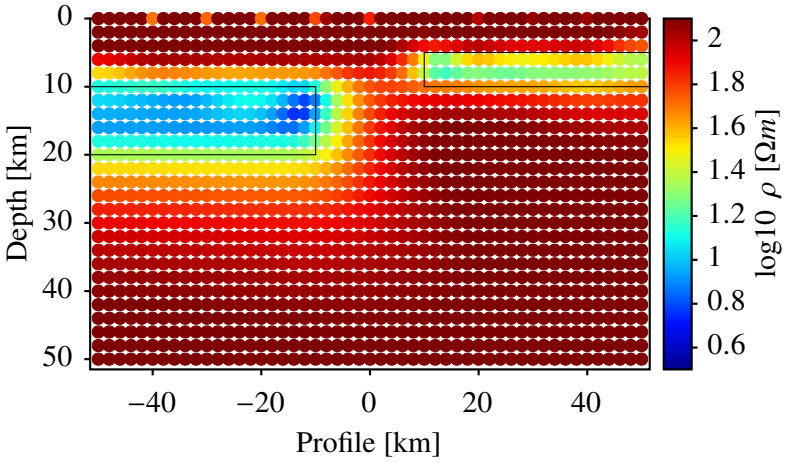

Figure 4.45: Final conductivity model produced in the resolution inversion example using synthetic data.

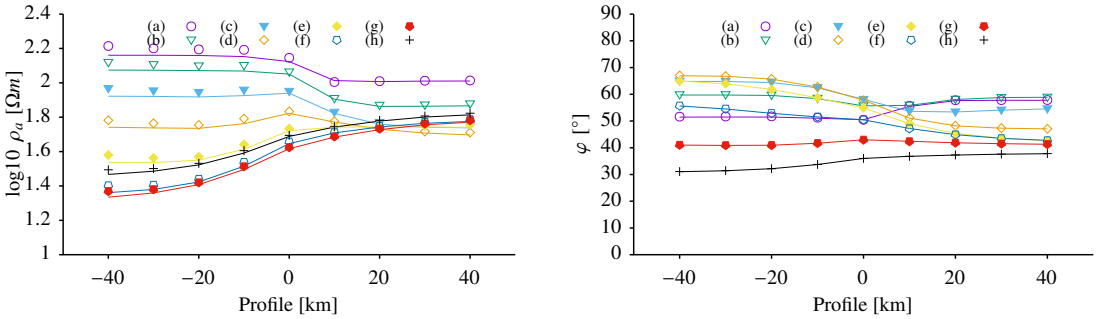

Figure 4.46: Synthetic data (solid lines) and modelled data (symbols) for the resolution inversion example plotted for all stations and for the frequencies (a) 0.4Hz, *(b)* 0.2Hz, *(c)* 0.1Hz, *(d)* 0.05Hz, *(e)* 0.025Hz, *(f)* 0.0125Hz, *(g)* 0.00625Hz, *(h)* 0.003125Hz.

The last example is to test the algorithm if it can handle topography. This test is tailored to use a meshless method, because point sets can be easily adapted to the topographic slope of the air-Earth interface. The model, which will be used, is displayed in Figure 4.47. It consists of a homogeneous half-space with a sinusoidal topography. At the surface nine receivers are placed to capture magnetotelluric responses and the same frequency range is used as before. Figure 4.47 shows the conductivity model used in this test. The same conductive prism should be recovered, but here in additional topography is added to the air-Earth interface. The final model can be seen in Figure 4.48. By inverting topography

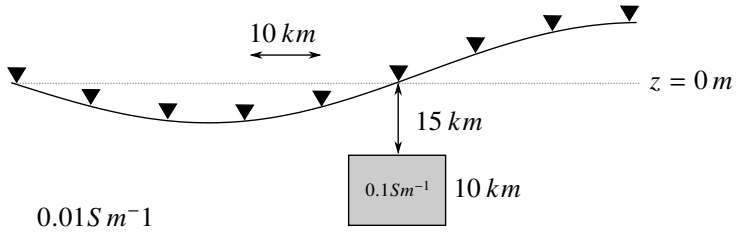

Figure 4.47: Conductivity topography model used in the inversion example. The triangles mark the receiver positions.

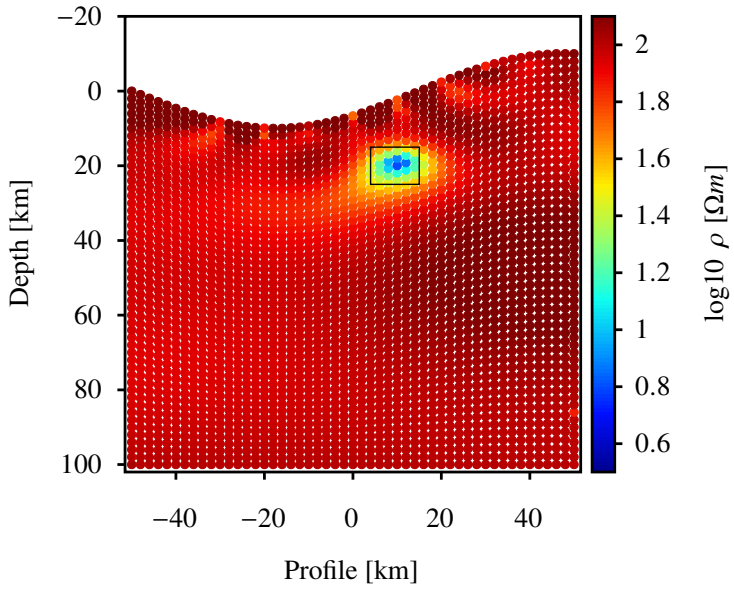

Figure 4.48: Final conductivity model produced in the first topography inversion example using synthetic data data.

it can be seen, that the spatial position of the conductivity structure can be recovered. Also, slight inversion artefacts can be seen at the air-Earth interface. The algorithm needs 18 iteration steps to reach a RMS of 6.26. This value cannot be improved with more iterations. Nevertheless, to incorporate topography into the algorithm not many parts of the program needs to be adapted. Here, only the point sampling needs to fill te surface area. For the TE-mode an air layer has to be included, but this is not shown in the final conductivity models. Also if topography is used, the fields at the receivers need to be correctly described by incorporating the slope of the air-Earth surface as described in Wannamaker et al. (1985). The final model responses displayed in conjunction with the synthetic data is shown in Figure 4.49.

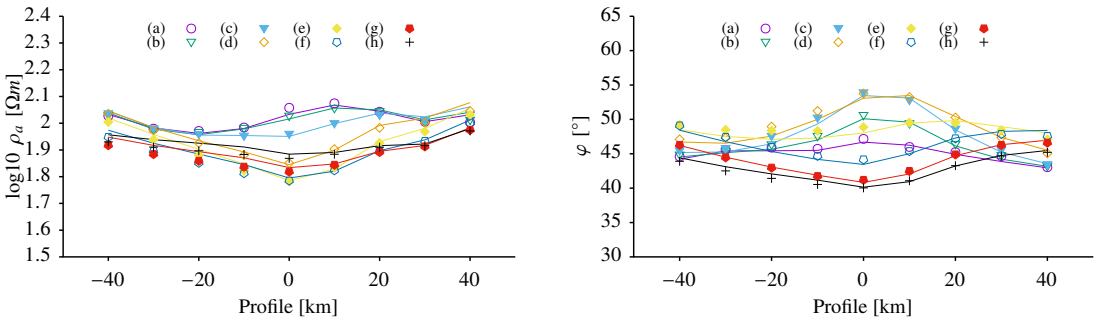

Figure 4.49: Synthetic noisy data (solid lines) and modelled data (symbols) for the first inversion example plotted for all stations and for the frequencies (a) 0.4Hz, *(b)* 0.2Hz, *(c)* 0.1Hz, *(d)* 0.05Hz, *(e)* 0.025Hz, *(f)* 0.0125Hz, *(g)* 0.00625Hz, *(h)* 0.003125Hz.

4.5 Summary and Conclusions

In this chapter a meshless inversion algorithm was developed to invert magnetotelluric data on point sets. First, an introduction to general inversion theory was given and the basic equations where stated to form an algebraic system to give the model update. In the next step the calculation of the Jacobi matrix was discussed and the computational work flow was described. Here the formulation for the two magnetotelluric modes are given. This scheme uses the principle of electromagnetic reciprocity to calculate the derivatives of the electromagnetic field with respect to the model parameters. Mathematically this procedure is somehow related to calculate rows of the inverse of a matrix. Using unit sources at the receiver points, these rows can be computed and in conjunction with the derivatives od the sparse discretization with respect to the model parameter the derivatives of the fields can be calculated. Using a meshless scheme, a working implementation for the TE-mode was realized. Due to instabilities of the second order operator in derivatives of the sparse matrix this formulation fails to calculate proper field derivatives for the TM-mode. Here additional research on an extended formulation needs to be done to get the Jacobi matrix calculations working.

Nevertheless for the TE-mode a full inversion implementation was developed. Here, the calculation of the Jacobi matrix succeeded and a stable meshless inversion algorithm was realized. Also first example inversions have been presented to show the potential of the scheme. Simple block structures can be inverted successfully and even if noise is included in the data reasonable conductivity models can be recovered. Also, due to the meshless approach, topography enters the formulation with almost no extra effort and Earth model with topography can be inverted successfully.

Summary

In this thesis, several new methods for the modelling and inversion of magnetotelluric data have been developed. Starting from the physical description of the magnetotelluric experiment, mathematical formulations have been derived for its simulation. Here, two ways have been followed to realize this. The mathematical description for the two-dimensional magnetotelluric problem was described and second order formulations have been introduced. Here, the fields split into two modes, the TE- and TM-mode. To simulate these modes, two second order partial differential systems need to be considered in order to simulate the electrical or the magnetic field. Boundary value problems are given for both and special assumptions have been made to use these formulations for magnetotelluric modelling. For the three-dimensional case, a vector potential formulation was given in terms of different gauging conditions. These gauging conditions are needed to remove the ambiguousness in the formulation of the vector potential and enables a stable discretization. To achieve this, second order formulations have been given to state a boundary value problem for the three-dimensional case. In this potential field formulation the fields are continuous across conductivity interfaces. This behavior is beneficial for using a meshless algorithm, because in these kind of discretizations interfaces are difficult to model. After defining the proper mathematical abstraction of the physical problem, the numerical part of the formulation begins.

In this thesis, an introduction into meshless modelling was given and the basic concept of a meshless modelling scheme was discussed. The advantages of using no meshes and discretize the partial differential equations on point samplings have been described. The basic scheme of constructing a discretization point by point, while gathering all neighbours, was explained to introduce the building block of the discretization scheme used in this thesis. The generalized moving least squares technique can approximate linear functionals from a set of functional data, with the help of a local polynomial reproduction system. This scheme needs to minimize a quadratic optimization problem with linear constrains, to construct the coefficients used in the approximation. It was shown by a couple of researchers, that this kind of approximation is related to the method of Backus and Gilbert. An extension has been made to generalize the approximation scheme to a staggered case, in which the divergence operator can be defined on a primal-dual complex only using the neighbouring points and a radial component function. This forms the basis of approximating vector fields and their divergence in the framework of the

generalized moving least squares approximation. To predict theoretically the error of the approximation scheme, error bounds are cited from the literature. In these bounds the error is proportional to the fill distance of the point sampling and it should be decrease if the fill distance increases. Also, the error is controlled by the polynomial degree. The error bounds are given for all kinds of approximations presented in this thesis and they can be used in conjunction with convergence tests.

By introducing a direct discretization scheme, it is possible to write the entire boundary value problem in terms of functionals. Here, an algebraic system corresponding to the discretization can be written only in terms of functionals. The task which remains, is to approximate the functionals given by the actual partial differential system. To proceed towards a meshless formulation for the magnetotelluric problem, two-dimensional and three-dimensional meshless formulations of the second order systems are proposed. Here, for the TE- and TM-mode different formulations using a set of linear functionals are stated, and by using such methodology the formulation of the meshless three-dimensional problem follows naturally. It can be seen, that a vector potential formulation can be reformulated in terms of linear functionals. Using this scheme, one has to collect all the coefficients from the functional approximation into an algebraic system to form the discretization. After introducing the strong formulations to discretize the boundary value problem, a weak formulation was given in terms of completeness. Here, integrals have to be evaluated. This makes this formulation costly and an actual implementation was not accomplished. After having defined all the formulations for the boundary value problems, the actual implementations where described. The general work flow of a meshless scheme purports the following tasks towards a meshless magnetotelluric scheme.

After defining proper scaled and shifted polynomial basis functions, weight functions have to be defined. In order to calculate the normal equations in the functional approximations, the actual implementations for the two- and three-dimensional case where given. Here, different options are possible to define meshless approximation methods. The pure point collocation scheme can be used, or the staggered scheme is available to discretize the differential equations. An important part of the scheme is the description of the conductivity interfaces. Different methods have been reviewed, and the 'double node' approach has been selected in combination with a material averaging scheme, to serve in the computations of this thesis.

Some remarks about the generation of point samplings have been made. Here, a lot of possibility methods are available, but in this thesis a Poisson disk sampling algorithm is used to generate unstructured point samplings. Also, it was discussed how to generate spatially adapted point samplings using a stretching function. The chapter about solving

the linear system informs about the methods, how to solve the sparse system of equations which, results from the discretization. Here, the sparsity pattern of two matrices have been presented and how the system is solved. Also, examples on the run times have been given in comparison to values from the literature. After having all parts described for the meshless implementations, example calculations were given. First, convergence results have been presented for different meshless formulations. They confirm that it is possible, even in the presence of steep conductivity contrasts, to achieve second order accuracy. The results are compared to values from the literature and similar convergence rates can be observed compared to finite element calculations. The effect of the spatially adaptation of point samplings have been presented and discussed. After testing the convergence of the meshless schemes, magnetotelluric example calculations have been given to test the algorithm. Two models from the literature have been used to study the accuracy of the meshless algorithm. The authors of these models provide analytical results and the accuracy of the meshless scheme was tested against these values. It can be concluded from the example calculations, that the meshless scheme provides a stable, flexible and accurate solution to the two-dimensional magnetotelluric modelling problem. The three-dimensional meshless algorithm was tested by using a simple conductivity model. Here, in comparison to a solution from a finite differences algorithm the meshless calculations are in a good agreement to these reference values.

After developing the two-dimensional magnetotelluric modelling algorithm, a meshless scheme to invert magnetotelluric data has been proposed. Here, the difficulty lies in the formulation of the Jacobian matrix, which is needed in the inversion process. Due to instabilities in the Jacobi matrix formulation of the TM-mode, only the TE-mode was considered in the later development. Then, a method to compute the needed regularization was proposed and in the last part of this chapter, examples have been given to test the newly developed inverse algorithm. Four different tests have been conducted in order to investigate the resolution of the inverse problem, the ability to handle noisy data and if it is possible to incorporate topography into the inversion process. All test have been successfully accomplished and the newly inverse scheme performed well in each case.

Bibliography

F. Abramovici. Applying the backus-gilbert theory to function approximation. *Stud. Univ. Babes-Bolyai Math.*, 56(2):207–218, 2011. (Cited on page 36.)

Y. Aharonov and D. Bohm. Significance of electromagnetic potentials in the quantum theory. *Physical Review*, 115(3):485, 1959. (Cited on page 11.)

A. G. M. Ahmed, H. Perrier, D. Coeurjolly, V. Ostromoukhov, J. Guo, D.-M. Yan, H. Huang, and O. Deussen. Low-discrepancy blue noise sampling. *ACM Trans. Graph.*, 35(6):247:1–247:13, November 2016. (Cited on page 74.)

P. R. Amestoy, I. S. Duff, and J.-Y. L'Excellent. Multifrontal parallel distributed symmetric and unsymmetric solvers. *Comput. Methods in Appl. Mech. Eng.*, 184:501–520, 2000. (Cited on page 78.)

S. Ansari and C. Farquharson. 3D finite-element forward modeling of electromagnetic data using vector and scalar potentials and unstructured grids. *GEOPHYSICS*, 79(4):E149–E165, May 2014. (Cited on page 2.)

M. Armentano. Error Estimates in Sobolev Spaces for Moving Least Square Approximations. *SIAM Journal on Numerical Analysis*, 39(1):38–51, January 2001. (Cited on page 44.)

L. Armijo. Minimization of functions having lipschitz continuous first partial derivatives. *Pacific Journal of mathematics*, 16(1):1–3, 1966. (Cited on page 102.)

D. N. Arnold, P. B. Bochev, R. B. Lehoucq, R. A. Nicolaides, and M. Shashkov. *Compatible spatial discretizations*, volume 142. Springer Science & Business Media, 2007. (Cited on page 36.)

D. Aruliah, U. Ascher, E. Haber, and D. W. Oldenburg. A method for the forward modelling of 3-d electromagnetic quasi-static problems. *Mathematical Models and Methods in Applied Sciences*, 11(01):1–21, 2001. (Cited on page 15.)

D. A. Aruliah. *Fast solvers for time-harmonic Maxwell's equations in 3D*. PhD thesis, University of British Columbia, 2001. (Cited on pages 13, 15, and 73.)

I. Ascencio-Lopez, O. Meruvia-Pastor, and H. Hidalgo-Silva. Adaptive Incremental Stippling using the Poisson-Disk Distribution. *Journal of Graphics, GPU, and Game Tools*, 15(1):29–47, January 2010. (Cited on page 75.)

R. C. Aster, B. Borchers, and C. H. Thurber. *Parameter estimation and inverse problems.* Amsterdam: Elsevier, 2005. (Cited on pages 99 and 102.)

S. N. Atluri and S. Shen. *The meshless local Petrov-Galerkin (MLPG) method*. Crest, 2002. (Cited on page 52.)

S. N. Atluri and T. Zhu. A new meshless local petrov-galerkin (mlpg) approach in computational mechanics. *Computational Mechanics*, 22(2):117–127, August 1998. (Cited on pages 36, 52, and 54.)

S. N. Atluri, H. G. Kim, and J. Y. Cho. A critical assessment of the truly meshless local Petrov-Galerkin (MLPG), and local boundary integral equation (LBIE) methods. *Computational Mechanics*, 24(5):348–372, 1999. (Cited on pages 52 and 53.)

I. Aziz and N. Haider. Meshless and multi-resolution collocation techniques for steady state interface models. *International Journal of Computational Methods*, pages 1750073–1 – 1750073–37, 2017. (Cited on page 68.)

I. Babuška and J. E. Osborn. Can a finite element method perform arbitrarily badly? *Mathematics of Computation*, 69(230):443–462, 2000. (Cited on page 67.)

I. Babuška. The finite element method for elliptic equations with discontinuous coefficients. *Computing*, 5(3):207–213, September 1970. (Cited on page 2.)

G. Backus and F. Gilbert. The resolving power of gross earth data. *Geophysical Journal of the Royal Astronomical Society*, 16(2):169–205, 1968. (Cited on page 36.)

G. Backus and F. Gilbert. Uniqueness in the inversion of inaccurate gross Earth data. *Philosophical Transactions of the Royal Society of London. Series A. Mathematical and Physical Sciences*, 266(1173):123–192, 1970. (Cited on page 36.)

J. Barnes and P. Hut. A hierarchical O(N log N) force-calculation algorithm. *Nature*, 324(6096):446–449, December 1986. (Cited on page 34.)

R. S. Barsoum. On the use of isoparametric finite elements in linear fracture mechanics. *International Journal for Numerical Methods in Engineering*, 10(1):25–37, 1976. (Cited on page 34.)

R. C. Batra, M. Porfiri, and D. Spinello. Treatment of material discontinuity in two meshless local Petrov–Galerkin (MLPG) formulations of axisymmetric transient heat conduction. *International Journal for Numerical Methods in Engineering*, 61(14):2461–2479, December 2004. (Cited on page 69.)

R. C. Batra, M. Porfiri, and D. Spinello. Free and Forced Vibrations of a Segmented Bar by a Meshless Local Petrov–Galerkin (MLPG) Formulation. *Computational Mechanics*, 41(4):473–491, December 2007. (Cited on page 69.)

T. Belytschko, Y. Y. Lu, and L. Gu. Element-free Galerkin methods. *International Journal for Numerical Methods in Engineering*, 37(2):229–256, January 1994. (Cited on pages 33, 36, and 69.)

M. Bennoune, J. Morin-Drouin, and R. G. Owens. On the jump conditions for an immersed interface method. *SIAM Journal on Scientific Computing*, 38(3):A1280–A1316, 2016. (Cited on page 32.)

M. N. Berdichevsky and V. I. Dmitriev. *Magnetotellurics in the context of the theory of ill-posed problems*. Society of Exploration Geophysicists, 2002. (Cited on pages 4, 5, and 6.)

M. N. Berdichevsky. Electrical prospecting by the method of magnetotelluric profiling. *Nedra, Moscow*, 140:153, 1968. (Cited on page 5.)

N. K. Bijan, B. Houshm, and T. Itoh. Fdtd analysis of dielectric resonators with curved surfaces. *IEEE Transactions on Microwave Theory and Techniques*, 45(9):1645 – 1649, 1997. (Cited on page 71.)

O. Biro and K. Preis. On the use of the magnetic vector potential in the finite-element analysis of three-dimensional eddy currents. *IEEE Transactions on magnetics*, 25(4):3145–3159, July 1989. (Cited on pages 13 and 14.)

O. Biro, K. Preis, and K. R. Richter. On the use of the magnetic vector potential in the nodal and edge finite element analysis of 3d magnetostatic problems. *IEEE Transactions on magnetics*, 32(3):651–654, 1996. (Cited on page 14.)

M. Bollhöfer and Y. Saad. Multilevel preconditioners constructed from inverse-based ilus. *SIAM Journal on Scientific Computing*, 27(5):1627–1650, 2006. (Cited on page 79.)

L. P. Bos and K. Šalkauskas. Moving least-squares are Backus-Gilbert optimal. *Journal of Approximation Theory*, 59(3):267–275, December 1989. (Cited on page 36.)

A. Bossavit. *Computational electromagnetism: variational formulations, complementarity, edge elements*. Academic Press, 1998. (Cited on page 25.)

A. Bossavit. On the lorenz gauge. *COMPEL-The international journal for computation and mathematics in electrical and electronic engineering*, 18(3):323–336, 1999. (Cited on pages 14 and 31.)

W. Boyse, D. Lynch, K. Paulsen, and G. Minerbo. Nodal-based finite-element modeling of Maxwell's equations. *IEEE Transactions on Antennas and Propagation*, 40(6):642–651, June 1992. (Cited on page 31.)

C. Brewitt-Taylor and J. Weaver. On the finite difference solution of two-dimensional induction problems. *Geophysical Journal International*, 47(2):375–396, 1976. (Cited on pages 1 and 87.)

R. Bridson. Fast poisson disk sampling in arbitrary dimensions. In *ACM SIGGRAPH 2007 Sketches*, SIGGRAPH '07, New York, NY, USA, 2007. ACM. (Cited on pages 75 and 76.)

C. Bryant, C. Emson, and C. Trowbridge. A general purpose 3d formulation for eddy currents using the lorentz gauge. *IEEE Transactions on Magnetics*, 26(5):2373–2375, 1990. (Cited on page 14.)

C. Bryant, C. Emson, C. Trowbridge, and P. Fernandes. Lorentz gauge formulations for eddy current problems involving piecewise homogeneous conductors. *IEEE Transactions on Magnetics*, 34(5):2559–2562, 1998. (Cited on page 14.)

L. Cagniard. Basic theory of the magneto-telluric method of geophysical prospecting. *Geophysics*, 18(3):605–635, 1953. (Cited on page 4.)

Y. Cai and H. Zhu. Direct imposition of essential boundary conditions and treatment of material discontinuities in the efg method. *Computational Mechanics*, 34(4):330–338, 2004. (Cited on page 68.)

V. Červ, O. Praus, and M. Hvoždara. Numerical modelling in laterally inhomogeneous geoelectrical structures. *Studia Geophysica et Geodaetica*, 22(1):74–81, 1978. (Cited on page 1.)

A. D. Chave and A. G. Jones. *The magnetotelluric method: Theory and practice*. Cambridge University Press, 2012. (Cited on pages 4, 6, 22, 29, and 30.)

J.-S. Chen, L. Wang, H.-Y. Hu, and S.-W. Chi. Subdomain radial basis collocation method for heterogeneous media. *International journal for numerical methods in engineering*, 80(2):163–190, 2009. (Cited on page 82.)

T. Chernogorova, R. Ewing, O. Iliev, and R. Lazarov. On finite volume discretzation of elliptic interface problem. In R. Herbin and D. Kroner, editors, *Finite Volumes for Complex Applications III*, pages 301 – 308. Hermes Penton Science, 2002. (Cited on page 70.)

P. W. Cleary and J. J. Monaghan. Conduction modelling using smoothed particle hydrodynamics. *Journal of Computational Physics*, 148(1):227–264, 1999. (Cited on page 70.)

J. H. Coggon. Electromagnetic and electrical modelling by the finite element method. *Geophysics*, 36:132–155, 1971. (Cited on pages 2 and 28.)

S. C. Constable, R. L. Parker, and C. G. Constable. Occam's inversion; a practical algorithm for generating smooth models from electromagnetic sounding data. *Geophysics*, 52(3):289–300, January 1987. (Cited on page 101.)

R. L. Cook. Stochastic Sampling in Computer Graphics. *ACM Trans. Graph.*, 5(1):51–72, January 1986. (Cited on page 74.)

L. W. Cordes and B. Moran. Treatment of material discontinuity in the Element-Free Galerkin method. *Computer Methods in Applied Mechanics and Engineering*, 139(1–4):75–89, December 1996. (Cited on page 69.)

O. Davydov and R. Schaback. Optimal stencils in sobolev spaces. *ArXiv e-prints*, November 2016. (Cited on page 73.)

A. B. de Castro, D. Gómez, and P. Salgado. *Mathematical models and numerical simulation in electromagnetism*, volume 74. Springer, 2014. (Cited on page 25.)

S. de la Kethulle de Ryhove and R. Mittet. 3d marine magnetotelluric modeling and inversion with the finite-difference time-domain method. *Geophysics*, 79(6):E269–E286, 2014. (Cited on page 11.)

C. Degroot and S. Constable. Occam's inversion to generate smooth, two-dimensional models from magnetotelluric data. *Geophysics*, 55(12):1613–1624, 1990. (Cited on pages 2 and 101.)

J. Dolbow and T. Belytschko. An introduction to programming the meshless element free galerkin method. *Archives of Computational Methods in Engineering*, 5(3):207–241, 1998. (Cited on page 56.)

J. Dolbow and T. Belytschko. A finite element method for crack growth without remeshing. *International journal for numerical methods in engineering*, 46(1):131–150, 1999. (Cited on page 33.)

Q. Du, M. Gunzburger, and L. Ju. Meshfree, probabilistic determination of point sets and support regions for meshless computing. *Computer Methods in Applied Mechanics and Engineering*, 191(13–14):1349–1366, January 2002. (Cited on page 73.)

D. Dunbar and G. Humphreys. A spatial data structure for fast Poisson-disk sample generation. In *ACM Transactions on Graphics (TOG)*, volume 25, pages 503–508. ACM, 2006. (Cited on page 75.)

M. S. Ebeida, M. A. Awad, X. Ge, A. H. Mahmoud, S. A. Mitchell, P. M. Knupp, and L.-Y. Wei. Improving spatial coverage while preserving the blue noise of point sets. *Computer-Aided Design*, 46:25–36, January 2014. (Cited on page 74.)

H. W. Engl, M. Hanke, and A. Neubauer. *Regularization of Inverse Problems*. Springer, 1996. (Cited on page 101.)

L. Eriksson. Generation of boundary-conforming grids around wing-body configurations using transfinite interpolation. *AIAA J*, 20(10):1313–1320, 1982. (Cited on page 77.)

M. E. Everett and A. Schultz. Geomagnetic induction in a heterogenous sphere: Azimuthally symmetric test computations and the response of an undulating 660-km discontinuity. *Journal of Geophysical Research*, 101(B2):2765, 1996. (Cited on page 2.)

Y. Fadaei and M. M. Moghadam. A greedy sparse meshless method for solving heat conduction problems. *Engineering with Computers*, 33(3):631–645, July 2017. (Cited on page 64.)

C. G. Farquharson and D. W. Oldenburg. Approximate sensitivities for the electromagnetic inverse problem. *Geophysical Journal International*, 126(1):235–252, July 1996. (Cited on page 103.)

R. Farwig. Multivariate interpolation of arbitrarily spaced data by moving least squares methods. *Journal of Computational and Applied Mathematics*, 16(1):79–93, September 1986. (Cited on page 35.)

R. Farwig. Rate of convergence of moving least squares interpolation methods: the univariate case. In *Progress in Approximation Theory*, pages 313–327. Academic Press, Boston, 1991. (Cited on page 35.)

G. E. Fasshauer. *Meshfree approximation methods with MATLAB*, volume 6. World Scientific, Singapore, 2007. (Cited on page 44.)

P. Fernandes. General approach to prove the existence and uniqueness of the solution in vector potential formulations of 3-d eddy current problems. *IEE Proceedings-Science, Measurement and Technology*, 142(4):299–306, 1995. (Cited on pages 13 and 14.)

M. Fleming, Y. Chu, B. Moran, T. Belytschko, Y. Lu, and L. Gu. Enriched element-free galerkin methods for crack tip fields. *International journal for numerical methods in engineering*, 40(8):1483–1504, 1997. (Cited on page 69.)

B. Fornberg and N. Flyer. Fast generation of 2-D node distributions for mesh-free PDE discretizations. *Computers & Mathematics with Applications*, 69(7):531–544, April 2015. (Cited on page 73.)

C. Franke and R. Schaback. Solving partial differential equations by collocation using radial basis functions. *Applied Mathematics and Computation*, 93(1):73–82, July 1998. (Cited on pages 35 and 48.)

A. Franke, R.-U. Börner, and K. Spitzer. Adaptive unstructured grid finite element simulation of two-dimensional magnetotelluric fields for arbitrary surface and seafloor topography. *Geophysical Journal International*, 171(1):71–86, October 2007. (Cited on pages 2 and 88.)

A. Franke-Börner. *Three-dimensional Finite Element Simulation of Magnetotelluric Fields on Unstructured Grids*. PhD thesis, Technischen Universität Bergakademie Freiberg, 2013. (Cited on pages 80, 81, 82, 83, 84, and 85.)

T.-P. Fries and T. Belytschko. The intrinsic xfem: a method for arbitrary discontinuities without additional unknowns. *International Journal for Numerical Methods in Engineering*, 68(13):1358–1385, 2006. (Cited on page 67.)

V. Girault and P.-A. Raviart. *Finite element methods for Navier-Stokes equations: theory and algorithms*, volume 5. Springer Science & Business Media, 2012. (Cited on pages 11, 13, and 24.)

Y. Gong, B. Li, and Z. Li. Immersed-Interface Finite-Element Methods for Elliptic Interface Problems with Nonhomogeneous Jump Conditions. *SIAM Journal on Numerical Analysis*, 46(1):472–495, January 2008. (Cited on page 32.)

M. Gonzalez Huici. *Accurate ground penetrating radar numerical modeling for automatic detection and recognition of antipersonnel landmines*. PhD thesis, Universität Bonn, 2013. (Cited on page 21.)

A. Grayver and T. Kolev. Large-scale 3D geoelectromagnetic modeling using parallel adaptive high-order finite element method. *Geophysics*, 80(6):E277–E291, August 2015. (Cited on page 2.)

W. Gropp, E. Lusk, and A. Skjellum. *Using MPI: portable parallel programming with the message-passing interface*, volume 1. MIT press, 1999. (Cited on page 34.)

E. Haber and D. Oldenburg. A gcv based method for nonlinear ill-posed problems. *Computational Geosciences*, 4(1):41–63, 2000. (Cited on pages 102 and 103.)

E. Haber, U. M. Ascher, D. A. Aruliah, and D. W. Oldenburg. Fast Simulation of 3D Electromagnetic Problems Using Potentials. *Journal of Computational Physics*, 163(1):150–171, September 2000. (Cited on page 21.)

P. C. Hansen. *Rank-Deficient and Discrete Ill-Posed Problems*. Siam - Society for Industrial and Applied Mathematics, Philadelphia, 1998. (Cited on page 101.)

C. Herault and Y. Marechal. Boundary and interface conditions meshless methods [for EM field analysis]. *Magnetics, IEEE Transactions on*, 35(3):1450–1453, 1999. (Cited on page 67.)

P. G. Huray. *Maxwell's equations*. John Wiley & Sons, Ltd, 2011. (Cited on page 11.)

M. M. Idemen. *Discontinuities in the electromagnetic field*. John Wiley & Sons, 2011. (Cited on page 17.)

A. Iske. Optimal Distribution of Centers for Radial Basis Function Methods. Technical report, Technische Universitat München, 2000. (Cited on page 73.)

A. Iske. *Multiresolution methods in scattered data modelling*. Springer, 2004. (Cited on page 73.)

J. Jackson. *Classical Electrodynamics*. Willey, Berkeley, 3 edition, 1999. (Cited on page 10.)

J. D. Jackson. From lorenz to coulomb and other explicit gauge transformations. *American Journal of Physics*, 70(9):917–928, 2002. (Cited on page 14.)

Y. Ji, T. Huang, W. Huang, and L. Rong. Meshfree method in geophysical electromagnetic prospecting: The 2d magnetotelluric example. *International Journal of Computational Methods*, page 1750084, 2017. (Cited on page 2.)

J.-M. Jin. *The finite element method in electromagnetics*. John Wiley & Sons, 2015. (Cited on page 20.)

T. R. Jones and D. R. Karger. Linear-Time Poisson-Disk Patterns. *Journal of Graphics, GPU, and Game Tools*, 15(3):177–182, October 2011. (Cited on page 75.)

F. Jones and L. Pascoe. A general computer program to determine the perturbation of alternating electric currents in a two-dimensional model of a region of uniform conductivity with an embedded inhomogeneity. *Geophysical Journal International*, 24(1):3–30, 1971. (Cited on page 1.)

T. R. Jones. Efficient generation of Poisson-disk sampling patterns. *Journal of Graphics, GPU, and Game Tools*, 11(2):27–36, 2006. (Cited on page 75.)

P. Joyot, J. Trunzler, and F. Chinesta. Enriched reproducing kernel approximation: Reproducing functions with discontinuous derivatives. In *Meshfree Methods for Partial Differential Equations II*, volume 43, page 93. Springer Science & Business Media, 2006. (Cited on page 69.)

D. L. B. Jupp and K. Vozoff. Two-dimensional magnetotelluric inversion. *Geophysical Journal International*, 50(2):333–352, January 1977. (Cited on pages 103 and 106.)

K. Key and J. Ovall. A parallel goal-oriented adaptive finite element method for 2.5-D electromagnetic modelling. *Geophysical Journal International*, 186(1):137–154, 2011. (Cited on page 2.)

K. Key. Mare2dem: a 2-d inversion code for controlled-source electromagnetic and magnetotelluric data. *Geophysical Journal International*, 207(1):571–588, 2016. (Cited on page 2.)

D. W. Kim, W. K. Liu, Y.-C. Yoon, T. Belytschko, and S.-H. Lee. Meshfree point collocation method with intrinsic enrichment for interface problems. *Computational Mechanics*, 40(6):1037–1052, August 2007. (Cited on page 69.)

A. Kirsch and F. Hettlich. The mathematical theory of time-harmonic maxwell's equations. In *Applied Mathematical Sciences*, volume 190. Springer, 2015. (Cited on page 20.)

E. Kisak and P. Silvester. A finite-element program package for magnetotelluric modelling. *Computer Physics Communications*, 10(6):421–433, 1975. (Cited on pages 2 and 87.)

J. Kopf, D. Cohen-Or, O. Deussen, and D. Lischinski. *Recursive Wang tiles for real-time blue noise*, volume 25. ACM, 2006. (Cited on page 74.)

M. Kordy, E. Cherkaev, and P. Wannamaker. Variational formulation for maxwell's equations with lorenz gauge: Existence and uniqueness of solution. *Int. J. Numer. Anal. Model*, 12(4):731–749, 2015. (Cited on page 14.)

M. A. Kordy. *Efficient computational methods for electromagnetic imaging with applications to 3D magnetotellurics*. PhD thesis, The University of Utah, 2014. (Cited on page 14.)

E. Kriezis, T. Tsiboukis, S. Panas, and J. Tegopoulos. Eddy currents: theory and applications. *Proceedings of the IEEE*, 80(10):1559–1589, October 1992. (Cited on page 26.)

A. Lagae and P. Dutré. A Comparison of Methods for Generating Poisson Disk Distributions. *Computer Graphics Forum*, 27(1):114–129, 2008. (Cited on page 75.)

P. Lancaster and K. Šalkauskas. Surfaces generated by moving least squares methods. *Mathematics of Computation*, 37(155):141–158, 1981. (Cited on page 35.)

P. G. Lelièvre and C. G. Farquharson. Gradient and smoothness regularization operators for geophysical inversion on unstructured meshes. *Geophysical Journal International*, 195(1):330–341, 2013. (Cited on page 107.)

R. J. Leveque and Z. Li. The immersed interface method for elliptic equations with discontinuous coefficients and singular sources. *SIAM Journal on Numerical Analysis*, 31(4):1019–1044, 1994. (Cited on page 70.)

D. Levin. The approximation power of moving least-squares. *Mathematics of Computation of the American Mathematical Society*, 67(224):1517–1531, 1998. (Cited on pages 36 and 37.)

D. Levin. Stable integration rules with scattered integration points. *Journal of Computational and Applied Mathematics*, 112(1–2):181–187, November 1999. (Cited on pages 36 and 107.)

Z. Li and K. Ito. *The Immersed Interface Method: Numerical Solutions of PDEs Involving Interfaces and Irregular Domains*. Frontiers in Applied Mathematics. Society for Industrial and Applied Mathematics, 2006. (Cited on page 32.)

Y. Li and K. Key. 2D marine controlled-source electromagnetic modeling: Part 1 — An adaptive finite-element algorithm. *Geophysics*, 72(2):WA51–WA62, January 2007. (Cited on page 2.)

S. Li and W. K. Liu. *Meshfree particle methods*. Springer Science & Business Media, 2007. (Cited on page 34.)

J.-J. Li, J.-B. Yan, and X.-Y. Huang. Precision of meshfree methods and application to forward modeling of two-dimensional electromagnetic sources. *Applied Geophysics*, 12(4):503–515, 2015. (Cited on page 2.)

M. Liu, G. Liu, and K. Lam. A one-dimensional meshfree particle formulation for simulating shock waves. *Shock Waves*, 13(3):201–211, 2003. (Cited on page 70.)

D. Livelybrooks. Program 3Dfeem: a multidimensional electromagnetic finite element model. *Geophysical Journal International*, 114(3):443–458, September 1993. (Cited on page 28.)

P. P. D. Lugão and P. E. Wannamaker. Calculating the two-dimensional magnetotelluric Jacobian in finite elements using reciprocity. *Geophysical Journal International*, 127(3):806–810, January 1996. (Cited on pages 103 and 104.)

P. P. D. Lugão, O. Portniaguine, and M. S. Zhdanov. Fast and Stable Two-Dimensional Inversion of Magnetotelluric Data. *Journal of geomagnetism and geoelectricity*, 49(11-12):1469–1497, 1997. (Cited on pages 103 and 104.)

T. G. Mackay and A. Lakhtakia. *Electromagnetic anisotropy and bianisotropy: a field guide*. World Scientific Pub. Co, 2010. (Cited on page 9.)

R. L. Mackie, T. R. Madden, and P. E. Wannamaker. Three-dimensional magnetotelluric modeling using difference equations - Theory and comparisons to integral equation solutions. *Geophysics*, 58:215–226, 1993. (Cited on page 2.)

R. L. Mackie, J. T. Smith, and T. R. Madden. Three-dimensional electromagnetic modeling using finite difference equations: The magnetotelluric example. *Radio Science*, 29(04):923–935, 1994. (Cited on pages 2, 93, 94, 95, and 98.)

J. C. Mairhuber. On haar's theorem concerning chebychev approximation problems having unique solutions. *Proceedings of the American Mathematical Society*, 7(4):609–615, 1956. (Cited on page 35.)

M. C. Marcysiak and W. K. Gwarek. Higher-order modelling of media interfaces for enhanced fdtd analysis of microwave circuits. In *Microwave Conference, 1994. 24th European*, volume 2, pages 1530–1535. IEEE, 1994. (Cited on page 71.)

M. McCool and E. Fiume. Hierarchical Poisson Disk Sampling Distributions. In *Proceedings of the Conference on Graphics Interface '92*, pages 94–105. Morgan Kaufmann Publishers Inc., 1992. (Cited on page 75.)

E. Medeiros, L. Ingrid, S. Pesco, and C. Silva. Fast adaptive blue noise on polygonal surfaces. *Graphical Models*, 76(1):17–29, 2014. (Cited on page 75.)

W. Menke. *Geophysical Data Analysis: Discrete Inverse Theory*. Academic Press Inc, 1984. (Cited on page 99.)

M. P. Miensopust. *Multidimensional magnetotellurics: A 2D case study and a 3D approach to simultaneously invert for resistivity structure and distortion parameters*. PhD thesis, Department of Earth and Ocean Sciences National University Ireland, 2010. (Cited on page 7.)

D. Mirzaei and K. Hasanpour. Direct meshless local petrov-galerkin method for elastodynamic analysis. *Acta Mechanica*, 227(3):619–632, 2016. (Cited on page 36.)

D. Mirzaei and R. Schaback. Direct Meshless Local Petrov–Galerkin (DMLPG) method: A generalized MLS approximation. *Applied Numerical Mathematics*, 68:73–82, June 2013. (Cited on pages 36, 37, 46, 48, 54, 58, and 62.)

D. Mirzaei and R. Schaback. Solving heat conduction problems by the Direct Meshless Local Petrov-Galerkin (DMLPG) method. *Numerical Algorithms*, 65(2):275–291, February 2014. (Cited on pages 36 and 48.)

D. Mirzaei, R. Schaback, and M. Dehghan. On generalized moving least squares and diffuse derivatives. *IMA Journal of Numerical Analysis*, 32(3):983–1000, January 2012. (Cited on pages 36, 37, 39, 40, 43, 44, 48, and 57.)

D. Mirzaei. Analysis of moving least squares approximation revisited. *Journal of Computational and Applied Mathematics*, 282:237–250, 2015. (Cited on page 31.)

D. Mirzaei. A new low-cost meshfree method for two and three dimensional problems in elasticity. *Applied Mathematical Modelling*, July 2015. (Cited on page 36.)

D. Mirzaei. Error bounds for gmls derivatives approximations of sobolev functions. *Journal of Computational and Applied Mathematics*, 294:93–101, 2016. (Cited on pages 43, 44, 45, and 46.)

T. Mogi. Three-dimensional modeling of magnetotelluric data using finite element method. *Journal of Applied Geophysics*, 35(2–3):185–189, September 1996. (Cited on page 2.)

S. Moskow, V. Druskin, T. Habashy, P. Lee, and S. Davydycheva. A finite difference scheme for elliptic equations with rough coefficients using a cartesian grid nonconforming to interfaces. *SIAM Journal on Numerical Analysis*, 36(2):442–464, 1998. (Cited on page 72.)

V. Namias. Discontinuity of the electromagnetic fields, potentials, and currents at fixed and moving boundaries. *American Journal of Physics*, 56(10):898–904, 1988. (Cited on pages 17 and 18.)

B. Nayroles, G. Touzot, and P. Villon. Generalizing the finite element method: Diffuse approximation and diffuse elements. *Computational Mechanics*, 10(5):307–318, September 1992. (Cited on page 36.)

J. C. Nedelec. Mixed finite elements in $\mathbb{R}3$. *Numerische Mathematik*, 35(3):315–341, September 1980. (Cited on page 2.)

V. P. Nguyen, T. Rabczuk, S. Bordas, and M. Duflot. Meshless methods: A review and computer implementation aspects. *Mathematics and Computers in Simulation*, 79(3):763–813, December 2008. (Cited on page 34.)

Y. Nie, W. Zhang, N. Qi, and Y. Li. Parallel node placement method by bubble simulation. *Computer Physics Communications*, 185(3):798–808, 2014. (Cited on page 73.)

H. Niederreiter. *Random Number Generation and Quasi-Monte Carlo Methods*. Society for Industrial and Applied Mathematics, 1992. (Cited on page 74.)

E. Oñate, S. Idelsohn, O. C. Zienkiewicz, and R. L. Taylor. A Finite Point Method in Computational Mechanics. Applications to Convective Transport and Fluid Flow. *International Journal for Numerical Methods in Engineering*, 39(22):3839–3866, November 1996. (Cited on page 48.)

S. Osher and R. Fedkiw. *Level set methods and dynamic implicit surfaces*, volume 153. Springer Science & Business Media, 2006. (Cited on page 17.)

S. J. Owen. A survey of unstructured mesh generation technology. In *7th International Meshing Roundtable*, pages 239–267, 1998. (Cited on page 34.)

H. Owhadi and L. Zhang. Localized bases for finite-dimensional homogenization approximations with nonseparated scales and high contrast. *Multiscale Modeling & Simulation*, 9(4):1373–1398, 2011. (Cited on page 67.)

C. C. Paige and M. A. Saunders. Algorithm 583: Lsqr: Sparse linear equations and least squares problems. *ACM Trans. Math. Softw.*, 8(2):195–209, June 1982. (Cited on page 103.)

G. J. Palacky. Resistivity characteristics of geologic targets. In *Electromagnetic Methods in Applied Geophysics: Volume 1, Theory*, pages 52–129. Society of Exploration Geophysicists, 1988. (Cited on pages 6 and 7.)

J. Pek and T. Verner. Finite-difference modelling of magnetotelluric fields in two-dimensional anisotropic media. *Geophysical Journal International*, 128(3):505–521, 1997. (Cited on page 2.)

C. S. Peskin. The immersed boundary method. *Acta Numerica*, 11:479–517, 2002. (Cited on page 32.)

J. Peypouquet. *Convex optimization in normed spaces: theory, methods and examples*. Springer, 2015. (Cited on page 40.)

S. Plimpton. Fast Parallel Algorithms for Short-Range Molecular Dynamics. *Journal of Computational Physics*, 117(1):1–19, March 1995. (Cited on page 34.)

P. Przybyszewski. *Fast finite difference numerical techniques for the time and frequency domain solution of electromagnetic problems*. PhD thesis, Technical University of Gdansk, 2001. (Cited on page 71.)

M. Ramezani, M. Mojtabaei, and D. Mirzaei. DMLPG solution of the fractional advection–diffusion problem. *Engineering Analysis with Boundary Elements*, 59:36–42, October 2015. (Cited on page 36.)

S. Rätz. *Ein dreidimensionales Finite Elemente Programm zur Simulation elektromagnetischer Oberflächen- und Bohrlochverfahren*. PhD thesis, Institut f. Geophysik und Meteorologie, Universität zu Köln, 2000. (Cited on page 28.)

H. Ren, K. Pei, and L. Wang. Error analysis for moving least squares approximation in 2D space. *Applied Mathematics and Computation*, 238:527–546, July 2014. (Cited on page 44.)

T. Rikitake. Note on the electromagnetic induction within the earth. *Bull. Earthq. Res. Inst., Univ. Tokyo*, (24):1–9, 1948. (Cited on page 4.)

W. Rodi and R. L. Mackie. Nonlinear conjugate gradients algorithm for 2-D magnetotelluric inversion. *Geophysics*, 66(1):174–187, 2001. (Cited on page 103.)

W. L. Rodi. A Technique for Improving the Accuracy of Finite Element Solutions for Magnetotelluric Data. *Geophysical Journal International*, 44(2):483–506, January 1976. (Cited on pages 2 and 103.)

Y. Saad. On the condition number of some gram matrices arising from least squares approximation in the complex plane. *Numerische Mathematik*, 48(3):337–347, 1986. (Cited on page 57.)

M. Sadiku. *Numerical Techniques in Electromagnetics, Second Edition*. Taylor & Francis, 2000. (Cited on page 48.)

R. Salehi and M. Dehghan. A generalized moving least square reproducing kernel method. *Journal of Computational and Applied Mathematics*, 249:120–132, September 2013. (Cited on pages 36 and 40.)

K. Šalkauskas. Moving least squares interpolation with thin-plate splines and radial basis functions. *Computers & Mathematics with Applications*, 24(12):177–185, 1992. (Cited on page 36.)

A. A. Samarskii. *The theory of difference schemes*, volume 240. CRC Press, 2001. (Cited on page 70.)

J. E. Santos and D. Sheen. On the existence and uniqueness of solutions to maxwell's equations in bounded domains with application to magnetotellurics. *Mathematical Models and Methods in Applied Sciences*, 10(04):615–628, 2000. (Cited on pages 9 and 20.)

R. Schaback and H. Wendland. Using compactly supported radial basis functions to solve partial differential equations. *WIT Transactions on Modelling and Simulation*, 22:311–324, 1999. (Cited on page 47.)

R. Schaback. Direct discretizations with applications to meshless methods for pdes. *Proceedings of DWCAA12*, 6:37–50, 2013. (Cited on page 46.)

R. Schaback. Greedy sparse linear approximations of functionals from nodal data. *Numerical Algorithms*, 67(3):531–547, November 2014. (Cited on pages 64 and 73.)

R. Schaback. Error analysis of nodal meshless methods. In M. S. M. Griebel, editor, *Meshfree Methods for Partial Differential Equations VIII*, volume 115 of *Lecture Notes in Computational Science and Engineering*, pages 117–143. Springer, 2017. (Cited on page 47.)

K. Schwalenberg and R. N. Edwards. The effect of seafloor topography on magnetotelluric fields: an analytical formulation confirmed with numerical results. *Geophysical Journal International*, 159(2):607–621, November 2004. (Cited on pages vii, viii, 78, 79, 88, 89, 90, 91, 92, 97, 140, 141, 142, 143, 144, and 145.)

C. Schwarzbach and E. Haber. Finite element based inversion for time-harmonic electromagnetic problems. *Geophysical Journal International*, 193(2):615–634, 2013. (Cited on pages 2, 103, and 107.)

C. Schwarzbach. *Stability of finite element solutions to Maxwell's equations in frequency domain*. PhD thesis, TU Bergakademie Freiberg, 2009. (Cited on page 2.)

M. A. Schweitzer and S. Wu. A moving least squares approach to the construction of discontinuous enrichment functions. In *Singular Phenomena and Scaling in Mathematical Models*, pages 347–360. Springer, 2014. (Cited on page 69.)

B. Seibold. *M-Matrices in meshless finite difference methods*. PhD thesis, Technische Universität Kaiserslautern, 2006. (Cited on pages 48 and 73.)

J. A. Sethian. *Level set methods and fast marching methods: evolving interfaces in computational geometry, fluid mechanics, computer vision, and materials science*, volume 3. Cambridge university press, 1999. (Cited on page 70.)

D. Shepard. A two-dimensional interpolation function for irregularly-spaced data. pages 517–524. ACM Press, 1968. (Cited on page 35.)

K. Shimada and D. C. Gossard. Bubble mesh: Automated triangular meshing of non-manifold geometry by sphere packing. In *Proceedings of the Third ACM Symposium on Solid Modeling and Applications*, SMA '95, pages 409–419. ACM, 1995. (Cited on page 73.)

A. Sihvola. Lorenz-lorentz or lorentz-lorenz? *IEEE Antennas and Propagation Magazine*, 33(4), 1991. (Cited on page 14.)

F. Simpson and K. Bahr. *Practical magnetotellurics*. Cambridge University Press, 2005. (Cited on pages 4 and 5.)

S. Srivastava. Method of interpretation of magnetotelluric data when source field is considered. *Journal of Geophysical Research*, 70(4):945–954, 1965. (Cited on page 27.)

A. Taleei and M. Dehghan. Direct meshless local Petrov–Galerkin method for elliptic interface problems with applications in electrostatic and elastostatic. *Computer Methods in Applied Mechanics and Engineering*, June 2014. (Cited on pages 36 and 68.)

A. Taleei and M. Dehghan. An efficient meshfree point collocation moving least squares method to solve the interface problems with nonhomogeneous jump conditions. *Numerical Methods for Partial Differential Equations*, pages 1031–1053, 2014. (Cited on page 68.)

A. N. Tikhonov and V. Y. Aesenin. *Solution of ill-posed problems*. V. H. Winston and V. H. Winston and Sons, 1977. (Cited on page 101.)

A. N. Tikhonov and A. A. Samarskii. Homogeneous difference schemes. *USSR Computational Mathematics and Mathematical Physics*, 1(1):5–67, 1962. (Cited on page 69.)

A. N. Tikhonov. On determining electrical characteristics of the deep layers of the earth's crust. *Dokl. Acad. Nauk SSSR*, 151(2):295–297, 1950. (Cited on page 4.)

S. C. Ting and G. W. Hohmann. Integral equation modeling of three-dimensional magnetotelluric response. *Geophysics*, 46(2):182–197, 1981. (Cited on page 2.)

N. Trask, M. Maxey, and X. Hu. A compatible high-order meshless method for the stokes equations with applications to suspension flows. *arXiv preprint arXiv:1611.03911*, 2016. (Cited on pages 43 and 57.)

N. Trask, M. Perego, and P. Bochev. A high-order staggered meshless method for elliptic problems. *SIAM Journal on Scientific Computing*, 39(2):A479–A502, 2017. (Cited on pages 36, 41, 42, 43, 45, 61, 70, 82, and 88.)

R. H. Tyler, F. Vivier, and S. Li. Three-dimensional modelling of ocean electrodynamics using gauged potentials. *Geophysical Journal International*, 158(3):874–887, January 2004. (Cited on pages 11 and 15.)

L. Verlet. Computer "experiments" on classical fluids. i. thermodynamical properties of lennard-jones molecules. *Phys. Rev.*, 159:98–103, July 1967. (Cited on page 76.)

K. Vozoff. The magnetotelluric method. In *Electromagnetic Methods in Applied Geophysics: Volume 2, Application, Parts A and B*, pages 641–712. Society of Exploration Geophysicists, 1991. (Cited on page 5.)

J. R. Wait. Propagation of Radio Waves over a Stratified Ground. *Geophysics*, 20:416–422, 1953. (Cited on pages 23 and 81.)

P. E. Wannamaker, G. W. Hohmann, and S. H. Ward. Magnetotelluric responses of three-dimensional bodies in layered earths. *Geophysics*, 49(9):1517–1533, 1984. (Cited on page 2.)

P. Wannamaker, J. A. Stodt, and L. Rijo. PW2D - Finite Element Program for solution of magnetotelluric response of two-dimensional earth resistivity structure. Technical report, University of Utah, 1985. (Cited on pages 2, 28, 76, 85, and 114.)

S. H. Ward and G. W. Hohmann. Electromagnetic theory for geophysical applications. In *Electromagnetic methods in applied geophysics*, volume 1, pages 131–311, 1988. (Cited on page 18.)

J. Weaver, B. Le Quang, and G. Fischer. A comparison of analytic and numerical results for a two-dimensional control model in electromagnetic induction–i. b-polarization calculations. *Geophysical Journal International*, 82(2):263–277, 1985. (Cited on pages vi, 86, 87, 88, and 97.)

J. T. Weaver, B. V. LeQuang, and G. Fischer. A comparison of analytical and numerical results for a 2-d control model in electromagnetic induction - ii. e-polarization calculations. *Geophysical Journal of the Royal Astronomical Society*, 87(3):917–948, 1986. (Cited on pages vi, vii, 86, 87, 88, and 97.)

L.-Y. Wei. Parallel Poisson Disk Sampling. In *ACM SIGGRAPH 2008 Papers*, pages 20:1–20:9. ACM, 2008. (Cited on page 75.)

P. Weidelt. Electromagnetic induction in three-dimensional structures. *J. Geophys*, 41(85):109, 1975. (Cited on page 2.)

C. J. Weiss and G. A. Newman. Electromagnetic induction in a fully 3-d anisotropic earth. *Geophysics*, 67(4):1104–1114, 2002. (Cited on page 2.)

C. J. Weiss. Project APhiD: A Lorenz-gauged A-phi decomposition for parallelized computation of ultra-broadband electromagnetic induction in a fully heterogeneous Earth. *Computers & Geosciences*, 58:40–52, August 2013. (Cited on page 15.)

H. Wendland. Local polynomial reproduction and moving least squares approximation. *IMA Journal of Numerical Analysis*, 21(1):285–300, 2001. (Cited on page 44.)

H. Wendland. *Scattered Data Approximation*. Cambridge University Press, 2010. (Cited on pages 40, 43, 44, 57, and 58.)

B. Wheelock, S. Constable, and K. Key. The advantages of logarithmically scaled data for electromagnetic inversion. *Geophysical Journal International*, 201(3):1765–1780, January 2015. (Cited on page 106.)

J. Wittke and B. Tezkan. Meshfree magnetotelluric modelling. *Geophysical Journal International*, 198(2):1255–1268, January 2014. (Cited on pages 2, 46, 48, 52, 54, 79, and 80.)

F. Xu, Y. Zhao, R. Yan, and T. Furukawa. Multidimensional discontinuous sph method and its application to metal penetration analysis. *International Journal for Numerical Methods in Engineering*, 93(11):1125–1146, 2013. (Cited on page 70.)

K. Yee. Numerical solution of initial boundary value problems involving maxwell's equations in isotropic media. *IEEE Transactions on antennas and propagation*, 14(3):302–307, 1966. (Cited on page 2.)

Y.-C. Yoon, S.-H. Lee, and T. Belytschko. Enriched meshfree collocation method with diffuse derivatives for elastic fracture. *Computers & Mathematics with Applications*, 51(8):1349–1366, April 2006. (Cited on page 69.)

M. S. Zhdanov. Methods in geochemistry and geophysics. In *Geophysical Inverse Theory and Regularization Problems*, volume 36 of *Methods in Geochemistry and Geophysics*. Elsevier, 2002. (Cited on page 99.)

M. S. Zhdanov. *Geophysical electromagnetic theory and methods*. Number 43 in Methods in Geochemistry and Geophysics. Elsevier Amsterdam, Amsterdam, 2009. (Cited on page 13.)

C. Zuppa. Error estimates for moving least square approximations. *Bulletin of the Brazilian Mathematical Society*, 34(2):231–249, July 2003. (Cited on page 44.)

F. I. Zyserman and J. E. Santos. Parallel finite element algorithm with domain decomposition for three-dimensional magnetotelluric modelling. *Journal of Applied Geophysics*, 44(4):337–351, July 2000. (Cited on page 2.)

F. I. Zyserman, L. Guarracino, and J. E. Santos. A hybridized mixed finite element domain decomposed method for two dimensional magnetotelluric modelling. *Earth, planets and space*, 51(4):297–306, 1999. (Cited on page 20.)

Appendix

A.1 Mathematical function spaces

In this section the function spaces used in this thesis will be defined, and declared. $C^0(\Omega)$ denotes the space of all continuous functions in Ω equipped with the norm

$$||u||_{C^0(\Omega)} = \sup_{x\in\Omega} |u(x)|. \tag{A.1}$$

$C^k(\Omega)$ denotes the space of all k-times continuous functions in Ω equipped and is defined as

$$C^k(\Omega) = \left\{u \in C^0(\Omega); \partial^\alpha u \in C^0(\Omega), \quad \forall|\alpha| \leq k\right\}. \tag{A.2}$$

$L^p(\Omega)$ is the space for all Lebesgue measurable functions $u : \Omega \to \mathbb{R}$, for which $||u||_{L^p(\Omega)} < \infty$, with the $L^p(\Omega)$-norms

$$||u||_{L^p(\Omega)} = \begin{cases} \left(\int_\Omega |u|^p \, dx\right)^{1/p} & \text{for } p < \infty \\ \text{ess sup}_{x\in\Omega} |u(x)| & \text{for } p = \infty \end{cases}. \tag{A.3}$$

$W_p^k(\Omega)$ is a Sobolev Space

$$W_p^k(\Omega) = \{u \in L^p(\Omega); \partial^\alpha u \in L^p(\Omega), \quad \forall|\alpha| \leq k\}, \tag{A.4}$$

equipped with the $W_p^k(\Omega)$-norms

$$||u||_{W_p^k(\Omega)} = \begin{cases} \left(\sum_{|\alpha|\leq k} \int_\Omega |\partial^\alpha u|^p \, dx\right)^{1/p}, & \text{for } p < \infty \\ \max_{|\alpha|\leq k} \left(\text{ess sup}_{x\in\Omega} |\partial^\alpha u(x)|\right), & \text{for } p = \infty \end{cases}. \tag{A.5}$$

A.2 Point samplings

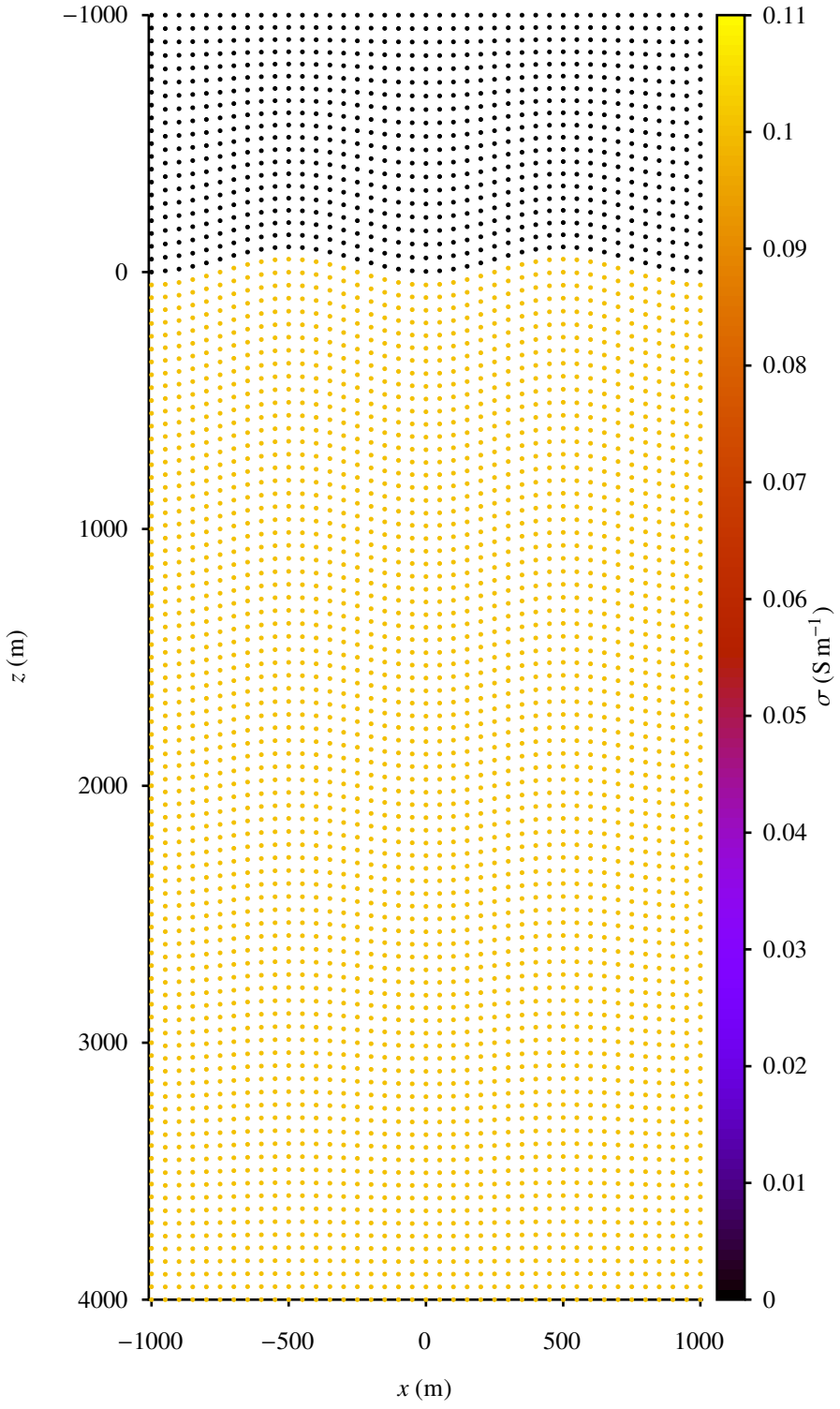

Figure A.50: Regular point sampling for the model of Schwalenberg and Edwards (2004) with an amplitude of $\triangle = 50\text{m}$*, used for the calculations in Chapter 3.8.*

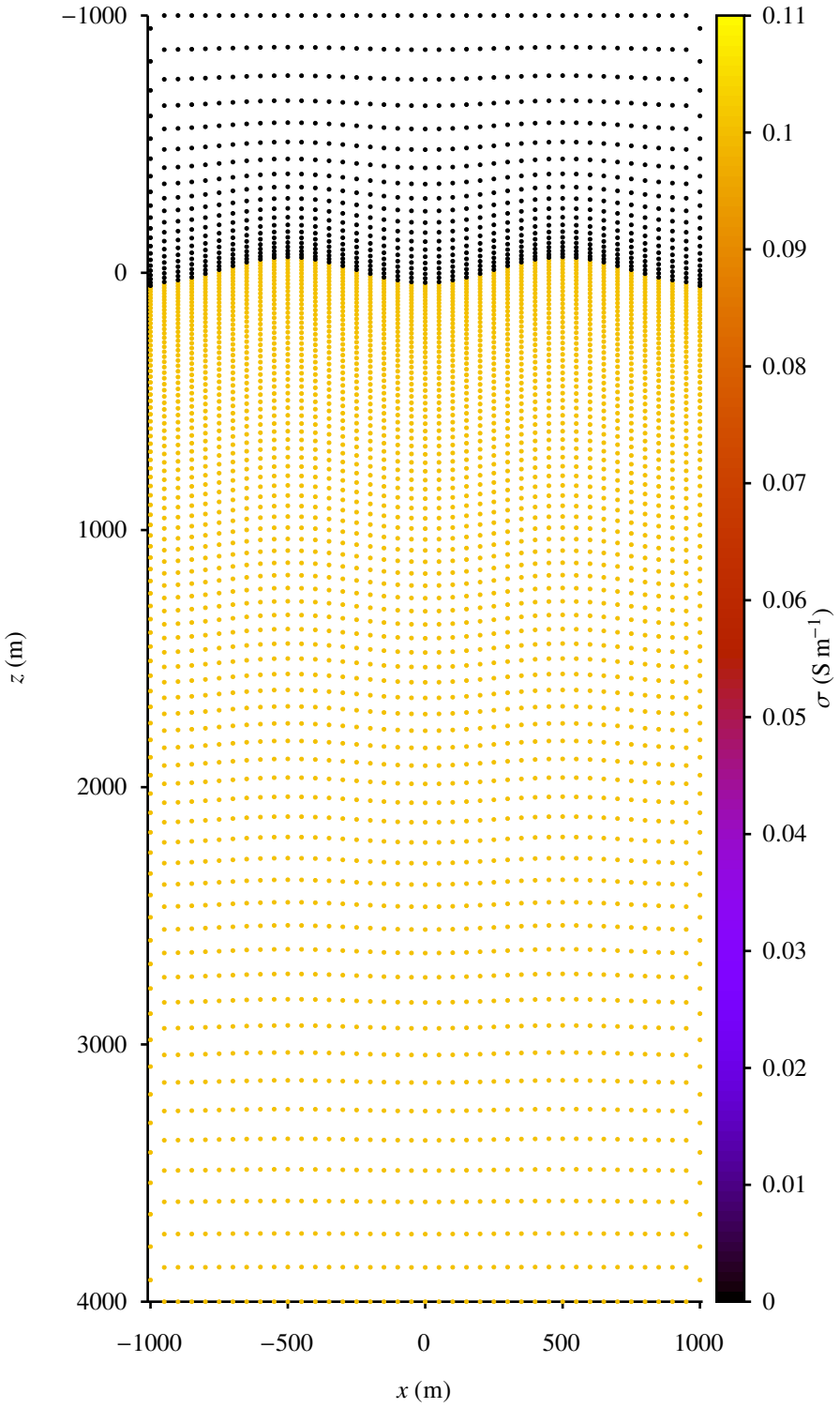

Figure A.51: Spatial adapted regular point sampling for the model of Schwalenberg and Edwards (2004) with an amplitude of $\triangle = 50\text{m}$*, used for the calculations in Chapter 3.8.*

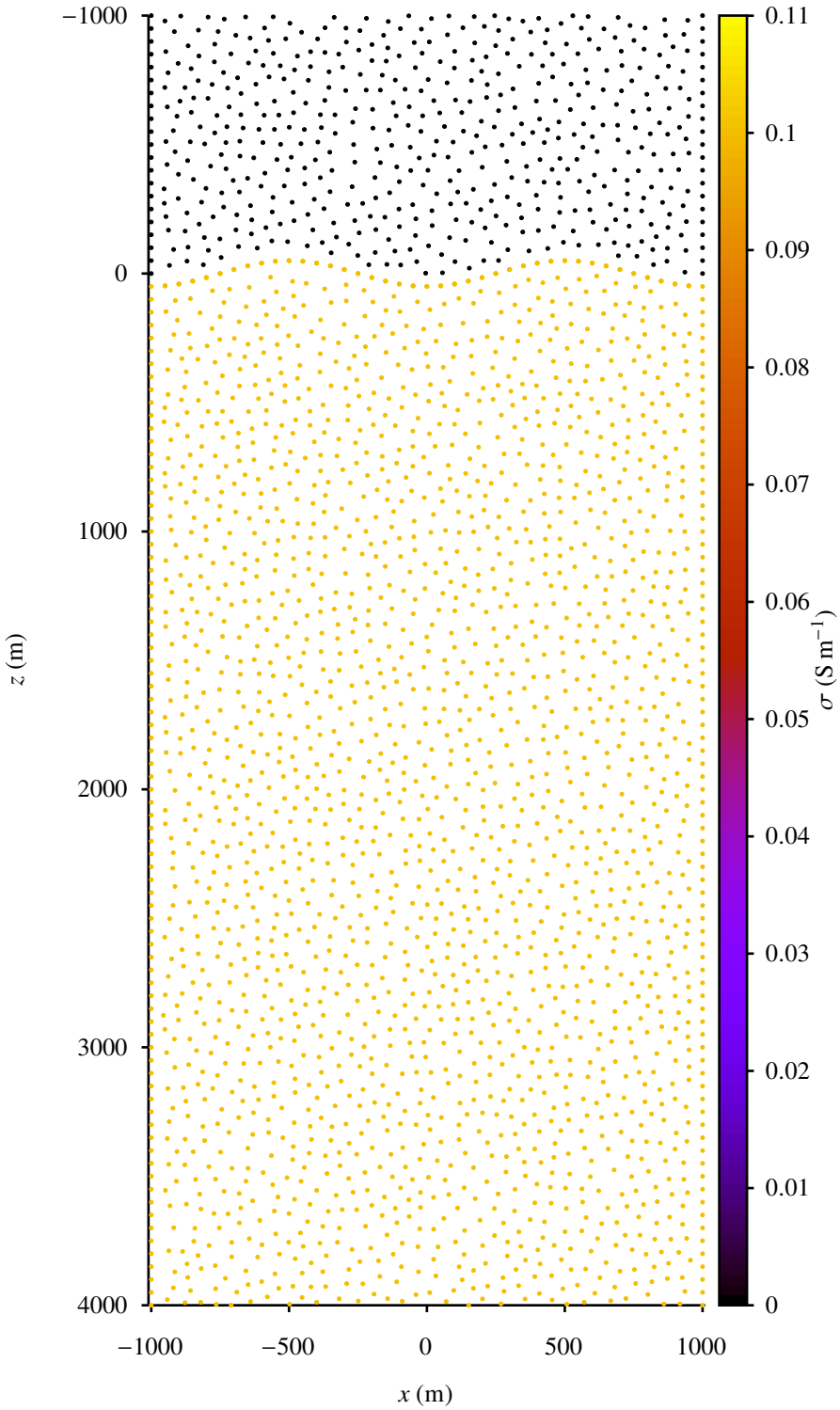

Figure A.52: Spatial adapted regular point sampling for the model of Schwalenberg and Edwards (2004) with an amplitude of $\triangle = 50\text{m}$*, used for the calculations in Chapter 3.8.*

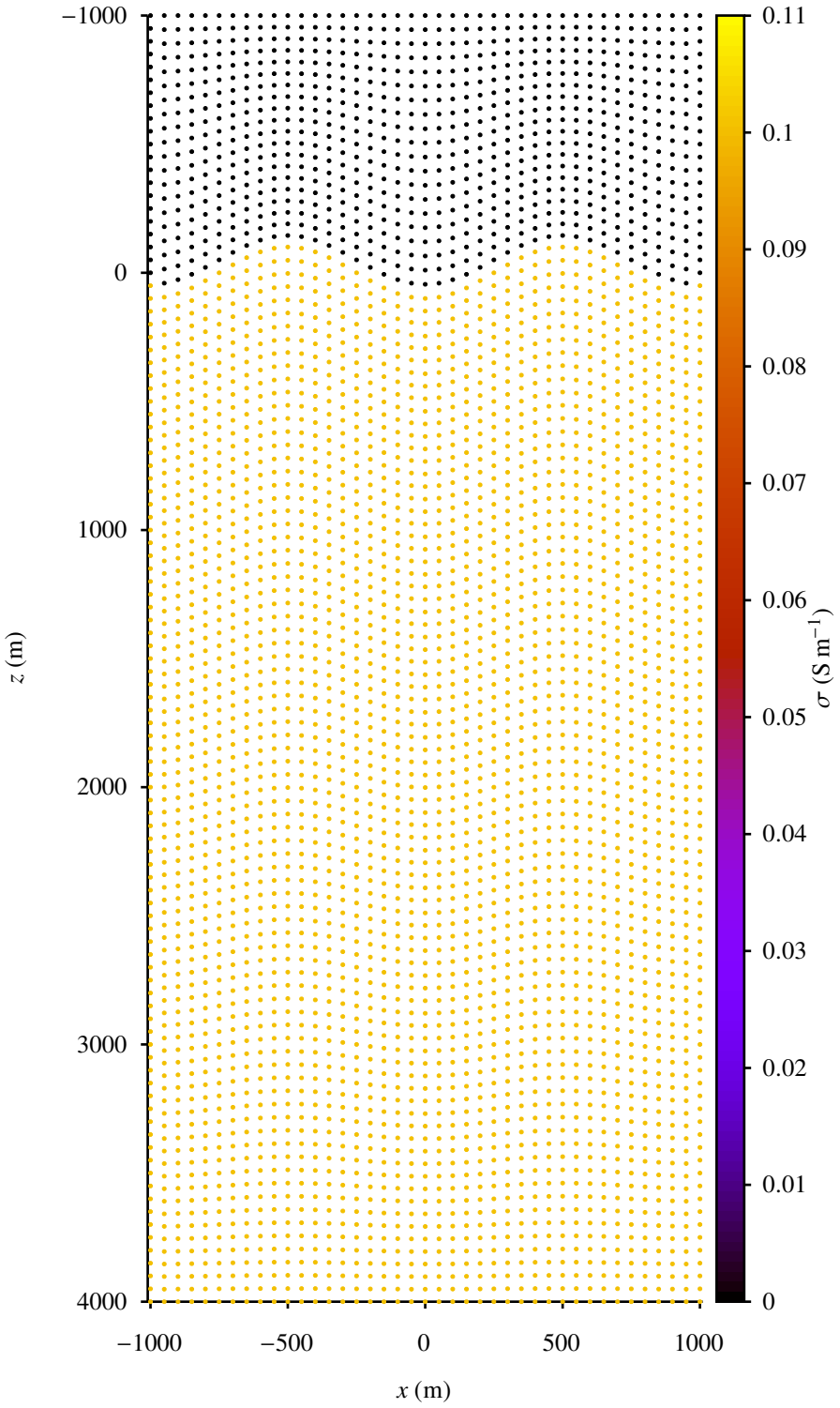

Figure A.53: Regular point sampling for the model of Schwalenberg and Edwards (2004) with an amplitude of $\triangle = 100\text{m}$*, used for the calculations in Chapter 3.8.*

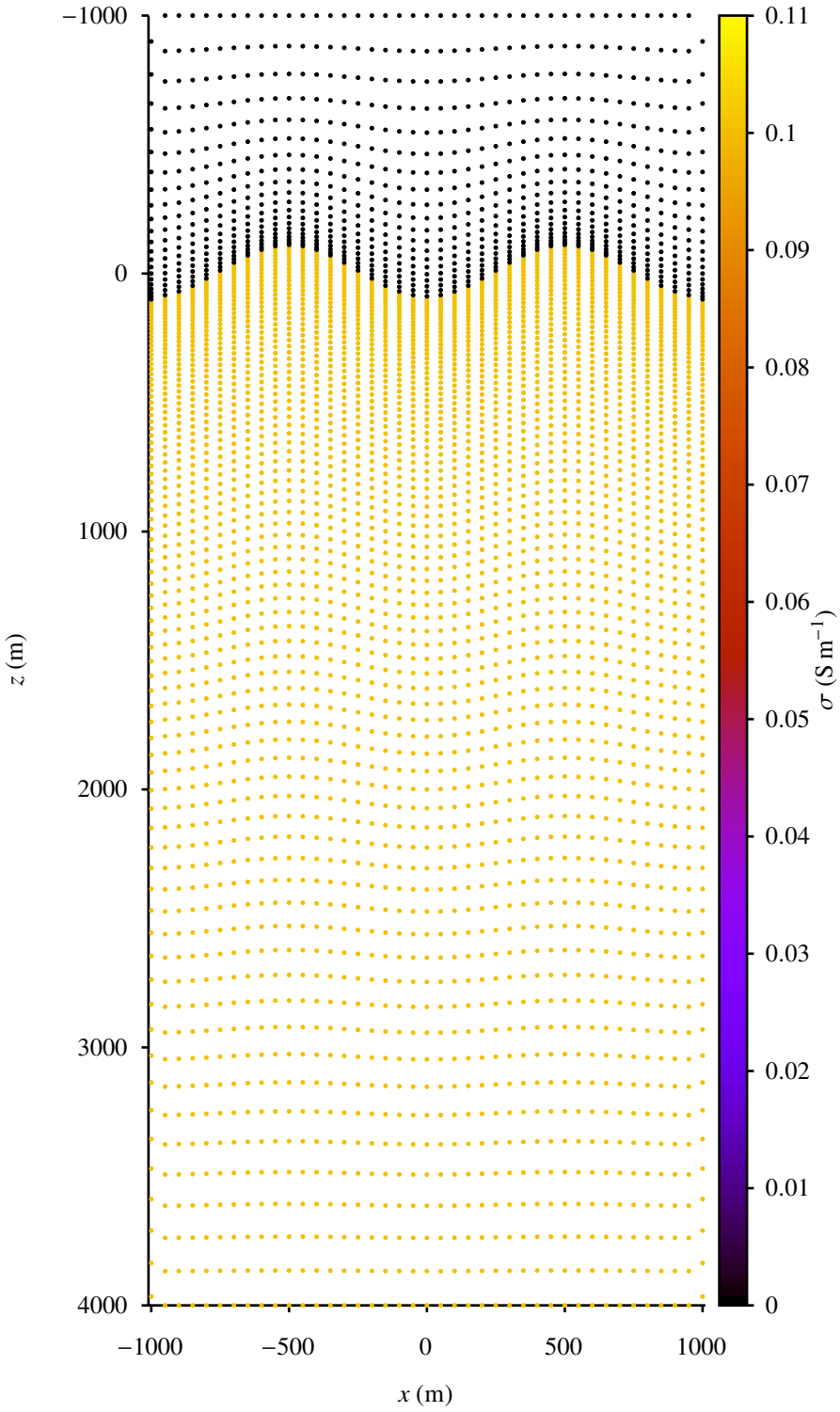

Figure A.54: Spatial adapted regular point sampling for the model of Schwalenberg and Edwards (2004) with an amplitude of $\triangle = 100\text{m}$*, used for the calculations in Chapter 3.8.*

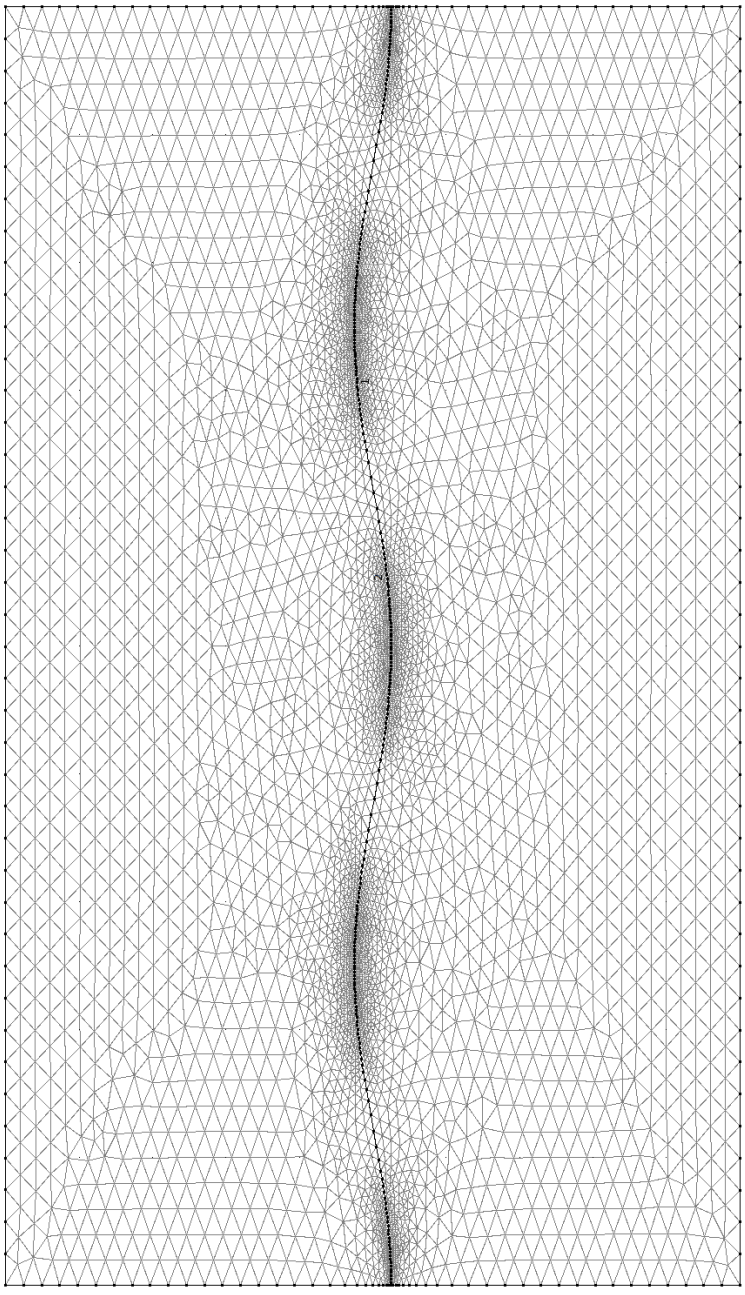

Figure A.55: Finite element mesh for the model of Schwalenberg and Edwards (2004) with an amplitude of $\triangle = 50\text{m}$*, used for comparison in Chapter 3.8.*

Danksagungen

Zuallererst möchte ich mich bei meinem Betreuer Prof. Dr. Bülent Tezkan bedanken. Ohne seine Unterstützung und Vertrauen in meine Arbeit wäre diese Dissertation nicht zustande gekommen. Ich bin sehr dankbar für den wissenschaftlichen Werdegang, den er mir am Institut ermöglicht hat und mir auch in schwierigen Zeiten beistand.

Prof. Dr. Klaus Spitzer möchte ich nicht nur für die Übernahme des Koreferats danken, sondern auch für das Interesse an meiner Arbeit und seine Unterstützung meiner wissenschaftlichen Laufbahn.

Einen sehr großen Dank gebührt meiner Familie die mich immer unterstützt hat und mir in schlechten wie in guten Zeiten beistand.

Ein ebenfalls großer Dank gilt allen meinen Arbeitskollegen am Institut für Geophysik, insbesondere Juliane Adrian, Amir Haroon, Hannah Langenbach, Klaus Lippert, Fabrizio Musacchio, Anne Schreiner, Pritam Yogeshwar, für Zeit die ich mit ihnen am Institut verbringen durfte. Voralleindingen danke ich Juliane, Hannah und Anne für die gemeinsame Zeit auch außerhalb des Institutes.

Weiterhin danke ich auch allen anderen Mitarbeitern und Kollegen am Institut für Geophysik mit denen ich die Jahre über zusammenarbeiten durfte.

Insbesondere danke ich Juliane Adrian, Jennifer Dippe, Amir Haroon, Hannah Langenbach, Anne Schreiner und Pritam Yogeshwar für das Korrekturlesen der Arbeit.

Weiterhin danke ich Amir Haroon für die gemeinsame Zeit im Büro und Sina Hamacher, die mir als meine SHK viel Arbeit abgenommen hat.

Besonderer Dank gebührt Jenny, die mir stets zur Seite stand und immer für mich da war. Sie musste vor allem in der Endphase der Arbeit viel ertragen hat mich aber in der Zeit beispiellos unterstützt. Danke dafür!

Erklärung

Ich versichere, dass ich die von mir vorgelegte Dissertation selbständig angefertigt, die benutzten Quellen und Hilfsmittel vollständig angegeben und die Stellen der Arbeit -einschließlich Tabellen, Karten und Abbildungen-, die anderen Werken im Wortlaut oder dem Sinn nach entnommen sind, in jedem Einzelfall als Entlehnung kenntlich gemacht habe; dass diese Dissertation noch keiner anderen Fakultät oder Universität zur Prüfung vorgelegen hat; dass sie -abgesehen von unten angegebenen Teilpublikationen- noch nicht veröffentlicht worden ist sowie, dass ich eine solche Veröffentlichung vor Abschluss des Promotionsverfahrens nicht vornehmen werde. Die Bestimmungen dieser Promotionsordnung sind mir bekannt. Die von mir vorgelegte Dissertation ist von Prof. Dr. Bülent Tezkan betreut worden.

Köln, 27.11.2017 Jan Wittke

Teilpublikationen

J. Wittke, and B. Tezkan, Meshfree magnetotelluric modelling. *Geophysical Journal International*, 198(2), 1255-1268, 2014.